An Ultra-cold Metastable Helium Beam for Atom Optics and Atom Physics

A thesis submitted for the degree
of Doctor of Philosophy of
the Australian National University

James Anthony Swansson, B.A.(Hons), B.Sc.(Hons), M.Sc.

Atomic & Molecular Physics Laboratories
Research School of Physical Sciences & Engineering Australian
National University
ACT 0200

Australia

December 2006

This thesis contains no material which has been accepted for the award of any other degree or diploma in any university. To the best of the author's knowledge and belief, it contains no material previously published or written by another person, except where due reference is made in the text.

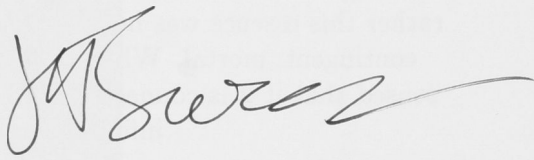

James Anthony Swansson
December 18, 2006

...when one day in winter, on my return home, my mother, seeing that I was cold, offered me some tea, a thing I did not ordinarily take. I declined at first, and then, for no particular reason, changed my mind. She sent for one of those squat, plump little cakes called petites madeleines, which look as though they had been molded in the fluted valve of a scallop shell. And soon, mechanically, dispirited after a dreary day with the prospect of a depressing morrow, I raised to my lips a spoonful of the tea in which I had soaked a morsel of the cake.

No sooner had the warm liquid mixed with the crumbs touched my palate than a shiver ran through me and I stopped, intent upon the extraordinary thing that was happening to me.

An exquisite pleasure had invaded my senses, something isolated, detached, with no suggestion of its origin. And at once the vicissitudes of life had become indifferent to me, its disasters innocuous, its brevity illusory - this new sensation having had the effect, which love has, of filling me with a precious essence; or rather this essence was not in me, it-was-me. I had ceased now to feel mediocre, contingent, mortal. When could it have come to me, this all-powerful joy? I sensed that it was connected with the taste of the tea and the cake, but that it infinitely transcended those savors...

Marcel Proust "In Remembrance of Things Past"

And they,
Because they were not the one dead,
Turned to their affairs.

Robert Frost

Erica Madeleine Schmuck

9/9/75 - 25/8/04

Acknowledgments

This thesis marks the end of a nine year odyssey through graduate studies, including the first two years that culminated in my masters thesis. So it is a small reflection of all that accomplished in that period, though no reflection therefore on their conduct nor value. I could not have gotten even half way here without the effort and support of more people than I could possibly list here. To everyone ... I extend my greatest thanks and appreciation:

Drs Ken Baldwin and Maarten Hoogerland for welcoming a particle theorist into the atom optics group in the Research School at the Australian National University.

For stepping into the breach after Maarten left the ANU, Dr Ken Baldwin.

Dr Andrew Truscott for accepting me into the ACQAO He* BEC project developed from the LHe cooled source, enabling me to continue and finish this thesis.

Drs Andrew Truscott and Ken Baldwin for their comments and guidance in the preparation of this manuscript.

For the collegiality of my fellow lab rats in the dungeon through all those years, Robert and Linda.

For teaching me safe tooling on the lathe and drill press, Steve and Graeme in AMPL workshop.

Dave and his fellows in electronics for helping put the smoke back so many ICs.

James and Julie helped with so many computer questions, simple or not.

Professors David Jameson and Steven Prawer and Dr Bibhu Rout at the University of Melbourne, for their support and collaboration investigating self-assembling monolayers.

Mark, Martin, Doug, John, David, Channa, Jeanette, Tracey and all the other physics dudes as they got on with their lives, for lunch, coffee, or beer whenever I might be in town.

Allan, Amanda, Steve, Jensen, Victoria, Brett, Derryth, Jim, Yongli and so many more colleagues in PARSA, especially Sandra Grey, for the struggles, celebrations, and plain hard work.

Rachel Robbins and Louise O'Rance, my co-Presidents, for their support and advice, in agreement and not, over the years before and since...

Diane Hutchins - just being still in centre of the storm.

Drs Linda Hort and Margot Pearson of CEDAM as partners and advocates for quality assurance in HDRs.

Don Malcolmson, for sage advice in matters personal and business, and Jeffrey Dalton for helping me make a little history.

Dr John Hooper and all the staff of Graduate School, as partners, advocates and opponents.

Professor Ian Chubb, professionally for listening and acting, personally for being there that night.

Anna, Elissa and Marjorie for saying the best at the worst.

Yulia Immajati, Steve Jarvis, Bryony Wakefield, Yasser Abdellatif, Ida Nursoo, Ricky Andraos, Tomoko Tsuru, Charles Tambiah Celia de Winter and the rest of the community at Graduate House, for pulling together.

Tracey for finding the 'odd jobs' that got me through...

For their collegiality during my lectureship in 2003, the Department of Physics at the Australian National University.

Professor Steven Bartos for the faith to hire me and the support to finish.

Finally, to Ellen and Beatrice, for demonstrating that there is life after grad. school.

I wish to acknowledge the financial support of an Australian Postgraduate Award, the Australian National University, and the Australian Research Council for the Centre of Excellence for Quantum-Atom Optics.

Abstract

This thesis is concerned with the achievement and properties of the first metastable helium (He^*) low velocity intense source, or He^* LVIS. The He^* LVIS is the midway point in the Australian National University project to achieve Bose Einstein condensation (BEC) in metastable helium. The He^* BEC apparatus commences with a compact magneto-optical trap (MOT) loading He^* beamline and LVIS in order to load ultra-cold He^* atoms into the MOT/magnetic trap in UHV chamber suitable for evaporative cooling to condensation.

The compact He^* beamline starts with a high flux liquid helium cooled source producing a high flux of atoms, 1.2×10^{14} atoms/sr/s, at a velocity (450 m/s) half of that attainable with liquid nitrogen cooled sources [1]. Matched with an optimally designed Zeeman slower the laser cooling beamline, supplying 1.5×10^{10} atoms/s for trap loading, achieves a large ($\sim 10^9$ atoms) He^* magneto-optical trap over a wide range of detunings, intensities and magnetic field gradients, with a maximum 3×10^9 atoms at -30 MHz [2].

A small modification of the MOT apparatus transforms the atom cloud into a source of atoms for a high quality atomic beam. This atom beam, the first of its type in a rare gas species, produces a maximum flux of 6.0×10^9 atoms/s with an average velocity ~30 m/s and ~25 mrad [3]. The $LVIS^+$ beam brightness[†] $3 - 9 \times 10^{13}$ atoms/sr/s approaches that of the LHe cooled source. This He^* LVIS permits the He^* BEC project to load a large second MOT in a small trapping volume optimal for magnetic trapping and evaporative cooling toward Bose Einstein condensation

[†]This term is defined for the purpose of this thesis in Sec 2.2.2

Contents

Notation

Parameter	Definition
Density operator	$\rho = \|\Psi\rangle\langle\Psi\|$
Detuning	$\delta = \omega_{laser} - \omega_{atom}$
Doppler shift	$\omega_D = -\vec{k} \cdot \vec{v}$
Electric dipole moment	$d_{eg} = e\langle e\|\vec{r}\|g\rangle$
Effective magnetic moment	$\mu' = (g_e M_e - g_g M_g)\mu_{Bohr}$
Excited state density matric element	$\rho_{ij} = \langle\phi_j\|\rho\|\phi_j\rangle$
Lifetime	τ
Spontaneous decay rate	$\Gamma = 1/\tau$
Linewidth	γ
Power broadended linewidth	$\gamma' = \gamma\sqrt{1+s_0}$
Polarisation, circular, linear	$\sigma^{\pm}, \pi$
Rabi frequency	$\Omega = -eE_0\langle e\|\vec{r}\|g\rangle/\hbar$
Saturation parameter, on resonance	$s_0 = 2\|\Omega\|^2/\gamma^2 = I/I_0$
Saturation Intensity	$I_s = \pi hc/3\lambda^3\tau$
Wavenumber	$k = 1/\lambda$
Scattering rate	$\gamma_p = \gamma\rho_{ee}$
Energy	E
Electric field	$\vec{E}$
Magnetic field	$\vec{B}$
Magnetic field gradient	$\partial_z\vec{B}$
Electron emission coefficient	ϵ_e
Emissivity	ϵ
Atomic beam velocity distribution	$P(\vec{v})$
Atomic beam temporal distribution	$I(t)$
Mass	m
Velocity	v
Average, flow or mean velocity	$u = \bar{v}$
Phase space density	$\rho, \rho(\vec{x}, \vec{p}, t)$
Quantum Efficiency	QE
Responsivity	$R_{cal} = E_\gamma \times QE$
Photon energy	E_γ

CHAPTER 1

Introduction

This thesis describes a part of the Australian National University apparatus to achieve Bose Einstein Condensation in metastable helium. Physicists are fascinated with Bose Einstein Condensates as a new phase of matter, one that opens a new view on quantum mechanics. Bose Einstein Condensation in metastable helium (He^*) offers unique access to further insights into these quantum phenomenon via the possibilities of single particle detection (Section 2.5) and ionisation [4, 5]. However He^* BEC is not a straight forward translation of techniques from alkali atoms, as evidenced by the six year delay from the first Bose Einstein condensate until the first He^* BEC was finally achieved [6, 7].

1.1 The ACQAO Objective: He^* BEC

The ultimate aim of the Australian National University He^* BEC group (part of the Australian Research Council Centre of Excellence for Quantum-Atom Optics - ACQAO) is to study the evolution of the relative phase between condensates [8]. It has been hypothesized that the visibility of a relative phase between two condensates should become apparent after just $\sim$ 50 atoms [9]. Alkali BECs are effectively prohibited from studying such evolution by the virtual impossibility of single atom detection. Conversely the near unitary efficiency of single He^* atom detection makes exactly this kind of study possible [4, 5].

The objective of the ACQAO group is the construction of a double well metastable helium BEC in an apparatus containing a micro-channel plate (MCP) for single atom detection. This detector will provide position and time data on single atoms emerging from the coupled BECs from which phase data can be extracted. But to conduct these studies first a simple, reliable machine is required for the production of large condensates. Starting with room temperature helium gas (velocity $v \sim$2 km/s, 20 mtorr source pressure) the full path to BEC includes (with typical parameters

for the ACQAO system):

1. Cryogenic cooling with liquid helium and production of the metastable helium state in an electron discharge source - 10^{14} atoms/s, 450-700 m/s;
2. Laser cooling and slowing of the atomic beam to velocities within the capture velocity of a Magneto-Optical Trap (MOT) - $\sim$ 10^{10} atoms/s, 70 m/s;
3. 'Trapping' and cooling in the first MOT region - $\sim 10^9$ atoms, 2 m/s $\simeq$ 1 mK;
4. Extracting atoms from the first MOT for transfer to an ultra-high vacuum BEC chamber using a high intensity beam of atoms - $\sim$ 10^{10} atoms/s, $\sim$ 25 m/s longitudinal velocity;
5. Trapping atoms in the second MOT - $\sim 10^9$ atoms, 2 m/s $\simeq$ 1 mK;
6. Loading a magnetic trap from the second MOT - $\sim 10^8$ atoms, 300 μK;
7. Evaporative cooling in the magnetic trap;
8. Finally Bose Einstein Condensation of the He* atom cloud - 1 μK, and phase space density $\rho = 2.61$.

This thesis describes my contribution to the development of the first four of these steps: the new liquid helium cooled He* source; the compact MOT loading beamline; the MOT; and finally the production of a new Low Velocity, Intense Source of He* atoms from the MOT, a He* 'LVIS'. The structure of this thesis correspondingly divides into each of these beamline components. The primary experimental results for the source, trap and He* LVIS as reported in Chapter 3, Chapter 5 and Chapter 6, have been published in references [1], [2] and [3] respectively.

1.2 Basic properties and conventions of metastable helium

The electronic spectrum of helium is illustrated in Fig. 1.1. The Russell-Saunders notation $\mathrm{n}^{2S'+1}\mathrm{L}_J$ for angular momentum is used, with n the primary valance quantum number, the total (core plus valence) spin S', core orbital momentum L, and total angular momentum J.

The first excited state is the triplet $2^3\mathrm{S}_1$ state 19.8 eV above the ground state. The lifetime of this state is over 8000 seconds, so it is metastable, and effectively the ground state for the triplet spectrum for the duration of any experiment. The 19.8 eV metastable state de-excites in collisions with surfaces, releasing a charged particle (Sec 2.5). Individual charged particles are easily detected, and hence single particle detection of He* is possible by electronic measurement. However the low 4.8 eV ionisation potential of the metastable state limits the density attainable due to Penning ionisation in He* - He* collisions.

There are three laser transitions accessible in the triplet manifold (Fig 1.1). The 2^3P state is excited by the laser cooling transition at 1083 nm, with a lifetime of 100 ns. Metastable helium has a recoil velocity (9.2 m/s) from this transition substantially larger than typical alkalis. The techniques of atom optics using this transition are discussed in Sections 2.2 to 2.4. In addition the 3^3P state can be excited directly from the metastable state with 389 nm light, and the 3^3D state can be reached indirectly via the 2^3P state with the visible 588 nm transition. This third transition can be very useful as neither the near-infrared 1083 nm transition nor the ultraviolet 389 nm transition can be used to image He* atoms.

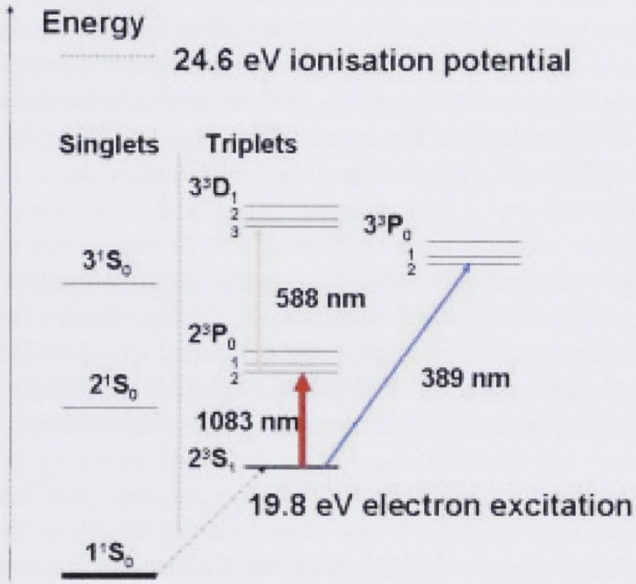

Figure 1.1: State diagram for helium with energy levels and optical transitions.

Another significant state is the metastable 2^1S state with an excitation energy of 20.6 eV. The lifetime $\tau = 19.6$ ms is *relatively* long, meaning that in some cases it is comparable with the duration of experiments. The ionisation potential of this state (4.0 eV) is similar to that of the metastable 2^3S_1 state (4.8 eV) so these two states have similar Penning ionisation rates in gaseous collisions and electron emissivities in surface collisions. Since single particle and electronic detection of helium proceeds through these processes it is possible for the singlet state to 'contaminate' measurements. Beam methods including the removal of contaminants and state preparation are discussed in Sec 2.1.

1.3 The Compact MOT loading He* Beamline

The first part of the path to He* BEC described in this thesis is a compact beamline loading a magneto-optical trap.

The compact MOT loading beamline commences with a high brightness[†], liquid helium (LHe) cooled grounded hollow cathode (GHC) source. This source is designed to produce rare gas metastable atoms at temperatures < 77 K, compared with source temperatures ≥ 77 achieved with liquid nitrogen. For He* generation the liquid helium temperature (4.2 K) is achieved using liquid helium supplied by the Australian National University's recycling helium liquefaction facility. The temperature of the source can be controlled for use as a metastable neon and argon source at their boiling points, 25 and 90 K respectively. This source design generates high brightness beams of these metastable rare gases: $\sim 10^{14}$ atoms/sr/s for helium and neon, and higher than $\sim 10^{11}$ atoms/sr/s for argon. The basis of this design and the properties of the GHC source are discussed in detail in Chapter 3.

Even with improved cryogenic cooling performance a source can never produce a beam of atoms appropriate for loading a MOT. Any trapping potential is still three or four times smaller than the kinetic energy of an ideally effusive source at liquid helium temperature. Hence additional cooling is required of a MOT loading beamline. Consequently the beamline has been implemented with two simple optical stages to collimate and bend the atom beam, followed by a Zeeman slower.

The principal beamline component - a high efficiency Zeeman slower just 3/4 metre long developed by the ACQAO group [10] - is less than half the length of the ANU 'bright beam machine' employed previously [11]. Chapter 4 considers the influences on the final design including the introduction of high power, (relatively) low cost fibre-amplified diode lasers that greatly simplify the production of the required light fields. This compact beamline contains atom optical stages to collimate and slow the atom beam achieving 7.5×10^{10} atoms/s before Zeeman slower, and $1.5 \pm 0.5 \times 10^{10}$ atoms/s after the trapping chamber. Nearly all of these atoms are within the capture velocity of the Zeeman slower and can be slowed to around 70 m/s for trapping.

[†]This term is defined for the purpose of this thesis in Sec 2.2.2

1.4 The He* Magneto-Optical Trap

Large numbers of trapped atoms are a prerequisite for evaporative cooling and Bose Einstein condensation. Progress toward large traps with metastable helium has been slow. This is particularly apparent in the delay from proposal of He* Bose Einstein Condensation (1989 [12]) to its achievement (2001 [6, 7]), particularly in comparison with alkali metals. This is further demonstrated in the history of reported He* magneto-optical traps in Table 1.1 from the first reported traps in 1992 containing just a few tens of thousands of atoms.

The first trend in Table 1.1 is simply the achievement of ever greater efficiency in loading magneto-optical traps. Initially the difficulty lay in simply detecting such small numbers of atoms, in part because of the invisible nature of the major infrared 1083 nm optical transition [13]. More efficient beamlines produced larger and larger traps, e.g. [14, 15]. By this time the limits due to Penning loss rates in the atomic cloud were beginning to be reached [16, 17]. Still experiments progressed toward BEC, e.g. [17, 18, 19], and then achieving condensation, e.g. [6, 7, 20].

A second group of experiments investigated in detail the internal MOT dynamics that potentially limit the size of a cloud of gaseous metastable helium atoms. These included first 'optical collisions' within a trap involving two atoms and a photon [21, 22, 23, 24]. As MOT clouds grew in size it became apparent that the real limiting process was two-body Penning ionization collisions [16, 17]. These limit the gas cloud density to less than 10^{10} cm^{-3}, such that as the total number of trapped atoms can only increase by increasing the trap size.

A third group of helium MOT experiments consider something quite different: boson-fermion mixtures [25, 26]. The availability of the fermionic isotope permits investigations toward the fermionic equivalent of the phase transition to a quantum mechanical BEC: degenerate Fermi gases (DFG) [26]. The similarities between the two isotopes means that ^{3}He* experiments don't start over from the beginning.

In the ACQAO experiment the first magneto-optical trap is loaded directly from the Zeeman slower, the distance to the trapping region minimised with a specially designed MOT configuration. The efficacy of the compact beamline design is proven, loading up to 3×10^9 atoms in a cloud about 4-5 mm in diameter [2], equivalent to the ANU MOT loaded with the 'bright beam line' [27]. The characteristics of the trapped atom cloud itself are discussed in Chapter 5.

Year	Laboratory		Atom Number	T mK	B Field G/cm	δ_{MOT} MHz	I/beam mW/cm2
1992	IMS	[13]	1×10^4	-	-	-10	9.6
2000	IMS	[25]	1×10^5	0.5	9-16	-5	20
1992	LCFIO	[28]	1×10^4	~ 1	20	-5	4
2000	LCFIO	[19]	1×10^8	0.6	5	-	-
2000	LCFIO	[16]	3.0×10^7	1.5	10-6-4	-20	4
2001	LCFIO	[18]	3.0×10^8	~ 1	[19]	-	-
1997	Vrije	[14]	3.0×10^7	~ 2	19	-40	5.5
1999	Vrije	[15]	1.5×10^9	~ 1.1	20	-35	24
2003	Vrije	[29]	2.0×10^9	1.2	-	-	
2004	Vrije	[30]	1.2×10^9	0.4	12	-35	-
2004	Vrije	[26]	3×10^8	~ 2	-	-40	-9.1
2001	ENS	[6, 31]	1.0×10^9	~ 1	-	-	500
2001	ENS	[17]	1.0×10^9	~ 1	20	-45	8
2002	ENS	[32]	-	~ 1	27	-45	8
1997	Utrecht	[33]	-	-	-	-	-
1998	Utrecht	[22, 23, 24]	5.0×10^5	~ 1.1	15	24	8.3
2001	Utrecht	[34]	1.0×10^6	1		-25	10
2003	TUB	[35]	5.0×10^5	2	23-30	-20	P=30
2005	ANU	[27]	$\sim 2\times10^9$	-	-	-	-
2006	ACQAO	[2]	$\sim 3\times10^9$	-	~ 10	-30	14

Table 1.1: Summary of reported He* magneto-optical traps at seven He* atom trapping laboratories worldwide, LCFIO, Vrije and ENS have created a He* BEC, as well as the ANU. The ACQAO trap discussed in this thesis is part of the ACQAO He* BEC.

IMS	Institute for Molecular Science, Okazaki
LCFIO	Laboratoire Charles Fabry de l'Institut d'Optique, Orsay
Vrije	Vrije Universieit, Amsterdam
ENS	Ecole Normale Superieure, Paris
Utrecht	Utrecht University, Utrecht
TUB	Technische Universität Berlin, Berlin
ANU	Australian National University, Canberra
ACQAO	Australian Centre of Excellence for Quantum-Atom Optics at ANU.

1.5 He* from MOT to BEC

Although the compact beamline loaded MOT reported in Chapter 5 is one of the largest reported in Table 1.1 it is unsuitable for conversion into a magneto-static trap and cooling toward condensation.

Pereira Dos Santos *et al.* provide a detailed description of the effort to condense metastable helium [32]. This experiment commences with a similarly large ($\sim 10^9$ atoms) MOT [31]. However the $\sim 5 \times 10^6$ atom BEC has a lifetime of only 2 seconds, at a partial pressure of helium of 5×10^{-11} torr [32]. Even the lifetime of the magneto-static trap is considerably prolonged ($\sim 4\times$) by the reduction in pressure to 10^{-11} torr.

In the compact beamline the He* beam is deflected before the Zeeman slower, producing differential pumping achieving a partial pressure of helium of order of 10^{-9} torr. This pressure is too high to achieve condensation, so the atoms must be transfered to a second ultra-high vacuum chamber.

Since the final photon emission by an atom heats the atom, by 4.1 μK for He* compared with the 1 μK condensation temperature, magnetic trapping and evaporative cooling has become the standard route to condensation. However even with metastable helium's relatively large effective magnetic moment the trapping potential of large magnetic traps (20-100 G/cm) is still very small. In Reference [32] the magneto-static trap has a maximum magnetic field gradient 256 G/cm corresponding to a trap depth of 16 mK. The three 2 cm diameter magnetic coils of this Ioffe-Pritchard trap contain an average 6000 ampere turns at a distance 26 mm from the trap centre [32]. To obtain optical access for the 2 cm diameter MOT beams and the two absorption imaging beams the MOT is trapped in a $4 \times 4 \times 5$ cm quartz cell.

The 10^9 atom MOT loaded from the compact beamline in Chapter 5 captures He* atoms from the Zeeman slower at 70 m/s. This requires large MOT beams (38 mm in diameter) to adequately slow atoms in the trapping region. The quadrupole coils, located 50 mm from the trap centre, produce a maximum magnetic field gradient of a few tens of gauss per centimetre. Closely placed magneto-static trap coils would obstruct the laser beams, drastically reducing the MOT trapping efficiency, as well as obscuring optical access for imaging.

So to obtain a large He* BEC it would be better to design a BEC chamber optimised for the goals of the ACQAO project, with closely spaced coils permitting fewer ampere turns, and the best optical access, and transferring the large number of trapped atoms from the first trap to a second ultra-high vacuum chamber for optical and magnetic trapping. This means converting the MOT into a source of a further beam of He* atoms.

1.6 Low velocity, high density atom beams

Since 1996 there has been an intense activity on the part of several groups to investigate magnetic-optical traps as sources for high density, low velocity beams of atoms for study. All operate on the same principle: the basic MOT traps atoms and condenses them into a region where some additional effect induces a linear motion producing an atomic beam. This general description can be subdivided into three categories:

- $3D^-$-MOTs, where one or more elements of a three dimensional MOT is removed (Sec 1.6.2);
- pyramid MOTs, based on a single laser (Sec 1.6.3); and
- push-beam MOTs, that use an additional laser beam to push atoms from the trap (Sec 1.6.4).

The key characteristics of these beams are their very low velocities (a few tens of metres per second) and their high densities, derived from the properties of the trapping regions.

The He* 'Low-Velocity Intense Source' (He* LVIS) is the ultimate objective and product of this thesis, considered in Chapter 6. A simple modification of the trapping apparatus converts the MOT into a source and creates a beam orthogonal to the Zeeman slower He* beam - thus there is no line-of-sight path from the source to the BEC chamber. The He* LVIS is improved with an additional laser beam, making the '$LVIS^+$'. The He* $LVIS^+$ brightness is nearly equivalent of the GHC source ($3 - 9 \times 10^{13}$ atoms/st/s) delivering 6×10^9 atoms/s at a low $\vec{v} \sim 30$ m/s velocity, suitable for loading a small magneto-optical trap. This He* LVIS compares favourably with other low velocity atom sources and achieves a very high rate of atom transfer to the UHV trap chamber for Bose Einstein condensation of metastable helium.

1.6.1 The Low-Velocity Intense Source

In the first report of such a beam in 1996, Lu *et al.* coined the term 'Low-Velocity Intense Source', or LVIS for short, as the name for their design [36]. The LVIS, whose design is the basis for the work in this thesis, is of the first category of devices, a $3D^-$-MOT. The only difference between the LVIS and the standard MOT is a narrow dark center introduced to one of the six MOT laser beams. Atoms at the centre of the MOT experience an asymmetrical radiation pressure and are accelerated out along the dark 'extraction column'. The extracted beam is continuously collimated

by the dark column, since divergent atoms which exit the extraction column are exposed to the restorative forces of the standard MOT beams and recycled into the centre of the MOT. In 1996 the brightest beam of slow atoms was produced using magneto-optical focusing in two dimensions (Sec. 1.6.2) with sodium in 1989 [37]. With 5×10^9 atoms/s at 5×10^{12} atoms/sr/s the Rb LVIS exemplified an order of magnitude brighter beam of atoms than in Ref [37].

The velocity profile achieved by Lu *et al.* with ^{87}Rb is a 2.7 m/s FWHM around a 14 m/s mean velocity. This width is significantly larger than the Doppler cooling limit of 0.12 m/s, a fact the authors attribute to the variation of entry points to the extraction column, and hence the different periods of acceleration.

Several laboratories have used the rubidium LVIS to load a second MOT [38, 39] or optical molasses [40], load a magnetic and optical guides [41, 42, 43]. In turn these have been steps toward improved atomic fountains [40], optical dipole traps [39] and beamsplitters [42, 43] and precision spectroscopy [38].

1.6.2 3D$^-$-MOT

The major tradition of '3D$^-$-MOT' experiments, which includes the LVIS, relates back to earlier work, e.g. Riis *et al.* in Ref [37] and includes devices like the ANU beam compressor described at length in Section 2.4 and reported in Ref [11].

In 1990 the authors of Ref. [37] described an atomic 'funnel' using a 2-D optical molasses and a radial magnetic field produced by a quadrupole of 'hairpin' wires illustrated in Fig. 1.2. Inside the parallel wires the magnetic field is predominantly a transverse 2-D quadrupole field constant along the length of the wires. Ordinarily, in conjunction with the optical molasses, this would focus the atomic beam. Instead the light fields are located at the ends of the wires. Here the quadrupole field decreases axially from 80% of maximum field gradient at the hairpin ends to 10% at 2.0 cm beyond. Hence the decrease in magneto-optical focusing is balanced by an increase in molasses cooling. This is enhanced by changing the polarization from circular for trapping to linear for cooling. The result, while still somewhat axially velocity selective, is a transverse bunching and cooling like a funnel. The authors report that while the thermal beam intensity is reduced from 10^{12} to 10^9 atoms/s, the improvement in divergence means the beam brightness is increased by three orders of magnitude [37].

In the past ten years many versions of a 2-dimensional MOT plus some additional optical or magnetic force or guide have been reported for rubidium [44, 45, 46, 47, 48], cesium [49, 50] and most recently potassium [51].

In 1998 Dieckmann *et al.* reported on 2D$^+$-MOT which was directly comparable

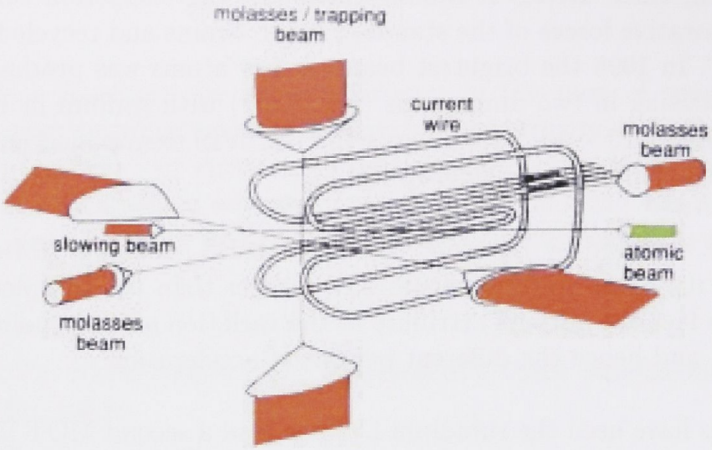

Figure 1.2: Sodium beam focusing using a hairpin wire 'funnel'. The constant 2-D quadrupole field within the parallel wires would ordinarily focus the atomic beam in a magneto-optical lens, but the axially weakening quadrupole field at the hairpin end permits transverse cooling concomitant with focusing. Illustration modified from [37].

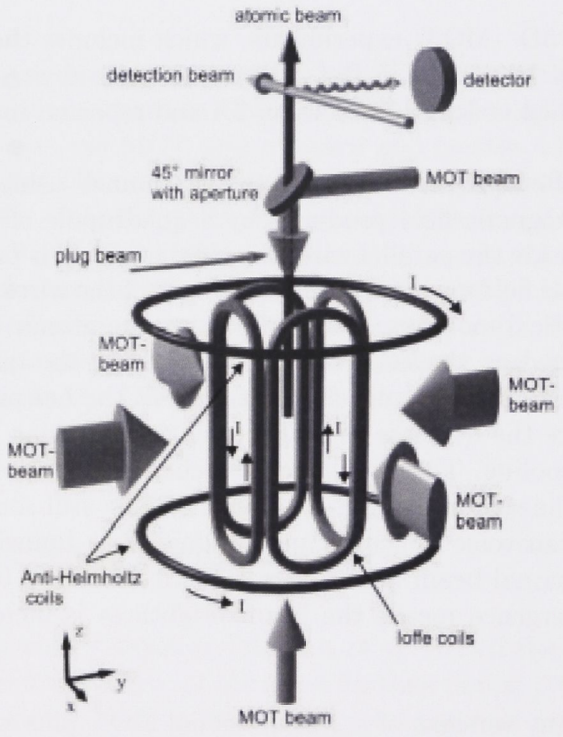

Figure 1.3: Apparatus for 2D-MOT, $2D^{+}$-MOT and LVIS. Illustration from Ref. [45].

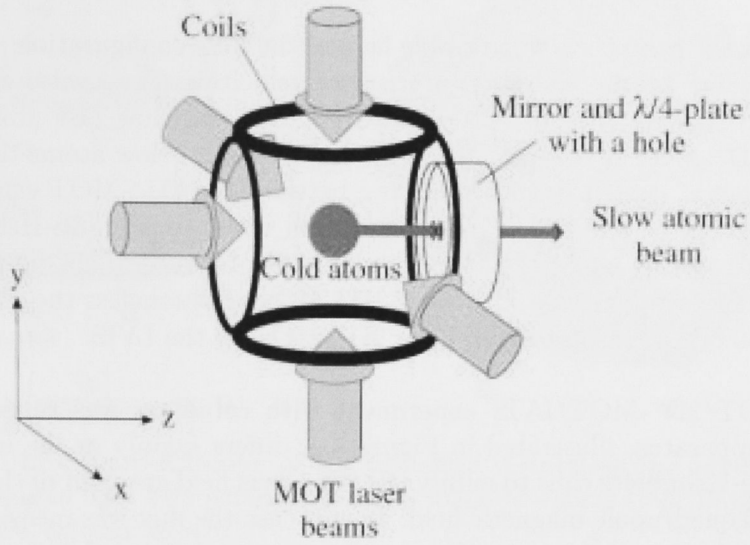

Figure 1.4: Apparatus for 2D-MOT, $2D^+$-MOT and LVIS. Illustration from Ref. [46].

with the LVIS by the construction of an easily adaptable apparatus [45]. In their apparatus, illustrated in Fig. 1.3, it can be seen that the rig is essentially the same geometry as an LVIS, but in addition to the normal anti-Helmholtz MOT coils the authors have Ioffe 'racetrack' coils. Similarly to [37] these coils produce a cylindrical quadrupole field, which is used in the '2D-MOT' or '$2D^+$-MOT' experiments.

In any configuration the trapping region captures rubidium atoms from the vapour produced from an oven reservoir. Then a rising atomic beam is produced that passes through a 0.8 mm collimation aperture into an ultra high vacuum chamber where the beam is analysed. The 2D-MOT cools atoms in the radial ($x-y$, see Fig 1.3) plane. The atoms then escape in the vertical (z) direction with the preserved component of thermal energy, making two vertical beams (one up, one down.) However those atoms with a high velocity in this direction are rarely within the trapping region long enough to be significantly transversely cooled, and hence are mechanically filtered from the beam by the narrow collimation aperture.

The $2D^+$-MOT is an extension of the 2D-MOT, where an additional pair of laser beams are applied in the z-direction. By unbalancing the intensity of these molasses in favour of the upward beam a greater flux of atoms can be generated through the aperture. Since the downward beam contains a central shadow due to the aperture in the 45° mirror (see Fig 1.3), those atoms exactly on axis are strongly accelerated

in the same way as in an LVIS.

It is apparent that the cylindrical quadrupole field of the Ioffe configuration extends the region along which atoms with large transverse velocities are recycled through cooling, further enhancing the trap's ability to capture and slow fast atoms. It follows that the $2D^+$-MOT is likely to produce a higher flux of slow atoms than the LVIS. Dieckmann *et al.* tested this by switching between the $2D^+$-MOT configuration with the Ioffe coils on and the LVIS configuration with just the anti-Helmholtz coils. In both cases the 3D molasses have an equal power balance. This means that this case is not exactly comparable with their $2D^+$-MOT. Nonetheless the potential improvement of $30\times$ is a reason to prefer the $2D^+$-MOT to the LVIS.

A similar 2D-MOT/$2D^+$-MOT/LVIS experiment with rubidium was reported in 2005 [46]. This apparatus, illustrated in Figure 1.4, differs mainly in the use of a second pair of anti-Helmholtz coils to nullify the the z-axis field gradient of the main three-dimensional quadrupole magnetic field. In this case the flux was measured by loading of a second trap, but no significant difference was recorded between the 2D-MOT and LVIS configurations.

The principle of the 2D-MOT has been proved in application with light metastable atoms in the production of a scanning focused spot with helium [52] and of a slowed beam of neon mode matched for a surface magnetic guide [53].

1.6.3 Single beam pyramid MOT and beam techniques

One drawback of the LVIS is the complexity of a six-beam magneto-optical trap for what is, after all, merely a source of atoms in a beam. For this reason much interest has focused around a simpler device: the pyramid MOT.

In the same year that the LVIS was reported, Lee *et al.* examined a simple MOT apparatus constructed from a single laser beam and either a pyramidal or hollow conical mirror [54]. The principle of these designs is illustrated in Fig 1.5. With each reflection the polarization is reversed, with the net result that in each dimension we have an opposed pair of $\sigma^+ - \sigma^-$ beams. Moreover these are in a configuration for a MOT when used in conjunction with a magnetic coil pair aligned with the z-axis (Fig 1.5-a.) Hence in the hollow of the pyramid there are always three pairs of oppositely polarized beams in a MOT configuration, while for the conical hollow, or axicon mirror, there are innumerable concentric pairs of transverse counter-propagating beams. In both cases all of the beams required for a MOT are produced by a single laser beam.

Such MOTs are limited by the precision of construction of the pyramid or axicon mirror. The pyramid configuration is bound to suffer defects at the corners of the

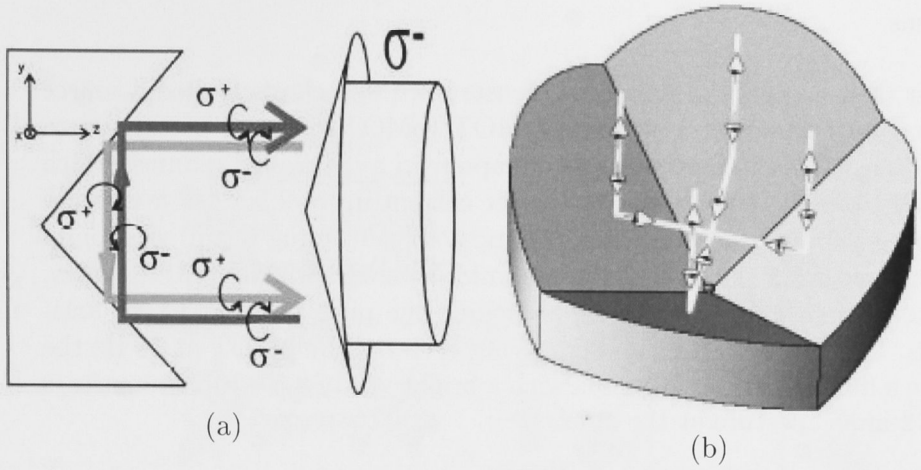

(a) (b)

Figure 1.5: Retro-reflection of the light field illustrating the formation of the required light field polarizations for a magneto-optical trap. Illustrations from [54] (a) and [57] (b).

mirrors due to imperfections in the cut edges. In both cases the apex cannot be manufactured to exacting perfection because of the surface and fitting imperfections at the acute corners of the cut mirrors for a pyramid, or the finite size of the cutting edge of the tool used to manufacture the axicon cone.

In practice, the MOT is difficult to form and image in the centre or near the edges of the pyramid mirrors due to light scattering. In the axicon mirror system a MOT is possible near the symmetric mirror axis. In this case the authors were not able to measure its size due to the distortions resulting from the roughness of the mirror surface. Otherwise the authors of Ref [54] measured $\sim 1.2 \times 10^7$ ^{85}Rb atoms in the pyramidal MOT, which they compare with the $3 - 4 \times 10^7$ atoms trapped in their MOT using similar light fields.

In both configurations the manufacturing limits imply that exactly along the axis there is no retro-reflected light at the apex, and hence an imbalance in the the radiation pressure on the atoms. For this reason the authors suggested the use of this apparatus as a 'pre-cooled funneled atom source'.

In a later study these same authors improved on the construction of the axicon mirror used for the conical MOT [55]. Here the mirror is made from an aluminium coated machined glass substrate with its surface polished to an optical flat within a wavelength. In this instance the axicon mirror has a 2 mm hole at the apex which they note is an almost inevitable by-product of machining a sharp point. However this can be used to extract a slow atom beam, or can be blocked with a retro-reflecting mirror and 1/4 wave plate so that the MOT can be formed on axis. Under similar circumstances to their earlier experiment [54] they measure a similar

number of atoms.

Two years after their suggestion, Arlt *et al.* constructed and characterized a source of slow cesium atoms based on a pyramidal MOT (pMOT) [56]. A getter source placed close to the pMOT liberates a cesium vapour in a controlled manner which is captured by the pMOT. By varying the getter current up to 2.5×10^8 atoms are captured by using a 'plug beam' on axis. The most efficient 'plug beam' was found to be one introduced from the rear of the pyramid, coaxial with the pMOT beam. The pMOT atom beam was produced by switching the plug beam and trap anti-Helmholtz coils. By cycling loading and emptying cycles of the pMOT at 10 Hz the authors achieve a flux of 1.1×10^9 atoms/s with a brightness of 8.5×10^{11} atoms/sr/s through a 1×2 mm^2 aperture at the apex.

At the same time, Williamson *et al.* [57] demonstrated the loading of a second MOT, located 35 cm away from a 'magneto-optical funnel' with a 2 mm hole at the apex. This pMOT captures ^{39}K and ^{40}K produced with a tandem accelerator. The low conductance through this aperture aids in the maintenance of differential vacuum between the accelerator source and the ultra-high vacuum trapping chamber. A UHV pressure of 10^{-11} torr can be maintained with the pMOT pressure approaching 10^{-6} torr with minimal effect on the loading rate of the UHV-MOT.

The authors measure the efficiency of the funnel by comparing the loading rates of the UHV-MOT with the pMOT formed off-axis. These measurements reveal only 6% efficiency in MOT loading. This cannot be directly compared with the LVIS described in Section 1.6.1, which is yet to be reported loading a second magneto-optical trap. But the LVIS did transfer 70% of atoms into the atomic beam. The success of this source has prompted improvements in performance, particularly in beam brightness, by other investigators [58, 59].

1.6.4 Push-beam MOT

The final class of MOT based beam sources is a trap augmented with an extra laser beam which pushes the cooled atoms from the trap. A typical experiment from Ref [60] is illustrated in Figure 1.6. In this experiment potassium atoms are pushed with an additional laser beam from the first trapping chamber on the left through an intermediate focusing 2D-MOT to the second trapping chamber. At a 48 cm trap centre separation the authors achieve up to 78±14% transfer efficiency with the focusing atom funnel, improved from 55±9% with just the push-beam.

Two rubidium experiments were simultaneously reported in 2001 by Cacciapuoti *et al.* [61] and Wohlleben *et al.* [62]. Each experiment is similar in that once atoms are trapped in a standard vapour-cell magneto-optical trap they are pushed by the unbalanced radiation pressure of an additional focused beam. The dipole force

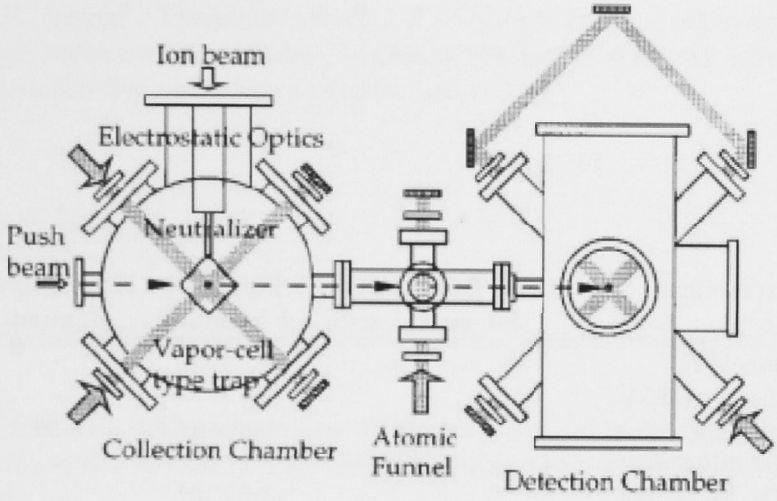

Figure 1.6: Apparatus for push-beam transfer of ^{41}K atoms between magneto-optical traps. Illustration from Ref. [60].

within this beam guides the atoms during transfer over long distances (35 cm) to load a second MOT at ultra-high vacuum. It is noteworthy that while these experiments achieve results within a factor of two of one another, they are both orders of magnitude below the LVIS and 2D$^+$-MOT experiments which also use rubidium.

1.6.5 Comparison of low velocity, high intensity beams

The key beam properties of brightness[†] and velocity of these experiments and the He* LVIS are summarized in Table 1.2. These show the progress of these designs since 1990 and the variety of success in terms of intensity and/or velocity. The best slow beams (velocity order of 10 m/s) have a flux order of $\sim 10^{10}$ atoms/s and brightness order of $\sim 10^{13}$ atoms/sr/s. These all employ some configuration of '3D$^-$-MOT', including pyramid MOTs without an apex. The three metastable rare gas experiments stand out especially for their higher velocities and higher brightness, and are a particular benchmark for He* LVIS.

The He* Low Velocity Intense Source (LVIS) represents the second novel and significant result to be studied in this thesis in Chapter 6. The He* LVIS is the first of its type to be produced with a metastable rare gas. The maximum He* flux was achieved with a hybrid 'LVIS$^+$' design, a '3D$^-$-MOT' apparatus like the original LVIS with an additional push-beam. This achieves a flux and brightness on

[†]This term is defined for the purpose of this thesis in Sec 2.2.2

Year	Atom	Experiment	Brightness [atoms s^{-1} sr^{-1}]	Flux (cw) Φ [atoms/s]	Divergence Θ [mrad]	Velocity $\langle v_z \rangle$ [m/s]
1990	Na	funnel [37]	-	1.0×10^{9}	-	270
1996	Rb	axicon trap[54]	-	-	-	-
1996	Rb	LVIS [36]	5.0×10^{12}	5.00×10^{9}	5-36	14
1996	Rb	$2D^{+}$ MOT [48]	-	1.0×10^{10}		3-10
1997	Cs	$2D^{+}$ MOT [50]	-	1.0×10^{6}	-	1.5-5
1997	Rb	axicon trap[55]	-	-	-	-
1998	Cs	$2D^{+}$MOT [49]	7.6×10^{9}	1.3×10^{8}	-	0.7-3
1998	Cs	pyramid [56]	8.5×10^{11}	1.10×10^{9}	40	8-12
1998	K	pyramid [57]	-	-	-	-
1998	K	push-beam [60]	-	-	-	40
1998	Rb	$2D^{+}$-MOT [45]	6.2×10^{12}	9.00×10^{9}	43	8
1998	Rb	$2D^{+}$MOT [47]	7.5×10^{13}	6.0×10^{10}	32	50
1999	Rb	LVIS [38]	-	4×10^{9}	-	11
1999	He*	2D-MOT [11]	1.0×10^{14}	$\sim3\times10^{10}$	10	70-100
1999	He*	funnel [52]	-	$\sim10^{10}$	-	600
2001	Rb	push beam [61]	-	7.0×10^{7}	-	14-18
2001	Rb	push beam [62]	1.3×10^{12}	1.3×10^{8}	10	14
2001	Cs	pyramid [58]	7.5×10^{12}	4.00×10^{9}	25-27	8-12
2002	Ne*	2D-MOT [63]	1.5×10^{14}	6.00×10^{8}	-	26
2003	Cs	pyramid [59]	1.2×10^{13}	2.20×10^{9}	11-16	7-16
2003	Rb	$2D^{+}$MOT [44]	5.12×10^{13}	8.0×10^{9}	12.5	2-15
2005	Rb	LVIS/$2D^{+}$ MOT [46]	-	8.0×10^{9}	-	8.5-11
2006	K	2D-MOT [51]	-	1.0×10^{11}	-	33
2006	He*	$LVIS^{+}$ [3]	$3-9\times10^{13}$	6×10^{9}	18-26	20-35

Table 1.2: Summary from selected slow ($\langle v_z \rangle \leq 30$ m/s) atomic beam sources since 1990, with brightness, flux, divergence and velocity where reported.

par or exceeding equivalent MOT-based experiments, and nearly that of the LHe cooled GHC source[†]. The beam velocity, $\vec{v} \sim 30$ m/s velocity, while high compared to the much more massive alkalies, is clearly the lowest achieved with helium and equivalent to the five times more massive neon.

1.7 Conclusion

This chapter outlines the direction of this thesis and the chapters that follow:

- The following Chapter reviews the theory and practice appropriate to atom beams, atom optics and metastable helium that underpin the work of this thesis.
- Chapter 3 describes the principles and performance of the first significant result of this thesis, the liquid-helium cooled, grounded hollow cathode He* source.
- The performance of the compact beamline, matching this source with an efficient Zeeman slower, is reported in Chapter 4.
- The characteristics of the He* trap loaded by the compact beamline are reported in Chapter 5, compared to other He* MOTs, and considered for use as a source for a slow He* beam.
- Finally the realisation of that beam, the He* LVIS and LVIS$^+$, the second significant result of this thesis, is studied in Chapter 6.

The performance of this compact beamline He* LVIS, summarised above, met the expectations of the ACQAO He* BEC group, which has subsequently achieved the world's fourth metastable helium Bose Einstein condensate with over one million atoms.

[†]This performance has been improved since the experiments reported in this thesis and the brightness of the LVIS beam is now approximately the same as that of the GHC source.

CHAPTER 2

Basic principles toward achieving low velocity, high density atom beams

The physics of atoms in a beam is a central and recurring theme of this thesis. An experiment with a beam of atoms has three basic sections:

- a source, whence emerge atoms in a beam;
- a beamline, where interactions of some kind modify the beam; and
- a detector that measures changes of the beam.

In metastable helium experiments atoms trapped in a MOT must be derived from a beamline rather than captured from the background gas due to the high source velocities and non-metastable source gas load. Metastable helium sources and the detailed properties of the new GHC source are studied in detail in Chapter 3. This chapter outlines the generalised properties of beamline interactions and detection that are applied to the experiments in this thesis.

An important optics concept central to the consideration of atom beams in this thesis is beam brightness. Applicable to both light and atom beams, brightness, the number of particles per steradian per second, is an important concept in geometric optics of light because the 'brightness theorem', or Liouville's theorem, requires that the brightness (or phase space density) cannot change. The most distinctive difference between light optics and atom optics is that the phase space or beam brightness of an atom beam can be changed, underpinning the field of atom optics.

The first section in this chapter considers the range of general elements that can be employed in metastable beamlines to modify the beam. The major part of this chapter considers the interaction of light with atoms (Sec 2.2.2) and its application in atom optics (Sec 2.3) using the existing ANU bright beam machine as an example (Sec 2.4). The last section of this chapter reviews the optical and electronic methods for detection of He^* atoms.

2.1 Modification and analysis of metastable atom beams

There are five general types of metastable atom source, discussed at greater length in Chapter 3. All types produce a variety of products in addition to the particular metastable state M^* of the molecule M of interest for study. A background beam of ground state atoms is always present since the efficiency of excitation varies from $\sim$50% for some thermal sources to $10^{-4} - 10^{-5}$ for electron discharge sources [64]. In addition a considerable proportion of electrons, ions, high energy photons and alternative metastable neutral states are produced in these sources. The new grounded hollow cathode source studied in Chapter 3 typically produces 50% ions, with the remainder being composed of metastable states and photons in the ratio $2^1S:2^3S:\gamma$ = 1:7:2.

The variety of methods for modification of a metastable beam in order to condition the beam to the species and state desired for experimental detection are illustrated in Figure 2.1. Commencing from the metastable M^* source (stage 1) a beam can be

- mechanically collimated (stage 2);
- rid of charged (M^+, e^-) states (stage 3);
- rid of metastable (typically doubly excited) states that are 'short-lived' relative to the duration of the experiment (stage 4);
- rid of metastable states that are 'long-lived' relative to the duration of the experiment (stage 5);
- prepared in a specific magnetic (stage 6) and velocity (stage 7) states; and
- deflected or otherwise optically manipulated (stage 8) before
- detection (stage 9).

Optical manipulation and atom detection are discussed in greater detail in the following Sections 2.2, 2.3 and 2.5 respectively. Chapter 3 is devoted to the apparatus and properties of the GHC metastable atom source. Attention in this section is paid to those other elements of beam preparation following the source in this metastable beamline.

2.1.1 Mechanical collimation

Section 3.1 describes later how the divergence of the emitted beam depends on the source geometry. This is principally manifest in the effusion of atoms in a cosine

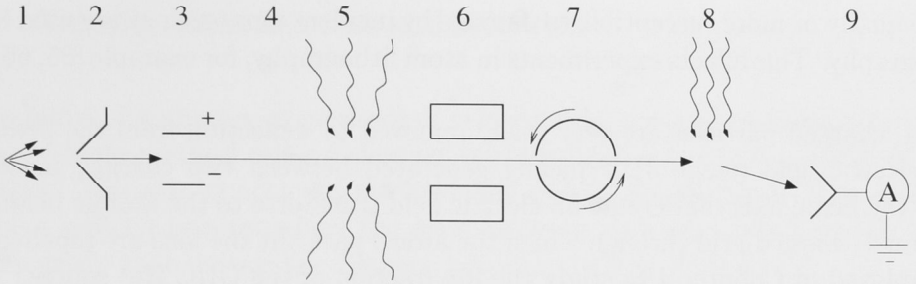

Figure 2.1: Schematic components to modify and analyze metastable beams: (1) divergent beam from source; (2) mechanical collimation by a skimmer; (3) charged plates; (4) drift region; (5) optical saturation; (6) inhomogeneous magnetic field; (7) velocity selector; (8) laser deflection; (9) metastable detection.

spatial distribution from the beam axis (see Eq 3.1), so mechanical collimation of this beam is usually required. In the case of low efficiency sources collimation is required immediately after the source so that a significant fraction of the ground-state gas load can be removed from the beam.

This is achieved with a skimmer (stage 2), a cone with a sharp aperture typically about the same diameter as the source nozzle. The sharp edge of the cone effectively deflects gas particles that collide with it away from the region of high density back into the source chamber where they are pumped away. Together with a high through-put vacuum pump this technique enables the maintenance of a typical pressure differential of 10^3 between the source chamber and the following beam chamber.

2.1.2 Charged particle removal

The flux of charged particles in the beam can be very significant, especially in sources based on electronic collisions. Electrons can form a fraction of the flux from the discharge source, since the electrons in the source flow in parallel with the atoms through the nozzle aperture (Sec 3.3). This is the case with the GHC source even when the source anode is 'internal' to the nozzle (Sec 3.3.3). Ions are also significant, up to ~50% of the excited state flux, since the ionization and excitation energies differ by a few eV (4-5 eV for He) and both are an order of magnitude less than the typical electron energies of a few hundred electron-volts [64].

Ions are of greater concern in beamline experiments than electrons. The measurement of flux by current detection cannot distinguish between ions and metastable atoms, since the latter proceeds largely through ionization processes (Sec 2.5.2). Similarly surfaces susceptible to modification by the surface interactions of metastable

atoms are equally or more susceptible to damage by incident ions, such as are used in atom lithography. This affects experiments in atom lithography, for example [65, 66].

For all this, charged particles are very easily removed by deflection from the beam using an electric field (stage 3), typically generated between two charged plates parallel to the beam axis that create an electric field transverse to the atomic beam, or a transverse charged grid through which the atoms pass but the ions are repelled. This is employed in Chapter 4 to study the ion fraction of the GHC He* source.

2.1.3 Optical pumping/quenching

Usually more than one metastable or Rydberg state is produced by the source. If these states are not ionized in the electric field (stage 3), or as short-lived states de-excite in a drift region (stage 4), it is usually desirable to quench all but the state of experimental interest. Although the lifetime of the 2^1S state in helium is quite short, $\tau = 19.6\ ms$, this is still sufficiently long at He* beam velocities to travel the length (2-20 m) typical of He* beamlines.

Photon excitation (stage 5) of the metastable state into an excited state usually results in eventual decay to the ground state. Coherent light is not necessarily required. The 2^1S state in helium can be pumped with 2.06μm light produced in a He discharge tube, which can be wrapped in a spiral around the atomic beam. This excited state decays to the ground state. The low energy photon-excited states of 2^3S state merely decay back into the long-lived ($\tau = 8000\ s$) triplet state [67]. This is employed in Chapter 4 to study the singlet fraction of the GHC He* source.

2.1.4 State selection and beam compression

The next beamline component is based on the metastable state's interaction with an inhomogeneous magnetic field. The 2^3S state is highly spin polarisible, particularly in comparison to the singlet ground and 2^1S states, both of which, with $m_J = 0$ sub-states, are undeflected by the magnetic field. A six-pole magnetic lens is more efficient than a simple Stern-Gerlach magnet in selection/analysis of a spin-polarized beam. Particularly with the undeflected ground and singlet atoms blocked by a central plug, Baum *et al* reported polarizations as high as 90% and ground-state:metastable ratios as low as 10^2 [68]. This efficiency has seen the six-pole magnetic lens utilized for beam compression in a simple LHe cooled beamline [34], and UV photon free lithography [69].

2.1.5 Velocity measurement and selection

The simplest of a number of methods of velocity selection and analysis is by means of time-of-flight method using a chopper that blocks the atomic beam for all but a brief time. This can be achieved mechanically or with a laser beam. Two choppers become a velocity selector where the delay between their open windows selects the velocity group that crosses the distance between them in that period.

This window, typically a few tens to hundreds of microseconds, allows a small packet of the total atomic beam to pass. In our experiments the chopper is usually a spinning disk 10 cm in diameter with a 1 mm radial slot at one point on its diameter. Rotation speeds ~30-60 Hz correspond to window periods of 100-50 μs respectively. The velocity characteristics of this packet can be measured by an atom detector at some distance L_{TOF} downstream. In a metastable rare gas beam with line of sight to the atomic source the UV photon flux conveniently provides a measurement of $t = 0$ at the same detector for the atom beam. Mechanical chopping of the beam is particularly useful for establishing the relative fractions of photons and metastable atoms in the beam, measured in the cumulative areas of the respective signals.

For a supersonic metastable atom source, to be discussed at greater length in Section 3.1.1, the velocity distribution P(v) is given by [70, 71]:

$$P(v)dv \propto v^3 \exp\left[-\frac{m(v-u(M))^2}{v_{th}^2(M)}\right] dv. \tag{2.1}$$

Here the average (flow) velocity u and local thermal velocity v_{th} both vary as a function of the final Mach number M. The time-of-flight experimental method does not measure this but a distribution of flux intensity in time, $I(t)$. The velocity distribution $P(v)$ is transformed using [14]:

$$\begin{aligned} v &= L_{TOF}/(t-t_0) \quad \text{and} \\ P(v)dv &= (L_{TOF}/t^2)I(t)dt \end{aligned} \tag{2.2}$$

into the intensity distribution $I(t)$ given by:

$$I(t) \propto (\frac{L_{TOF}}{tv_{th}})^5 \exp\left[-(\frac{L_{TOF}}{tv_{th}} - \frac{u}{v_{th}})^2\right]. \tag{2.3}$$

Using the same transformations (Equation 2.2) the collected time signal can be converted back into the beam velocity profile. This is used in this thesis to study

the velocity profile of the He* beam at each stage of the compact beamline and LVIS.

2.1.6 Deflection

A simple manipulation of metastable atoms using laser fields is to deflect the beam from the line of sight path from the source. This produces a beam (mostly) free of the background ground state and photon flux. Optical manipulation of an atom beam is discussed at greater length in the following Sections 2.2, 2.3 and 2.4.

2.1.7 Detection

The effect and efficiency of each of these beam modifying components is measured by a final detector. The energy contained in metastable states allows direct electronic measurement of individual atoms. The details of metastable atom detection are discussed in the final Section 2.5 of this Chapter.

2.2 Optical manipulation of atoms and beam brightening

From the point of view of a beamline, the significance of optical methods of manipulating atoms lies in beam slowing and beam brightening. This section commences with a 'back of the envelope' estimation to demonstrate why beam brightening is not only desirable but necessary with metastable helium beamline. Atom optics can selectively change degrees of freedom while maintaining others fixed since the light-atom interaction is essentially dissipative. Understanding how light forces can brighten an atom beam requires first defining what is meant by intensity, brightness and phase space density, and then how the 'brightness theorem' is violated in atom optics. The interaction of photons with atoms is reviewed first in the semi-classical two-level theory and the origin of the spontaneous (dissipative) and dipole (conservative) light forces. Then real multi-level systems such as metastable helium are considered in complex fields like a magneto-optical trap.

2.2.1 The necessity of beam brightening

Metastable helium experiments are dominated by the atom's very small mass. In collisions of any type the helium atom will receive an amount of momentum that, because of its low mass, translates as a very significant change in velocity. Strikes by

background gases, composed mostly of nitrogen and molecules of very much larger mass, will simply remove the He* atoms from the beam. Intra-atom collisions within the beam (predominantly at the source) contribute to the large beam divergence. Even the momentum recoil from the absorption/emission of a 1083 nm photon corresponds to a significant change in velocity of 9 cm/s.

The basic problem the element's mass raises is the range of velocities required of a He* beamline. At room temperature helium's velocity is about 2 km/s: with liquid nitrogen cooling of the source this is reduced to ~1 km/s. The reduction from this velocity to the few metres per second in a MOT using laser cooling requires over 10 thousand photon absorptions. Each corresponding photon emission contributes to the diffusion of the beam as the random direction of recoil momenta increase the velocity transverse to the direction of the He* beam.

As a rough estimate of this diffusion in the design of a He* beamline, for laser cooling an atom from an initial velocity 1000 m/s to a final velocity $v_{final} = 60$ m/s:

$$
\begin{array}{rcll}
\Delta v = & \text{1000 - 60} & = 940 & \text{m/s} \\
\text{number of scattered photons } N_{scatters} = & \Delta v / v_{recoil} & = 10444 & \\
\text{number of 'heating' photons } N_{heating} = & \sqrt{N_{scatters}} & = 102 & \\
v_{heating} = & \mathrm{N}_{heating} \times v_{recoil} & = 9.2 & \text{m/s} \\
\text{maximum divergence} = & v_{heating} / v_{final} & \simeq \frac{1}{7} & \text{rad}
\end{array}
$$

From this we infer that with even the best collimation of the metastable beam before deceleration the beam afterward be diverging and already expanded in diameter due to the accumulation of divergence and spreading over the length of the slowing region. A high brightness atom beam will require not only re-collimation but also compression. Furthermore some flux will be lost during slowing, as rapidly diverging atoms escape the laser beam along the slower length.

In first generation designs generous allowances in the efficiency of individual atom optic components produced He* beamlines that were very long. A 'second generation' machine like the ANU 'bright beam line machine' (BBM), which is discussed as an example in Sec 2.4, is still over three metres long, spread over two optical tables. The compact MOT loading He* beamline is intended to fit onto a single 2.4 m optical table, be simple to use and rapidly and efficiently load a large MOT.

2.2.2 Flux/intensity, brightness and phase space density

So far we have thought mostly in terms of some number of atoms passing by some marker or entering some region of the experiment, in other words a flux with units of number of particles per unit time. Properly speaking, however, this measurement is over a cross-sectional area, i.e. an intensity (number of particles per unit time

per unit area.) In practice we use the two terms interchangeably operating on the assumption that our 'unit area' is larger than the beam cross-section and the total flux, which is often what we are interested in, and the intensity are the same. Often we are concerned only with the on-axis collimated beam where the relevant area does not significantly change over the length of the experiment.

When considering the geometric properties of light the brightness of a beam is a more general property than its intensity because the former is independent of the distance between the source and the 'viewer' or detector. Any beam of light from a finite source is inherently divergent, as we know from Huygen's theorem in wave optics. The fixed, finite size of a detector will capture less and less of a beam flux as it is moved further away. A better measure of the beam is the amount of energy flowing into a given solid angle, or brightness, since this is a constant at any distance from the source. The equivalent unit for atoms is the number of particles per unit time per unit solid angle, and this is the sense in which beam brightness is used in this thesis[†].

A closely associated concept, but referring to particles instead of waves is the phase space density $\rho(\vec{r}, \vec{p}, t)$ of Hamiltonian-Lagrangian theory. If ρ is interpreted as a probability, then it is positive and normalized

$$\int \rho(\vec{r}, \vec{p}, t) d^3r d^3p = 1. \tag{2.4}$$

The integral of ρ over position yields the velocity distribution function $P(\vec{v})$, and the integration over momentum yields the density $n(\vec{r})$.

2.2.3 Liouville's Theorem, and its violation in atom optics

Liouville's theorem states that for a time independent, energy conserving (conservative force) Hamiltonian, the time evolution of $\rho(\vec{r}, \vec{p}, t)$ is conserved

$$\frac{d\rho(\vec{r}, \vec{p}, t)}{dt} = 0. \tag{2.5}$$

Phase space density cannot be changed, although it's distribution across the six degrees of freedom can be changed. Hence for a lens the position of photons are changed (focused) but requires the redistribution of momenta (divergence.)

[†]It has been noted in examination that there is variation in the use of these terms in atom optics, and that this is not necesarily a common definition. This is discussed further in Appendix A. However for the purposes of this thesis beam brightness is used to mean the measurement of the number of atoms per unit time per unit solid angle.

The difference with atom optics is that the forces involved need not be conservative and can be velocity dependent. Indeed the most fundamental interaction of photon and atom is inherently so, since photon absorption/emission is a resonant interaction that is dissipative, whereby the energy removed from the atom is proportional to the difference in Doppler shifted detuning from resonance between the absorbed and emitted photons. This opens the possibility of changing the phase space density or brightness of a beam of atoms.

2.2.4 Photon interactions with atoms

One of the basic models used in atom optics employs a semi-classical interaction of a light field with the electric dipole approximation of the transition between two energy levels of an atom. The strength of the interaction is measured by the Rabi frequency Ω combining the light electric field strength E_0 and the transition electric dipole d_{eg} (with the Rabi frequency spatial derivative split into real (q_r) and imaginary (q_i) parts for later convenience) [72]:

$$\Omega = \frac{-E_0 d_{eg}}{\hbar}, \qquad \frac{\partial \Omega}{\partial z} = (q_r + i q_i)\Omega. \tag{2.6}$$

The atom is described by the atomic density matrix with excited (e) and ground state (g) components. The equation for the light force is related to the Rabi frequency and the complex parts of the atomic density matrix ρ_{eg} [72]:

$$F = \hbar q_r(\Omega \rho_{eg}^* + \Omega^* \rho_{eg}) + i\hbar q_i(\Omega \rho_{eg}^* - \Omega^* \rho_{eg}). \tag{2.7}$$

This general result is indicative of two forces, proportional to the imaginary and real components of $\Omega \rho_{eg}^*$ respectively [72].

The first force can be identified with the absorption of a photon from the light field followed by the spontaneous emission of a photon in a random direction. This leads to momentum transfers from the field to the atom. Spontaneous emission results in random momenta recoils, which averaged over many cycles has zero net effect. The net 'spontaneous force' on the atom is then the product of the unit of momentum transfer $\hbar k$, the rate of spontaneous emission γ, and the probability of excited state population ρ_{ee} [72]:

$$F_{spon} = \hbar k \gamma \rho_{ee}. \tag{2.8}$$

The second force is related to the 'light shifts' that occur to the atomic energy levels when the atom is located in a light field. These are the result of stimulated

Parameter	Definition	Unit
Wavenumber	$k = 1/\lambda$	m^{-1}
Lifetime	τ	seconds
Photon energy	E_γ	eV,J
Electric dipole moment	$d_{eg} = e\langle e\|\vec{r}\|g\rangle$	
Effective magnetic moment	$\mu' = (g_e M_e - g_g M_g)\mu_{Bohr}$	
Spontaneous decay rate, linewidth	$\Gamma, \gamma = 1/\tau$	Hertz, rad/s
Power broadened linewidth	$\gamma' = \gamma\sqrt{1+s_0}$	rad/s
Detuning	$\delta = \omega_{laser} - \omega_{atom}$	Hertz, rad/s
Doppler shift	$\omega_D = -\vec{k}\cdot\vec{v}$	rad/s
Zeeman shift	$\Delta E = g\mu_B M B$	eV,J
Rabi frequency	$\Omega = -eE_0\langle e\|\vec{r}\|g\rangle/\hbar$	rad/s
Saturation parameter, on resonance	$s_0 = 2\|\Omega\|^2/\gamma^2 = I/I_0$	
Saturation Intensity	$I_s = \pi hc/3\lambda^3\tau$	watt/cm^2
Density operator	$\rho = \|\Psi\rangle\langle\Psi\|$	
Excited state density matrix element	$\rho_{ij} = \langle\phi_j\|\rho\|\phi_j\rangle$	
Scattering rate	$\gamma_p = \gamma\rho_{ee}$	Hertz

Table 2.1: Summary of optical parameters for semi-classical theory of atom-light interactions.

absorption/emission due to the imaginary off-diagonal components of the interaction Hamiltonian and imply that the eigenstates of the original non-interaction Hamiltonian are not those of the total Hamiltonian. Such light shifts depend on the amplitude of the optical electric field, and the 'dipole force' is proportional to the gradient of these shifts [72]:

$$F_{dip} = -\frac{\partial(\Delta E_g)}{\partial z} = \frac{\hbar\Omega}{2\delta}\frac{\partial\Omega}{\partial z}. \tag{2.9}$$

Such gradients arise in the change in amplitude produced, for example, by the interference of two far-detuned (no spontaneous emission) plane-wave light fields or at the foci of very high intensity fields. Thus in a standing wave composed of two counter-propagating far-detuned laser fields the period spatial modulation produces a force by the stimulated redistribution of photons from one beam to the other. Since the energy of these photons is the same this force is conservative, and cannot be used for cooling (although it can be used for localisation in the potential wells).

The common parameters of atom optics are listed in Table 2.1. In particular note the parameters useful in the laboratory, the saturation parameter and detuning. The spontaneous and dipole forces expressed in these terms are [72]:

$$F_{spon} = \frac{\hbar k s_0 \gamma/2}{1 + s_0 + (2\delta/\gamma)^2}, \tag{2.10}$$

$$F_{dip} = \frac{2\hbar k \delta_0 \sin 2kz}{1 + 4s_0 \cos^2 kz + (2\delta/\gamma)^2}. \tag{2.11}$$

The limit of on-resonant photon absorption of the spontaneous force is apparent on consideration of the $2\delta/\gamma$ term in the denominator in Eq 2.10. If the detuning is exclusively due to the atomic motion, the capture limit $v_c \equiv \gamma/k$ is the point at which the spontaneous force is significantly reduced by the Doppler shift. A consequence is that after a certain number of interactions with a light field an atom will be accelerated out of resonance with the light field. This limitation of laser cooling is overcome by the complicated nature of real atoms compared to this simple two-level theory, permitting manipulation of inner states of the atom to maintain the resonance condition.

2.2.5 Multi-level atoms

The simple two-level atom in this semi-classical model is complicated by the quantum mechanics of angular momentum and spin of the nucleus, core and outer shell electrons. These sub-states interact with external electric and magnetic fields and the angular momentum selection rules determine the strength of interactions with polarisation of the light field. It is largely by these details of the interaction that the basic force of Eq 2.10 can be applied to make the atom optical devices in Sec 2.3.

For most rare gas isotopes this picture is simplified by the absence of nuclear spin. The primary 1083 nm transition in helium between the 2^3S_1 effective ground state and the lowest energy J = 2 state of the $2^3P_{0,1,2}$ states, is shown in Fig 2.2. This 'simple' transition is between three magnetic sub-states in the ground state and five in the excited state. These sub-states are linked by the polarisation of the light field: $\Delta m = \pm 1$ by circularly polarized $\sigma^{\pm}$ light, $\Delta m = 0$ by linearly polarized π light, also illustrated in Fig 2.2.

Where the polarisation and quantisation axis is randomised the increased density of destination states reduces effective transition strength. In general this factor is the average of Clebsch Gordon co-efficients between the ground and excited states. This is particularly relevant where the atom interacts with multiple light fields, considered below.

Where the quantization axis is maintained and the atom interacts with a single polarization beam optical pumping can occur, that is $\sigma^{\pm}$ will pump the atoms toward higher/lower m_j-states until the highest/lowest ground sub-state is reached

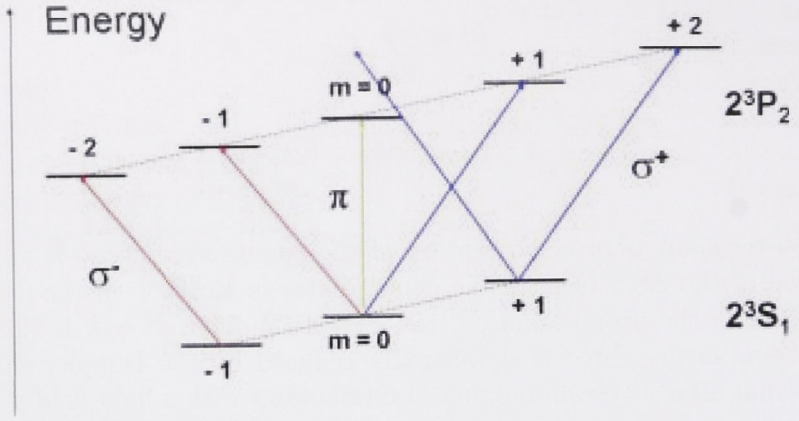

Figure 2.2: Multilevel atoms: the magnetic sub-states and optical transitions in He^* . In a magnetic field the Zeeman shift of the magnetic sub-states can be used to shift the atomic transition into resonance with a particular transition, in this example red detuned σ^- circular polarisation or blue detuned σ^+ circular polarisation.

(illustrated in Fig 2.2 for σ^+). Because the density of states for the end state of either transition is reduced to one the relative efficiency is raised compared to the interaction of random polarizations with random states.

It is specifically the energy shifts due to an electric field (Stark effect) or magnetic field (Zeeman effect) that permits the spatial variation of the spontaneous force that makes many atom optical devices effective. Figure 2.2 shows the Zeeman shift of the magnetic projection states of the 2^3S and 2^3P excited states:

$$\Delta E_{Zeeman} = -\mu' B_s, \tag{2.12}$$

$$\mu' = (g_e m_e - g_g m_g)\mu_{Bohr}, \tag{2.13}$$

where m_s and g_s are the magnetic quantum number and Landé g-factor of the ground and excited states, and B_s is the magnetic field strength in the direction of the quantisation axis.

The transitions are also detuned with respect to the $\Delta E = 0$ (π) transition fre-

quency: in this example σ^+, with a larger energy difference, is blue detuned and σ^- is red detuned. The result is that the atomic resonance will be closer to a photon energy in one polarisation. In Fig 2.2 this is illustrated by the resonant blue detuned σ^+ transition versus the out of resonance σ^- transition.

In an electric field an atom's polarisability α resulting from the angular momentum of a state produces the Stark shift [72]

$$\Delta E_{Stark} = \frac{1}{2}\alpha|\vec{E}|^2 \tag{2.14}$$

where $\vec{E}$ is a dc electric field. This polarisability is generally very small, requiring very strong electric fields, for the Stark effect to be practical for any but a few atomic species. The Stark effect has no particular application in this thesis.

2.2.6 Multiple light fields

The spatial sensitivity achieved by Zeeman or Stark detuning can be further enhanced with the directional sensitivity of multiple light fields. In the simplest configuration an atom in two opposed beams will experience two opposed forces, Eq 2.10, with $\delta = \delta_{laser} + \omega_{Doppler}$, where $\omega_{Doppler} = kv$. The forces balance only for atoms with zero velocity in the direction of the light fields. When the laser is red detuned, $\delta_{laser} = -|\delta_{laser}|$, then the force opposes the motion of the atom in the case known as 'optical molasses'. In one dimension:

$$F_\pm = \pm\hbar k\frac{\gamma}{2}\frac{s_0}{1 + s_0 + [2(\delta \mp |\omega_D|)/\gamma]^2}, \tag{2.15}$$

$$F_{OM} \simeq \frac{8\hbar k^2 \delta s_0 \vec{v}}{\gamma(1 + s_0 + (2\delta/\gamma)^2)^2} \equiv -\beta\vec{v}. \tag{2.16}$$

This friction force is therefore cooling in this dimension. Optical molasses in one or two dimensions form the most basic atom optical device, collimating a beam of atoms to the axis orthogonal to the beams. Hence 'collimators' are fundamentally beam brightening, reducing the divergence of an atom beam.

Optical molasses are dissipative but not spatially dependent: a collimated atom beam will emerge from molasses with the spatial width (approximately) the divergent beam entered them. In particular the optical force is not central, optical molasses in three dimensions will cool but will not trap atoms. A central force in two or three dimensions is achieved by adding the polarisation selectivity of the Zeeman effect considered above. A quadrupole magnetic field, illustrated in one dimension

in Fig 2.3, increases approximately linearly from a centre. As in Figure 2.2, an atom at $x < 0$ will be shifted into resonance with σ^- light and experience a force toward the centre. The reversal of the field at $x > 0$ brings the atom more into resonance with the opposing σ^+ beam.

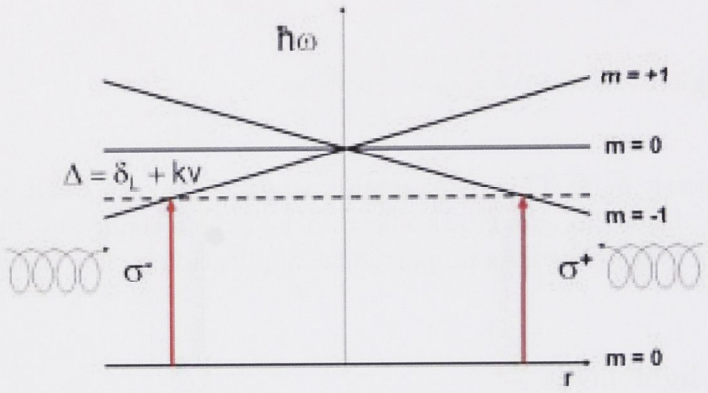

Figure 2.3: The one dimensional magnetic field profile used in a magneto-optical trap. The reversing magnetic field changes the polarisation of the light closest to resonance, thus changing the direction of the light force.

The result is a force both cooling and central, with a resonant detuning $-|\delta_{laser}| + kv - \mu' B(r)$, making a magneto-optical lens in two dimensions or a magneto-optical trap (MOT) in three dimensions. Again, as essentially dissipative, 2D- and 3D-MOTs can increase brightness or phase space density. Examples of each in the ANU bright beam machine (Sec 2.4) and compact beamline (Chapters 4and 5) will be extensively considered in this thesis.

The superposition of polarizations in 2D or 3D light fields, such as the magneto-optical trap, has the effect of reducing the overall saturation intensity as the atoms randomly interact with different quantization axes. That is the effect of optical pumping in one axis randomizes the m_j projection state in the other axes, effectively anti-optical pumping.

The reduced saturation factor must lie somewhere between the average of squares of Clebsch-Gordan coefficients (0.56 for the J = 1 to J = 2 transition) and unity. It is commonly empirically assumed to be 0.8 ± 0.2 as the widest possible range of physical values [16, 73, 74]. Javanainen [75] notes that the atomic population among the Zeeman states may be distributed differently by optical pumping at low

$j_l \rightarrow j_2$	α	β	x_r	α	β	x_r
		lin $\perp$ lin			MOT	
$0 \rightarrow 1$	0.994	1.311	0.729	1.007	1.28	2 0.841
$1 \rightarrow 2$	1.191	1.620	0.632	1.259	1.620	1.045

Table 2.2: Coefficients α, β and x_r for three dimensional molasses in basic MOT and lin $\perp$ lin configurations.

and high intensity. Then the effective Clebsch-Gordan coefficient finally depends on the total intensity and on the spatial distributions of both light field energy and polarization. The excited state fraction ρ_{ee} in Eq 2.8 is modified by the ansatz equations:

$$x = \frac{(I/I_s)\Gamma^2}{4\delta^2 + \Gamma^2}, \tag{2.17}$$

$$y = \left[\left(\frac{1}{\alpha} - \frac{1}{\beta}\right)\frac{x_r}{x + x_r} + \frac{1}{\beta}\right] x, \tag{2.18}$$

$$\rho_{ee} = \frac{y}{1 + 2y}. \tag{2.19}$$

The fitted values of α, β and x_r derived in Ref [75] are given in Table 2.2 for the two most common optical configurations, the 3D $\sigma^+\sigma^-$MOT and lin $\perp$ lin molasses. Then according to Javanainen,

> "Qualitatively $1/\alpha^{1/2}$ and $1/\beta^{1/2}$ are the effective Clebsch- Gordan coefficients at low and high intensity, and x_r is the roll-over saturation parameter at which the switch takes place.
>
> Put in another way, at low and high intensities the excited-state fraction behaves as in the standard two-state models with the respective saturation intensities αI_s and βI_s."

Using this theory Javanainen calculates this factor to be $C = 0.838 \pm 0.075$ [75], well within and significantly more precise than the empirical ansatz quoted above.

2.3 Manipulating atom velocity

It was discussed in Section 2.2 how an optical force can be applied to manipulate an ensemble of atoms. In particular a strong force is derived from the 'scattering' or 'spontaneous' force

$$F = \hbar k \Gamma \rho_{ee}. \tag{2.20}$$

However a central problem of any application of this force with a narrow band laser field with linewidth γ is that a small number of photon scatters alters the velocity of the atom, hence changing its Doppler shift ω_D, taking the atom out of resonance. The resonance condition

$$|\delta + \omega_D| = |\omega_l - \omega_a + \omega_D| << \gamma, \tag{2.21}$$

allows methods based on each of the three parameters to compensate for the Doppler shift: the laser frequency ω_l, the atomic resonant frequency ω_a, and the laser linewidth γ. This section overviews the application of these methods in atom optic devices for for manipulating atoms and atom velocity. The following section considers the application of these techniques in the ANU bright beam machine as an example for adoption in later chapters to create the compact MOT loading beamline.

2.3.1 Broadband Light

Compensation for the changing Doppler shift is unnecessary if the light field is not spectrally narrow but intense ($I > I_s$) over the width from ω_a to $(\omega_a - \vec{k}\vec{v_0})$. Then the atom will be in resonance at any velocity below v_0. This idea of 'white light' cooling was first proposed by Hoffnagle [76].

Figure 2.4 shows the effect of broadening the normal linewidth of the SDL 6702-HI diode laser used in the bright beam machine by frequency modulating the current of the diode laser. The spectral width of the modulation broadened beam is equivalent to a capture range of almost 400 m/s. The broadband effect is easily switched by reducing the intensity of the signal producing the modulation of the diode current (for practical purposes this signal could not be simply turned off). Hence 'low power white noise' is almost equivalent to the normal linewidth of the laser.

The disadvantage of this white light source is that the maintenance of spectral density (I_s/γ) at all velocities requires much more light power. This can be easily seen in the Fig 2.4 where the same laser diode is used in both spectra. The increase

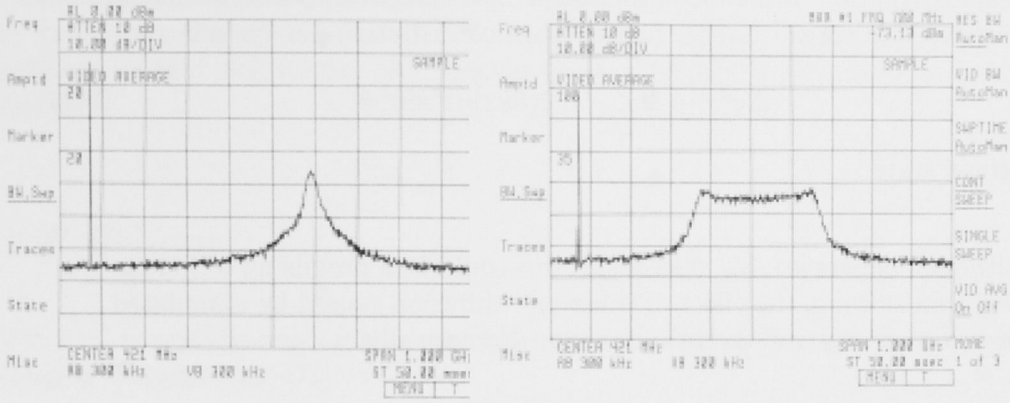

(a) (b)

Figure 2.4: Spectrum analyser measurement of the the SDL 6702-HI diode laser's linewidth: the laser's normal linewidth $\sim 2-3$ MHz with 'low power' frequency modulation (a); and the broadened $\sim$ 30 MHz width with 'high power' frequency modulation.

in spectral width from $\sim 2-3$ MHz to ~ 30 MHz is achieved with a corresponding decrease of ~ 5 dB in peak intensity. Although this method has been demonstrated several times with atoms [77, 78] including helium [79] and ions [80] it is generally impractical because of too much power is required to maintain spectral density.

2.3.2 Isotropic light

A similar broad capture velocity technique was demonstrated slowing sodium [81] and rubidium [82] atoms using isotropic light. Using a special material with very high diffuse reflectivity as an enhancement cavity filled with diffuse light, the changing Doppler shift as atoms slow is compensated by the preferential absorption of photons at varying angle to the direction of motion, or continuous "angle tuned slowing".

$$\omega_a = kv\cos\theta \tag{2.22}$$

Below a cut-off velocity $v_f = (\omega_a - \omega_l)/k \equiv \delta/k$ the light is off-resonant and decelleration is slower. Hence the atoms preferentially absorb photons from a ring $\cos\theta = v_f/v$ so that the decelleration is

$$a = a_0\cos\theta = a_0 v_f/v, \quad \text{where} \quad a_0 = \hbar k\gamma/m \tag{2.23}$$

However the study the isotropic slowing effect for Ne^* in a small cavity with low laser powers highlights the problem of stimulated diffusion in this technique [83]. While the perpendicular component of the recoil momentum averages to zero, the

statistical distribution of the azimuthal angle of the aborbed photons increases the transverse velocity spread $\langle \Delta v_\perp^2 \rangle$. The average contribution per cycle is

$$\langle \Delta v_\perp^2 \rangle_i = 2v_{r,\perp}^2 = 2(\hbar k/m)^2 \sin^2 \theta \tag{2.24}$$

The authors state

> Although papers [81, 82] stated that this could be a promising technique for beam slowing, the effect of transverse diffusion caused by stimulated emission can destroy the beam quality dramatically.

In particular the inverse dependence on mass in Eq. 2.24 means that the effect of transverse diffusion will be most pronounced for metastable helium.

2.3.3 Bichromatic Light

The bichromatic force arises from two beams of equal intensity and symmetrical detuning from a two-level atomic resonance. The process can be characterised as stimulated absorption from one beam followed by stimulated emission into the other by alternate π-pulses [84]. This stimulated cycle period T is faster than that limited by the spontaneous emission lifetime τ, and counterpropagating beam alignment means there are two directed momentum recoils per cycle. Hence the bichromatic force

$$F_{bi} = 2\hbar k/T \quad 1/T = \delta/\pi \tag{2.25}$$

is many times stronger than the spontaneous force (Eq. 2.10), with a velocity capture range the order of the the frequency separation between the two beams, $2\delta/k$.

The bichromatic light in the atomic reference frame requires four frequencies in the laboratory rest frame for atom beam slowing. This was first demonstrated in 1997 with the beams transmitted through the rear wall of a cesium oven [84]. The atoms were slowed by several tens of m/s in a 10 cm interaction length.

Bichromatic deflection and slowing was demonstrated with metastable helium in 2001 [85]. Atoms from a LN_2 cooled He^* source were slowed by $\sim$ 100 m/s in an interaction length of 20 mm by bichromatic beams aligned a 3° to the atomic beam.

In principle the 1 W optical power available at 1083 nm from fibre amplification means the bichromatic force could stop a LN_2 temperature He^* beam in less than 1 cm [85]. In practice this has been difficult to realise. In 2004 refinements to the apparatus in Ref. [85], including in vacuo mirrors to reduce the alignment angle to 1°, achieved $\sim$ 300 m/s slowing [86], still well above MOT capture velocities even from a LHe cooled source.

In addition to the mechanical difficulty of aligning the atomic and laser beams, the three magnetic substates of the 2^3P state interact with varying strengths to the birchromatic field [86], further reducing the slower efficiency in the short interaction length.

2.3.4 Chirping

'Chirping' is rapidly varying the laser frequency in a sweep that follows the atoms changing Doppler shift [72]

$$\dot{\omega_l} = -\dot{\omega_D} < \omega_r \gamma. \tag{2.26}$$

The method is easily implemented with diode laser sources by similar electronics to that discussed above for the white light broadening. However the cyclical rather than continuous slowing limits the efficiency of slow atom production, which is a problem with a species like helium. The atoms arrive in pulses at intervals a few times the shortest deceleration interval $t_{min} = \bar{v}/a_{max}$. Hence the efficiency e of chirping is the total number n of photon absorption cycles to slow an atom divided by the number of cycles in this interval $t_{min}/2\tau$:

$$e = \frac{2n\tau}{t_{min}} = \frac{2v_r}{v_c}\frac{\tau}{t_{min}}. \tag{2.27}$$

Using the values for helium, $v_r = 9.0$ cm/s, velocity $v_c = 1.76$ m/s, $\tau = 98$ ns, $t_{min} = 0.34$ s, the efficiency $e = 6 \times 10^{-8}$ is clearly unsuitable for any practical application.

2.3.5 Stark slowing

The remaining methods compensate for the changing Doppler shift by changing the atomic transition frequency ω_a. The Stark shift introduced in Sec 2.2.5 can compensate the changing Doppler shift by changing the energy level in an inhomogeneous electric field

$$E(z) = E_0\sqrt{1 - \sqrt{1 - \frac{z}{z_0}}} \tag{2.28}$$

where z_0 is the length of the slowing field. This method is limited by the relatively low Stark shifts of the low-lying excited states that have sufficiently large linewidths to achieve adequate deceleration. Together with the requirement for very large electric fields this limits the Stark method for all but a few elements, including metastable helium.

Slowing of He* has been demonstrated using the Stark shift of the 3^3P state and 389 nm transition from 2^3S state [87]. However this is not a closed two-level transition, and the decay via the 3^3S state populates the m=0 ground state that is no longer coupled to the cooling level by selection rules. At high electirc fields this becomes a dark state that captures all atoms after about 30 absorption-emission cycles. This is overcome by a weak magnetic field perpendicular to the electric field that mixes the magnetic substates [87]. Overall the authors deduce a deceleration of atoms starting from about 850 m/s down to a velocity of 175 m/s.

In 2003 this apparatus, with significant modification, was used to slow atoms to $\sim$ 55 m/s, for capture in a MOT [35]. The He* flux exiting the Stark slower is undetermined, but relatively low as infered from the small size of the He* MOT (see Table 1.1).

2.3.6 Zeeman slowing

The most common method of compensating for changing Doppler shifts in multilevel atoms is to shift the energy levels of the Zeeman sub-states with a spatially varying magnetic field. The Zeeman slower has become common place for its simplicity of design and construction and efficient operation. In traditional Zeeman slowing, the changing Doppler shift experienced by the atoms being slowed is compensated for by a spatially varying magnetic field keeping the atoms in resonance with a counter-propagating laser beam. For a uniform deceleration $a = \eta a_{max}$ with efficiency design parameter $\eta \leq 1$ ($a_{max} = 0.469 \times 10^6$ m/s^2 [72],

$$\delta = \delta_0 + kv - \mu' B(z)/\hbar \tag{2.29}$$

$$B(z) = B_b \pm B_t \sqrt{1 - z/z_0} \tag{2.30}$$

$$F = \frac{\hbar k \Gamma}{2} \frac{s_0}{1 + s_0 + 4(\delta_0 + kv - \mu' B(z)/\hbar)^2/\Gamma^2} \tag{2.31}$$

where the positive (negative) sign applies to σ^+ (σ^-) slowing, B_b constant bias field, B_t peak (equals B_b in this case). There are two substantive issues for consideration in the design of a Zeeman slower.

First is the design parameter η. Using circularly polarised light optically pumps the

atoms into the optimally tuned resonant state. The efficiency of the Zeeman slower, i.e. the maximisation of the force (Eq 2.31) at each point, is then dominated by the interplay of the laser intensity s_0 and the precision of the magnetic field (Eq 2.30). The design parameter determines the length of the magnet z_0. This is usually chosen to compensate for the inaccuracies of the magnetic field produced in a solenoid compared with the theoretical profile of Eq. 2.30, by allowing a longer length and hence more time for photon interactions to occur at a given Doppler shift. In addition Zeeman slower designs often include power broadening for the same reason, increasing absorption away from the resonant frequency.

Second is the choice to be made of the sign in Eq. 2.30. The two primary options are a σ^+ slower using a decreasing magnetic field, and a σ^- slower using an increasing magnetic field. The former suffers a number of set backs: the zero or near zero field at the exit means that the atoms exiting the slower are still in resonance with the slowing laser and may continue to be slowed, be stopped or even pushed back into the slower. The problem of poor extraction efficiency is exacerbated when the slower feeds a magneto-optical trap: forming a MOT at the centre of the atomic beam is also in the centre of the near resonant slowing beam, subject to substantial radiation pressure.

A variety of solutions to each of these problems have been trialled: extraction coils [88, 33]; a small amount of reversed σ^- slowing [66, 14, 89]; formation of the trap off-axis; a 'dark-spot in the middle of the slowing beam [90]; and using a mirror with a small hole in the middle for injection of the slowing beam in front of the MOT [66]. The reversing field technique, where the large detuning rapidly moves out of resonance as the magnetic field rapidly drops to zero, is common with metastable helium beamline including the ANU bright beam machine [14, 66].

2.4 The ANU bright beam machine: collimation, deceleration and brightening

The design for the existing beamline at the Australian National University is illustrated in Figure 2.5. This 'bright beam machine' produces a relatively slow, intense, collimated He* beam using three main atom-optical components [91].

First the diverging atom beam from a LN_2 cooled source[†] is first collimated in 2 dimensions using 5×30 cm mirrors inclined at a small angle to the beam axis. The effect of mirror inclination and the angle of laser entry is a gradual change in the crossing angle making a 'curved wavefront', slowly retuning the transverse Doppler shift of this laser to follow the changes in velocity of the atoms [92]. This maximises

[†]Note that this is the source design in [93] and Fig 3.3.

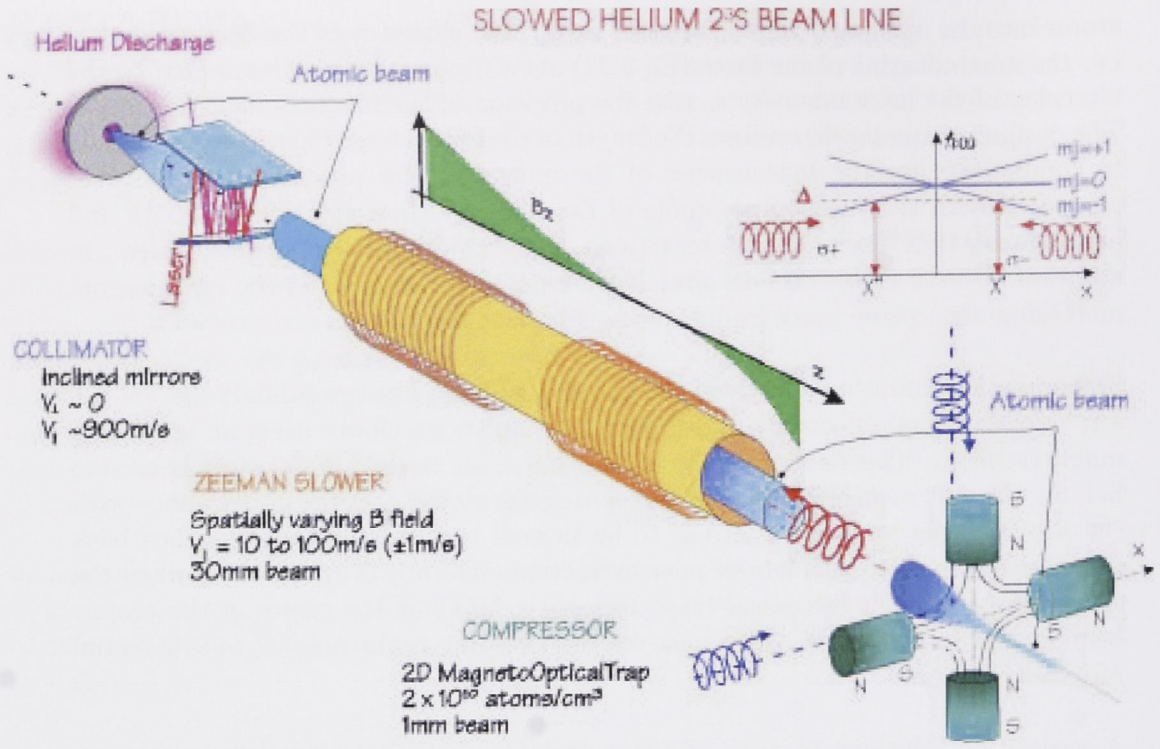

Figure 2.5: The bright beamline at ANU showing the collimation, slowing and compression of the atom beam from the discharge source. Image from [66].

the efficiency of both capturing atoms in the beam and their collimation. The result is a well collimated beam of about 1 cm diameter.

The He* beam is slowed from ~1 km/s by a standard design reversing field Zeeman slower. The slowly varying magnetic field tunes the Zeeman shift to the changing Doppler shift as the atoms are slowed down. As noted in Sec 2.2.1 the atomic beam broadens with transverse heating. Atoms which exit the side of the slowing laser beam are beyond retrieval and lost to background gases. Hence the exiting atomic beam at the end of the end of the magnetic coils is essentially the diameter of the laser beam, which in this case is ~30 mm.

The loss of atoms during deceleration can be reduced by a couple of refinements. The slight focusing of the laser beam provides a degree of cooling transverse to the beam axis. This can be assisted by a transverse cooling element at the junction between the magnetic field coils where the field is reversed, although this is not currently used in the ANU beamline.

The last component of the beamline is a 2-D magneto optical trap, although this is

an inadequate description the 'compressor' [94]. Unlike the molasses field formed by the collimator, which removes kinetic energy of the atom in the plane of the lasers, a 2-D MOT both does this by default and applies a restoring force to a beam axis. In order to avoid simply strong focusing of the atomic beam, the compressor is actually a pair of 2-D MOTs, or an atomic telescope, reducing the beam size to about one millimetre. This uses a single recycled laser beam for the two 2-D interaction zones, guided by the mirrors supported by this unit, which is fitted inside a purpose built vacuum chamber. The two quadrupole fields are derived from two arrays of rare earth solid magnetic mounted outside this vacuum chamber.

In practice it was found that the efficiency of the compressor is enhanced by the implementation of two additional Doppler cooling collimation stages. A 50 mm optical molasses stage collimates the beam entering the compressor, maximizing the captured flux and the transmission efficiency from the Zeeman slower.

A 5 mm stage after the compressor removes the slight remnant focus (< 10 mrad) of the atomic beam exiting the compressor and hence minimizes the spread of the beam where the experimental stages sit 20 to 70 cm downstream. The bright He^* beam produced by this machine contains some 10^9 atoms per second at velocities less than 100 m/s in a narrow beam.

The applications of the bright beam machine may, and has, include loading a magneto-optical trap. Certainly this is capable of maintaining a large (10^9 atoms) He^* MOT [27], but it is a complicated beam machine to operate in order to so do. Neither does a MOT truly utilize the advantages of such a bright atomic beam. Hence ultimately the bright beam machine is really intended for more sophisticated beam experiments, such as the guiding experiments using hollow optical fibres [95] or cross beam apparatus electron scattering experiments to measure the differential cross-section.

2.5 Detection of metastable atoms

Typically the presence and properties of atoms are measured optically by absorption (absorption measurement) or emission (fluorescence measurement) of photons. As seen below in Sec 2.5.1 ordinarily detectable light powers require large numbers of atoms. Alternatively, the ability to detect single neutral atoms by electronic methods is a property unique to metastable states of rare gases. When metastable atoms strike a surface the release of internal energy upon de-excitation causes an electron to be ejected from the surface. If the electrons emitted by a surface do not recombine with that surface the detection of the neutral atom can proceed by readily measuring the electron current, as discussed in Sec 2.5.1. Both optical and electronic methods of detection are employed in this thesis to measure properties of the compact LHe He* beamline.

2.5.1 Atom detection by fluorescence measurement

Recent advances in the sensitivity of photo-electric devices to infra-red light have produced a 'quantum leap' in optical detection of metastable helium in atom optics. For more than ten years a second wavelength laser that excited the 588 nm transition from the 2^3P state was required in order to readily visualise He* beams or traps [13]. The reason for this poor performance was simple. Any photo-electric device has a peaked sensitivity profile, like that in Fig 2.7. While these devices were engineered to provide optimum response in the visible wavelength range, the response in the low energy infra-red was very poor, typically less than one percent.

A practical outcome of this, for example, is that the imaged He* MOT of several million atoms is only barely visible with an an ordinary silicon-based CCD camera. This excludes most of the atom clouds in Table 1.1, a fact that alludes to one reason for the protracted development history of He* traps. Put simply, once a great effort was required to confirm the presence of trapped atoms in the first place before considering optimisation of an apparatus. Today the situation is much improved by a new class of devices, and a MOT apparatus can be started, working and optimised in a few minutes because of the direct information about the atom cloud now available.

The following discusses the photodiode and CCD camera used to non-destructively measure the He* MOT. A high resolution ultra-sensitive infra-red detector was built for fluorescence detection. This combines a Thorlabs FGA10 Indium-Gallium-Arsenide photodiode, with increased sensitivity in the infra-red, and a pre-production amplifier from Texas Instruments with an ultra-high gain-bandwidth product (GBP), employed in a simple current sensitive amplification circuit. A Hitachi KP-160 1/2" frame transfer CCD camera (now discontinued) is used for imaging.

The basic photodiode detection circuit involves the sensitive detection and amplification of the small amount of charge produced across the photodiode due to the light incident upon it. A back-of-the-envelope calculation assuming a unity quantum efficiency (i.e. one electron produced for each photon, an optimistic assumption), a maximum rate of fluorescence, $\Gamma/2$, and the experiment geometry, gives just short of a nanoampere to be detected for a moderate MOT of twenty million atoms. Not only does this need to be linearly amplified to around the 1 V range, but done so with a bandwidth which is still useful. The typical time scale for measurements may be fractions of a millisecond, so the minimum acceptable bandwidth is of order 100 kHz, requiring a very high ($10^9 - 10^{10}$) Gain-Bandwidth-Product (GBP) amplifier. This is now calculated in detail.

The typical quantum efficiency (QE) of a silicon based photo-electric semiconductor at 1083 nm is an order of magnitude less than unity or worse. For an analog device such as a photodiode this is measured by the current produced by the power of light incident on the device, or 'responsivity' R, related to quantum efficiency via the photon energy E_γ by $R = QE \times E_\gamma$. Such a poor responsivity means that optical detection of He* starts on the back foot.

Over the past few years the responsivity of photodiodes and CCD arrays has been improved by an order of magnitude. This has been driven by a commercial demand in the security industry for infrared sensitive detectors and cameras for use at night. For example the Hitachi KP-160 CCD camera's 'sensitivity' ($S = R/R_{max}$) specification is reproduced in Fig 2.7, showing a sensitivity of 10-15% at 1083 nm, compared with $\ll 3\%$ for standard CCD cameras.

The best silicon photodiode at ANU has been calibrated at $R = 0.18$ A/W or 20.5% quantum efficiency at 1083 nm. The new generation Indium-Galium-Arsenide photodiodes offer substantially improved performance. The ANU has two low capacity, high speed Thorlabs FGA10 InGaAs photodiodes with a specified responsivity of 0.7 A/W at the He* transition wavelength of 1083 nm and minimum 40 MHz bandwidth. The installed diode was calibrated as 0.572 A/W. The calibrated responsivity and corresponding quantum efficiency of the three available photodiodes is given in Table 2.3. Compared with even the best silicon based diode the InGaAs diode gives a better than threefold increase in signal.

The basic circuit for amplification of a photodiode signal is a trans-impedance amplifier, shown in Fig 2.6. The output voltage $V_o = R_f I_D$ is directly proportional to the input current with the circuit gain given by the feedback resistance: $G = R_f = R_1(1 + VR_1/R_2)$. The diode capacitance C_D (which includes the op-amp input capacitance C_A) is fixed and the trans-impedance gain set through the feedback resistance R_f. Then the frequency response may be controlled through

Photodiode	$R(A/W)$	QE
InGaAs (1)	0.572	65.2%
InGaAs (2)	0.630	71.8%
Silicon	0.18	20.5%

Table 2.3: Calibrated responsivity and quantum efficiency values for each of the two purchased InGaAs photodiodes, compared with the highest sensitivity Silicon photodiode at 1083 nm.

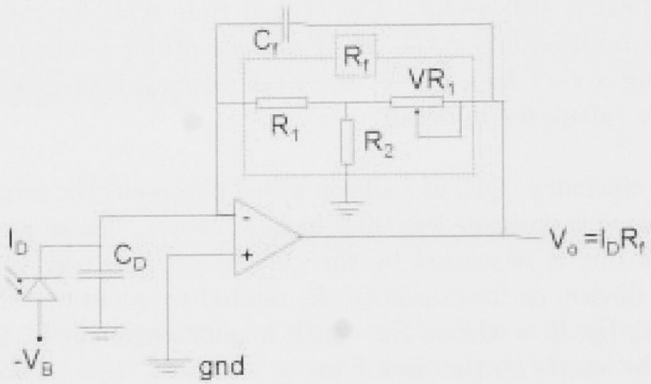

Figure 2.6: Trans-impedance circuit made to amplify current from the photodiode. The gain is given by the feedback resistor R_f, and the frequency response is controlled by the feedback capacitor C_f.

the feedback capacitor C_f. For a maximally flat frequency response the feedback capacitance is chosen such that

$$1/(2\pi R_f C_f) = \sqrt{GPB/(4\pi R_f C_D)}. \tag{2.32}$$

The -3dB bandwidth is approximately:

$$f_{-3dB} = \sqrt{GPB/(2R_f C_t)}. \tag{2.33}$$

where C_t is the total capacitance $C_D + C_A + C_f$. Continuing with the optimistic calculation, the FGA10 photodiode has a capacitance of 85 pF, so a gain of 10^9 at 100 kHz bandwidth would require a 10 GHz Gain-Bandwidth-Product amplifier!

R_1	R_2	VR_1	C_D	C_A	C_f
1 MΩ	0.5 kΩ	100 kΩ	85 pF	5.2 pF	1 pF

$G = R_f(max)$	-3dB	$G_{calibrated}$
201 MΩ	209 kHz	197.7 MΩ

Table 2.4: The trans-impedance circuit component values used in the gain circuit in Fig 2.6, together with the corresponding theoretical and calibrated gain measured in Ohm.

Atom No.	$P_{incident}$	V_{out}
10^6	0.04 nW	5 mV
10^9	40 nW	5V[a]

Table 2.5: Calculated performance of the photodiode and amplification circuit for specified components and experimental geometry.

[a]Note the OPA657 has an operating range of ±5 V.

The best operational amplifier even approaching this level of performance is the new Texas Instruments OPA657 op-amp. With an exceptional 1.6 GHz gain bandwidth product, very low level signals can be significantly amplified in a single stage circuit design. With very low input noise (4.8 nV/$\sqrt{Hz}$) very large gains can be made over high bandwidths before this noise is peaked up by the photodiode source capacitance. Hence using the OPA657 with the component values listed in Table 2.4 the photodiode circuit responds with a minimum -3dB bandwidth of 209 kHz at a maximum gain of 201×10^6. Including all the reductions due to quantum efficiency, geometry, reflective losses, etc., this detector gives a linear signal range from millivolts to volts for the interesting range of MOT atom number, Table 2.5.

The components were assembled on a manufactured printed circuit board (PCB), with a smooth power supply at ±5 V supplied by solid state rectifiers with noise on the output capacitively filtered to ground. The PCB is mounted in a die-cast case using π filters to reduce the entrance of RF noise via the power connections. Although the photodiode was not run with a bias voltage the cathode was connected to the ground plane of the PCB in a twisted pair with the anode signal to minimise ground loops and shield the small input signal. The output signal was also connected by twisted pair to the SMB/SMC connector to reduce any likelihood of noise pickup on the signal. The trans-impedance circuit was calibrated with a gain of 197.7×10^6 using a controlled nanocurrent source.

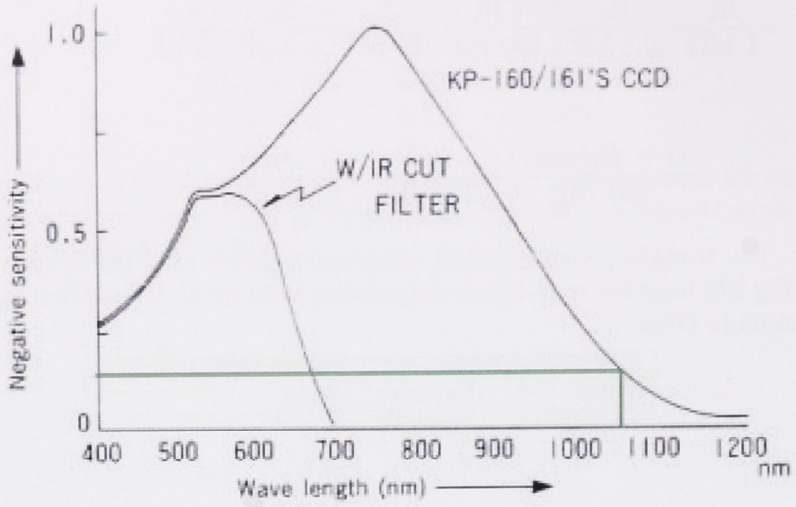

Figure 2.7: Spectral response from the specification of the Hitachi KP 160 CCD camera: the peak of sensitivity ($S = R/R_{max}$) is shown to be shifted significantly to the infrared (~780 nm) and although it drops off the sensitivity at 1083 nm is still 10-15% compared with $< 3\%$ for standard CCD camera. (Note: sensitivity is 'negative' because the photoelectric device produces electrons.)

Imaging

Similar considerations about the IR performance of devices affect imaging of the He* MOT cloud. The peaked responsivity shape of Fig 2.7 is typical of charge coupled devices (CCDs) and since these were first designed for visible wavelengths the response in even the near-infrared was relatively poor. Typically at the He* transition wavelength 1083 nm this was merely the one or two percent left in the wings of the responsivity/sensitivity curve.

The market for night-time video surveillance cameras has steadily pushed the improvement in performance of CCD devices in the infrared. In the late 1990's a new generation of devices were produced with an order of magnitude improved response in the far infra-red. The Hitachi KP-160 CCD is an example of these. Figure 2.7 shows the normalised responsivity (or negative sensitivity) specification of this CCD camera. The peak is shifted to the near-IR, about 780 nm, so that the responsivity at 1083 nm is well within the normal range of the device. Reading from this plot the sensitivity is 10-15% at 1083 nm wavelength.

For either fluorescence or absorption measurements the scattered optical power P is directly proportional to the number of atoms contained in the light fields. In either method the atoms randomly scatter photons from a directed beam into the total 4π solid angle. In absorption measurements the loss of power from the laser beam will then be a measure of the number of atoms in its path. In fluorescence measurements the probability of detection of a particular scattered photon is a geometrical factor, the fraction of 4π of solid angle Ω subtended by the detector.

The atom number is calculated from the photodiode fluorescence measurement, recorded as the peak to baseline voltage difference. The voltage is converted to the power measured by the photodiode using the amplifier gain G and the photodiode quantum efficiency

$$P_{PD} = \frac{V_{PD}}{QE \times G} = \frac{V_{PD}}{R_{cal} E_\gamma G}. \tag{2.34}$$

where R_{cal} is the responsivity of the photodiode and the photon energy $E_\gamma = 1.14$ eV, using the calibrated values for each photodiode used in the experiment in Table 2.3. The atom number is then calculated from

$$N_{atoms} = \frac{P_{PD}}{f_\Omega E_\gamma \gamma_p (1 - RL)} \tag{2.35}$$

using the 'geometric' factors subtended solid angle fraction ($f_\Omega = 3.36 \times 10^{-4}$) and reflective losses (RL=10%).

The scattering rate in a single light field is usually given in terms of the spontaneous decay rate and excited state population:

$$\gamma_p = \Gamma \rho_{ee} = \frac{\Gamma}{2} \frac{s}{1 + s + (2\delta/\gamma)^2}. \tag{2.36}$$

For high saturation parameters $s \geq 1$ and low detunings $\delta \sim \gamma$ the excited state population saturates at fifty percent, and the saturated optical power is $E_\gamma \Gamma / 2N$.

Equation 2.36 needs to be modified for use in a three dimensional magneto-optical trap where the intensity and polarisation of the light field varies [74]. The total intensity is multiplied by dimensionality $\mathcal{N}$ of the molasses, but the saturation is

effectively reduced by the reduced coupling due to the variation of polarisation and magnetic field. An effective Clebsch-Gordan coefficient may depend on the populations of and coherences between each Zeeman state of the atom, the "anti-optical pumping" discussed in Sec 2.2.6. Hence the intensity is replaced with an empirical equation $2\mathcal{N}Cs$, where the phenomenological factor $C \leq 1$ accounts for the reduced saturation effect [16, 73, 74]. In the experiments in References [16] and [73] C is chosen as 0.8 ± 0.2 to represent the broadest range of possible physical values, between the average of squares of Clebsch-Gordan coefficients (0.56 for the J = 1 to J = 2 transition) and unity. As noted in Sec 2.2.6 Javanainen calculates this factor to be $C = 0.838 \pm 0.075$, well within and significantly more precise than this empirical ansatz [75].

Time of Flight measurement of temperature

The temperature of an atom cloud can be derived from its expansion when released. From Ehrenfest theorem of ordinary kinematics the expectation values of the cloud radius at two times in the expansion(0 and t) are related by

$$\langle \vec{r}^{\,2} \rangle_t = \langle \vec{r}^{\,2} \rangle_0 + \left\langle \frac{2\vec{r} \cdot \vec{p}\, t}{m} \right\rangle_0 + \left\langle \frac{\vec{r}^{\,2} t^2}{m^2} \right\rangle_0 \tag{2.37}$$

The middle term on the right is zero as there is no correlation between momenta and location. Using the equipartition theorem, and a Gaussian spatial distribution $n(\vec{r}) = n_o \exp(-r^2/2\sigma_0^2)$, so that $\langle \vec{r}^{\,2} \rangle = 3\sigma_0^2$, this becomes

$$\sigma_t = \sqrt{\sigma_v^2 t^2 + \sigma_0^2}, \text{ or} \tag{2.38}$$

$$\sigma(t) = \sigma_0 \sqrt{1 + \frac{k_B T}{m\sigma_0^2} t^2} \tag{2.39}$$

where the cloud temperature is $T = \frac{m}{k_b}\sigma_v^2$ [96].

The DAQ system described in Sec 5.2 can collect images of the atomic cloud at any time t after the MOT is released by switching off the magnetic and light fields. From these images we derive the Gaussian radii $\sigma_z(t)$ and $\sigma_\rho(t)$ for the strong and weak axes respectively, and hence the respective temperatures. Equation (2.39),

$$\sigma_t^2 = \sigma_v^2 t^2 + \sigma_0^2 \tag{2.40}$$

is linear in $y = \sigma_t^2$ and $x = t^2$ such that the data can be fit to $y = a + bx$. In fact the problem is to minimise the discrepancies between the measured values and the

corresponding calculated values: $\Delta y_i = y_i - a - bx$ [97]. The total error of each data point is a combination of fluctuations and instrumental errors that are not equal for every data point, even within the one time set. Therefore each term in the sum of χ^2 is weighted by the deviation at that point before summing. Employing the solutions to this minimisation problem [97], it is only $T \pm \Delta T = \frac{m}{k_B}(b \pm \Delta b) = \frac{m}{k_B}(b \pm 2/3\sigma_b)$ that we are interested in finding.

2.5.2 Metastable detection by e^- measurement

When the internal energy E^* of a metastable atom exceeds the work function Φ of the surface upon which it alights an electron may be ejected. The electron emission coefficient γ_e is defined as the average number of electrons emitted per incident metastable atom. The value of γ_e is dependent on the excitation energy and the nature of the detector surface.

ELECTRON EMISSION FROM SURFACES

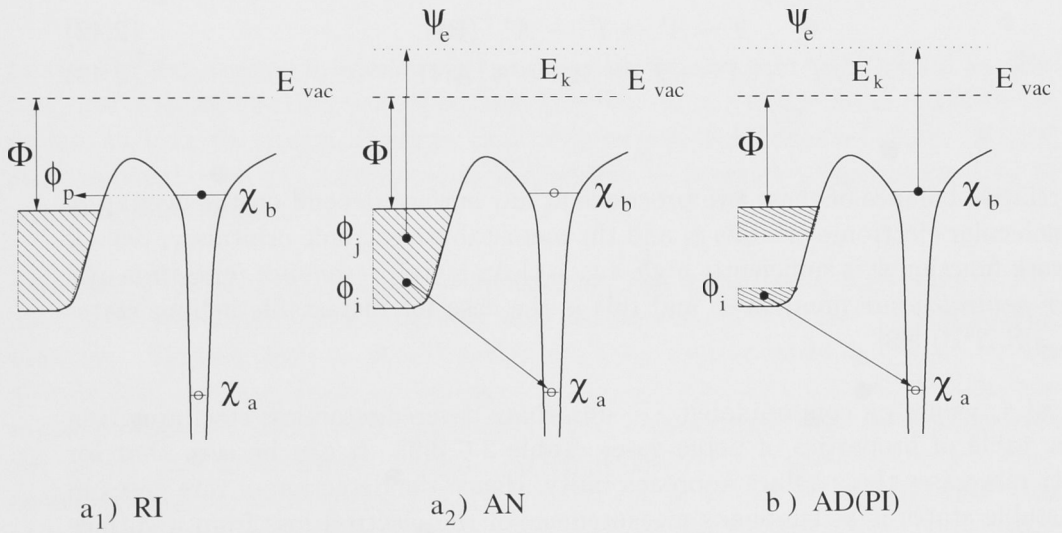

Figure 2.8: Mechanisms for electron emission from surfaces, shown in the diagrams of potential (vertical axis) for an atom with an excited electron state χ a distance (horizontal axis) from a surface with a work function Φ: resonance ionisation (RI) followed by Auger neutralisation (AN); and Auger De-excitation (AD) also known as Penning ionisation (PI). Diagrams not to scale.

There are two main processes by which rare gas metastable atoms can de-excite and an electron is ejected from a surface in the collision of a metastable atom (A^*),

illustrated in Fig. 2.8 [98, 99].

In 1927 Penning suggested the ionisation process due to collisions between metastable and gaseous target atoms (T):

$$T + A^* \rightarrow T^+ + A + e^- \quad \text{(PI)}. \tag{2.41}$$

At a solid surface this is alternatively called *Auger De-excitation* (AD).

Near a Fermi surface with a high work function a two stage process can occur. First an excited atomic electron tunnels χ_b tunnels into a vacant level (ϕ_p) above the Fermi surface creating an ion close to the surface (*resonance ionisation* RI, Fig. 2.8a_1). Then this ion neutralises by an Auger process (*Auger neutralisation* AN, Fig. 2.8a_2):

$$T + A^* \rightarrow T^- + A^+ \quad \text{(RI)}, \tag{2.42}$$

$$T^- + A^+ \rightarrow T^+ + A + e^- \quad \text{(AN)}. \tag{2.43}$$

The relative balance of these two processes at any surface depend on the overlap of the molecular electronic orbitals ϕ_i and the metastable electronic orbitals χ_i [98]. If the work function Φ is sufficiently high, e.g. a clean metal, *resonance ionisation* and *Auger neutralisation* dominates, and this is the case for metastable helium states (2^3S, 2^1S, 2^3P) [99].

Typical γ_e values on contaminated, i.e. adsorbate-covered, stainless steel are given in the table of properties of noble gases, Table 2.6 [99]. It can be seen that for lighter rare gases these values approach unity. Hence the detection of rare gases in metastable states is as simple as measurement of the electron loss from a surface upon which the metastable beam is incident. Then the techniques for detection of this electron fall into two regimes of low and high atom flux measurement. The boundary between these regimes lies approximately at the limit of current detection of a picoammeter, or saturation of a single electron detector.

$$10^{-12}/1.6 \times 10^{-19} = 10^6 - 10^7 \text{ Hz}$$

Rare Gas	State	E^* (eV)	E_{IP} (eV)	γ^a
He	$^3S_1$	19.8	4.8	95%
	$^1S_0$	20.6	4.0	
Ne	$^3P_2$	16.6	4.9	91%
	$^3P_0$	16.7	4.9	
Ar	$^3P_2$	11.5	4.2	97%
	$^3P_0$	11.7	4.0	
Kr	$^3P_2$	9.9	4.1	1%
	$^3P_0$	10.5	3.4	
Xe	$^3P_2$	8.3	3.8	2%
	$^3P_0$	9.4	2.7	

Table 2.6: The excitation, ionisation and emissivities of metastable states of Rare Gases [99].

[a]Electron emission co-efficients for stainless steel.

Low flux regime - atom counting

In the low flux regime measurements proceed via measurement and signal amplification of a single electron corresponding to detection of a single atom. Particle detectors such as electron multipliers, channeltrons and multi-channel plates (MCPs) are combined with pre-amplifiers and amplifiers to produce a signal that can be analyzed and counted.

The first stage of signal amplification is shown for the electron multiplier in Figure 2.9. The first contact of a particle with the front surface/dynode, ejects a single electron. This electron is accelerated toward the second surface/dynode by the electric field resulting from the difference in electric potential ΔV between the two surfaces. Upon colliding with this second surface several electrons are ejected from the surface due to the kinetic energy acquired by the first. These in turn are accelerated toward the third surface/dynode and so on, in a cascade or 'avalanche' that accumulates as a detectable charge Q deposited on the final anode. The principle in channeltrons and MCPs is the same, although there the cascade occurs within a continuous cylindrical surface with a varying potential along a resistive surface produced by a potential difference along its length.

Several factors go into the signal gain achieved by these detectors [100, 101]. The size of the final charge Q is dependent positively and negatively on the electrical properties of the surface/dynode. On the one hand the work function is required to be some fraction of the accelerating potential ΔV so that each colliding electron generates many more free electrons, typically $\times 4$ with dynode materials like beryllium copper. A typical average curve for emission of secondary electrons from an

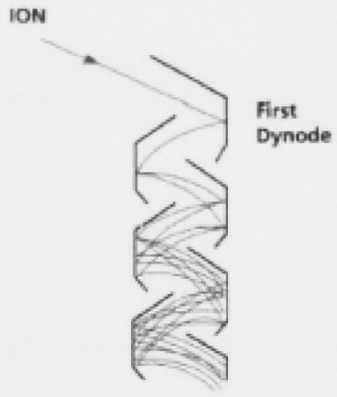

Figure 2.9: Electron cascade in a discrete dynode electron multiplier. Source [101].

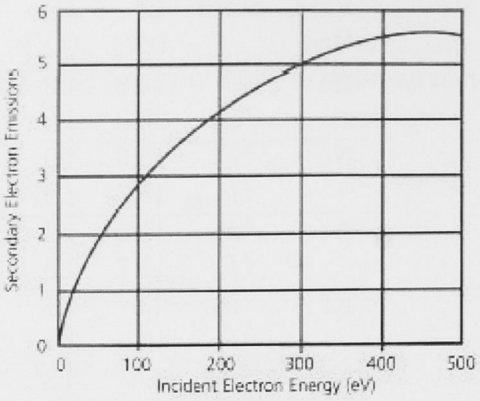

Figure 2.10: Average emission of secondary electrons for incident electron energy for a ETP electron multiplier. Source [101].

incident surface for the ETP electron multipliers used in this experiment is given in Figure 2.10 [101]. On the other hand the surface needs to be resistive to electric breakdown when subject to high potential differences. In the case of channeltrons and MCPs with continuous surfaces the total potential difference $V_{total} = N \times \Delta V$ must be maintained from one end of the tube to the other. These surfaces are commonly metallic impregnated glasses such as lead silicate.

Typically, then, there is a turn-on or threshold voltage where the cascade within the detector can be sustained. Examining Fig. 2.10 clearly no cascade can occur below $\Delta V = 25$ volts and at least 50 V is required for an 'avalanche'. With increasing potential the number of electrons and hence total charge Q increases monotonically, but eventually both the stimulation of secondary electrons and the efficiency of the avalanche begin to saturate. First the number of electrons in a cylinder of a given radius and height in the dynode surface that can be disturbed and ejected by the passage of the high energy electron is limited. Then the efficient focusing of the cascade so that electrons are not lost from the avalanche depends critically on the geometry of the dynode surfaces. The final effect is a practical limit on the signal gain of each individual stage, which is approximately linear over a limited range (say $\Delta V = 100 - 350$ V) [100].

The total gain is then a function of both the accelerating potential ΔV and the number of accelerating stages:

$$G \propto \Delta V_{total}^{n} \tag{2.44}$$

where n is of the order of the number of stages less two, typically $n = [7, 9]$ [100]. Dependence to such a high order on the applied voltage make the use of a stabilised power supply essential to consistent results, since the error in gain is

$$\delta G/G = n\delta\Delta V/\Delta V = n\delta V/V. \tag{2.45}$$

Hence with $n \sim 8$ a 1% variation in the HV supply is an 8% variation in gain, implying a requirement for ultra-stable high voltage power supplies.

The loss of electrons from the dynode depletes the surface for a period until the electrons can be replaced from the HV potential source. This dead-time limits the rate at which the electron multiplier can detect incident particles and reduces the effective measurement of individual particles at very high count rates [100]. The typical recovery time of the ETP electron multipliers is specified < 30 ns, so that at a 10 MHz input count rate there is only a 66% probability of detecting two subsequent atoms and the measured count rate is significantly depleted [100, 101]. At 20 MHz input count rate the detector is dead 50% of the time and above that the measured count rate will actually appear to decrease. The practical limit on counting individual atoms is limited to 1-10 MHz.

This is the upper limit of single atom detection in the low flux regime. However, as was noted above, this range overlaps with the lowest range of current detection in the high flux regime.

High flux regime - current measurement

Since the electron emissivity of stainless steel (Table 3.2) is near unity, measurement of high flux beams of metastable rare gases is very straight-forward. The $\geq 10^7$ electrons ejected from the metallic surface can be drawn away from the detecting surface by moderate potentials, a few tens of volts, on a second conductor, even just a wire. Then the direct current of electrons flowing into the detector to replace those can be measured with a picoammeter, and the measured current converted simply into atom flux.

At such low ranges (picoampere) the accuracy of current measurements are subject to large random fluctuations due to sources of all kinds. These including random fluctuations affecting the beam but also predominantly RF pick-up. This may occur inside the vacuum chamber due to other in vacuo electrical sources, such as the motor driving the chopper wheel in time-of-flight measurements (Sec 2.1.) It may also occur outside the vacuum chamber due to small faults in coaxial cable shielding or loose connections.

However typically direct current measurement of this sort are usually applied to beams several orders of magnitude larger providing nano- and milliampere currents. In these cases the random fluctuations of current measurements are reduced to fractions of to a few percent.

2.6 Conclusion

This Chapter has reviewed the basic principles and practices that underpin the development and study of the compact MOT loading He* beamline and LVIS in this thesis in the following chapters:

- The theory and practices for the state preparation and analysis of metastable atoms beams, including collimation, beam velocity, optical manipulation and detection, occur and recur throughout this thesis.
- The concept *atom beam brightening*, and the atom optical methods for achieving this, is essential to this thesis. In this context the theory and application of light-atom interactions for consideration in this thesis are reviewed.
- The application of these interactions in standard atom optical techniques for the production of a low velocity, high flux He* beam is considered through the example of the the ANU 'bright beam machine' as an example. Producing a flux of 10^9 atoms/s at 100 m/s, this existing He* beamline is a point of reference for the current beamline, especially as employed to load a large (10^9 atoms) magneto-optical trap.
- The application of optical methods of detection of He* have improved significantly with the development of IR sensitive photodiodes and charge coupled devices, leading to greater accuracy and ease of use and optimisation by these ensemble methods.
- The great advantage of neutral metastable states is single-particle detection by based on detection electronic methods. Ultimately these provide a detection range considerably greater than optical detection, over twelve orders of magnitude or more.

CHAPTER 3

A simple high flux He* source

The starting point of the compact He* beamline is a source of metastable helium atoms. Many source designs have been employed over 80 years including that developed in Ref [93] at ANU. The interest in developing a new source design is driven by the requirements of a compact beamline for a) a high flux, high brightness source, b) producing an atom beam of the lowest possible velocity. A compact MOT loading beamline with the lightest of all rare gas species requires the lowest possible initial velocity if sufficient slowing is to occur in the desired length to maximize the capture efficiency of the trap. This final velocity range, typically < 100 m/s, is still far below the average atom beam flow of liquid nitrogen cooled sources that for helium is still approximately one kilometre per second.

The problem is that these criteria are nearly opposed. In the basic model of atoms effusing from a source (Eq 3.2), flux scales with mean velocity. Non-effusive, 'supersonic' sources such as the ANU source experience higher 'flow' velocities [93]. Conversely source conditions capable of effusive flow are likely to have a reduced and unstable rate of excitation. The new source is required to generate as many metastable atoms as possible, in such a way that the average velocity of the resultant beam is as low as possible while still maintaining the beam density.

The new design and performance of a liquid helium cooled, grounded hollow cathode source is described in Section 3.3. This source generates fluxes $\sim 10^{14}$ atoms/sr/s, comparable with other metastable helium sources used in atom optics, with considerably lower average velocities ($450 - 700$ m/s) than liquid-N_2 cooled sources.

The design, construction and operation of this new source requires an understanding first of both source characteristics and cryogenic systems. The properties of sources in general, and of metastable rare gas atoms in particular, that provide the background for the choices made in the design of this new source are reviewed in Sec 3.1. This is followed in Sec 3.2 with an overview of cryogenic cooling of sources used to reduce the operating temperature of the new source to 4 kelvin.

3.1 Metastable atom sources

A metastable atom source performs two functions: first, it is a source of atoms, and second, some fraction of those atoms are excited into a metastable state. This section considers first the well established basic characteristics of atomic and molecular sources. The second part reviews the options for production of metastable states, and the characteristics that favour a hollow cathode gas discharge design for the new source.

3.1.1 Effusion of atoms from a reservoir

The theoretical and practical development of thermal beam sources has been well established by pioneers of atomic and molecular physics such as Knudsen and Ramsey [70] and has now been integrated into summary monographs that include emerging techniques of the late twentieth century including light interactions with neutral atoms [67].

The basic component of an atomic source is a vessel containing the element of study in gas phase, with an aperture, or nozzle, in one face through which the gas will 'leak'. The nozzle is typically a small circular aperture or a narrow slit. In either case the nozzle width w is customarily used to refer to the smallest dimension. It is essential to Knudsen's cosine law of molecular effusion that the motion is molecular effusive rather than hydrodynamic [70]. First, any molecule that strikes the aperture passes through it. Second, the spatial and velocity distributions within the vessel (which contribute to the mean velocity $\bar{v}$) are unaffected by the loss of molecules by effusion. This second condition requires that the slit width is much smaller than the mean collision free path inside the source: $w \ll \lambda_{Ms}$. Then the element of molecular flow or *flux*, $d\Phi$, from a source aperture into each segment of solid area $d\Theta$ is [70]:

$$d\Phi = (\frac{d\Theta}{4\pi}) n\bar{v} \cos\theta A_s. \tag{3.1}$$

Here n is number density of the gas, $\bar{v}$ the mean molecular velocity in the source, and θ is measured from the normal to the aperture area A_s. Integrated over the 2π solid angle in the forward direction the total flux is

$$\Phi = \frac{1}{4} n\bar{v} A_s. \tag{3.2}$$

The resultant flux is dependent on the gas pressure, via n, and temperature, via $\bar{v}$, and the nozzle shape. In practice the first assumption above, to do with the thickness of the slit, cannot be physically realized in all but rare circumstances.

Equally the assumption of effusive flow depends on the thermodynamic state of the source gas, and if that cannot be satisfied the nozzle creates a partial hydrodynamic (supersonic) flow. The consequences of each are considered in the following Section.

Nozzle design

If the thin walled aperture assumed in the derivation of Eq 3.2 is replaced by a channel aperture of considerable length, the total flux Φ can be expected to be reduced by the loss of molecules which strike the channel wall during their passage [70]. In particular the cosine law of Eq 3.1 will be altered because while the total amount of gas which emerges from the source will be reduced, the component with a velocity in the direction of the channel will be undiminished.

This reduction is expressed in terms of a pre-factor $\frac{1}{\kappa}$ introduced to Equation 3.2. In general this pre-factor is calculated by the integral along the length of the channel:

$$\frac{1}{\kappa} = \frac{16}{3} / \left(A_s \int_0^l \frac{o_p}{A^2} dl \right) \tag{3.3}$$

where A is the cross-sectional area orthogonal to the nozzle axis, and o_p is the length of its perimeter [70]. If cross-section is constant then

$$\frac{1}{\kappa} \Rightarrow \frac{16}{3} \frac{A_s}{o_p l} \tag{3.4}$$

Three cases are of particular note:

- if the length of the channel is reduced to zero then $\frac{1}{\kappa} = 1$;
- for a long cylindrical tube, where the length is greater than the radius $l \gg r$, $\frac{1}{\kappa} = \frac{8}{3}\frac{r}{l}$
- for a long rectangular slit, with a slit height $h \gg l$ and length $l \gg w$, $\frac{1}{\kappa} = \frac{w}{l} \ln \frac{l}{w}$

From the flux Eq 3.2 the intensity measured by a detector with a surface area A_d at a distance l_d can be calculated [70]:

$$I = \frac{1}{4\pi} \frac{A_d}{l_d^2} n \bar{v} A_s = 1.118 \times 10^{22} \frac{p' A_s A_d}{l_d^2 \sqrt{mT}}. \tag{3.5}$$

The last part of this equation gives the intensity in terms of the thermodynamic quantities of the source gas, pressure p' and temperature T. The numerical factor is for pressure in units of torr, temperature in Kelvin, and lengths in centimeters.

Velocity distribution of a beam

The velocity distribution within a thermal source follows a classical Maxwell distribution of a gas. However the probability of an atom emerging from the source is proportional to the atomic velocity, as is apparent from the velocity dependence of the Equation 3.2 for flux. Hence the beam intensity for atoms between velocities v and $v + dv$ is [70, 72]

$$I(v) = \frac{2I_0}{v_{th}^4} v^3 \exp(-v^2/v_{th}^2) \tag{3.6}$$

where v_{th} is the thermal velocity width $\sqrt{2k_BT/m}$. Normalized this is equivalent to the probability for an effusive (Mach number M$\ll 0.1$) beam as shown in Fig 3.1.

Supersonic factors

Where the condition for effusive flow through the nozzle ($w \leq \lambda_{Ms}$) is not satisfied, the collisions of particles within the nozzle become significant [71]. Fundamentally the walls of the nozzle restrain motion in the tangential plane. Then rethermalising collisions redistribute kinetic energy from these dimensions to the longitudinal axis. The net effect is the narrowing of the thermal velocity widths in three dimensions, while the total axial or 'flow' velocity increases. The spatial distribution affected by directionality thus becomes more strongly peaked [71]. Properties such as the flow velocity $u(x)$ and thermal velocity ($v_{th}(x) \neq u(x)$) become a function of the axial distance x from the source [71].

$$P(v) \propto v^3 \exp\left[-\frac{m(v-u(x))^2}{2RT(x)}\right] = v^3 \exp\left[-\frac{m(v-u(x))^2}{v_{th}(x)^2}\right]. \tag{3.7}$$

The conservation of enthalpy is used to examine supersonic effect in detail. In the case of adiabatic, isentropic expansion:

$$H(T(x)) + \frac{1}{2}mu(x)^2 = H(T_{source}). \tag{3.8}$$

Quantity	Value
C_P	$\frac{5}{2}R$
$\gamma = C_p/C_V$	$5/3$

Table 3.1: Thermal parameters for an ideal monatomic gas

Here $H(T(x))$ is the molar enthalpy of the gas at the position x. For an ideal gas $H = C_P T$. In turn the ratio $T(x)/T_0 = W^{-1}$ can be related to the Mach number $M(x)$ by

$$W \equiv 1 + \frac{\gamma - 1}{2} M^2(x). \tag{3.9}$$

In principle the Mach number increases very rapidly downstream. In reality the expansion 'freezes out' and $M(x) \to M$ at some point where the average number of collisions drops below the requirement for rethermalisation [71]. The theory is scaled in units of w, the source diameter, and in practice the beam characteristics are stable just a short distance (several w) from the source. Hence 'downstream' dependence is equivalently and more usefully expressed as Mach number dependence: $u(x) \to u(M); v_{th}(x) \to v_{th}(M); T(x) \to T(M)$.

The Mach number dependence of the beam temperature $T(M)$ and the flow velocity $u(M)$ can be calculated using equations 3.9 and 3.8. The beam temperature $T(M)$, related to the velocity width, very rapidly decreases with even low small (1 - 5) Mach numbers, while the average flow very rapidly approaches a limit given by

$$u_{max} = \sqrt{\frac{H(T_0)}{m}}. \tag{3.10}$$

Figure 3.1 illustrates the supersonic effect on the longitudinal velocity distribution for very low (effusive), low and high Mach numbers. These are obtained by calculating $T(M)$ and $u(M)$ from Equations 3.9 and 3.8 respectively, then substituting these into the velocity distribution generalized from Eq 3.7 by Morse [71]. The probability distributions have been normalised to unit area. The transitions with increasing Mach number occur in two phases. As the flow moves from effusive (indistinguishable from $M \sim 0.001$) to a Mach number of unity, the flow velocity shifts to a higher average value, approaching the limiting value u_{max}. For still higher Mach numbers (M$\geq$ 1) the center of the distribution approaches a limiting value and the main effect of further increasing Mach number is velocity bunching and reduction in the thermal velocity width v_{th}.

The original aim for the LHe cooled GHC was for a source producing a sizable

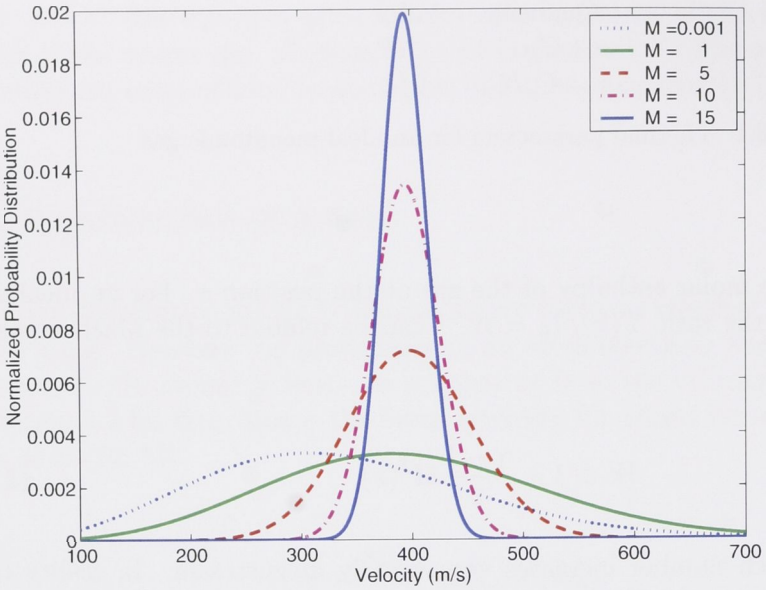

Figure 3.1: The longitudinal velocity distributions for a 5 K beam with Mach number varying from effusive (indistinguishable from $M \sim 0.001$) to high supersonic (M=15). The distributions have been normalised to unit area.

fraction of atom flux in a velocity range below the (enhanced[†]) capture velocity of a MOT, obviating the requirement for further slowing of the atom beam. Then it is immediately apparent from Fig 3.1 that it is desirable to operate the source closer to the effusive regime rather than the supersonic regime, since the wider probability distribution reaches these lower velocities.

Later in Section 4.1.2 we review the reasons why this represents sub-optimal application of the GHC source in a compact MOT loading beamline, and matching the source with a optimised Zeeman represents a better technological solution. In this case the operation of the source at higher pressures resulting in an increased Mach number does not *a priori* decrease the number of atoms capturable by the slower.

3.1.2 Production of excited states of atoms

Many designs for sources of atoms and molecules in metastable states have been developed in the past 80 years, but in general they can be classed in one of five categories according to the process of excitation [64]:

[†]Some amount of Zeeman slowing might be achieved using the distant magnetic field of the MOT and an additional slowing light field, as in Ref [34]

Rare Gas	Mass (amu)	State	τ (s)	λ (nm)	E^* (eV)	T_{boil} (K)	$\bar{v}_{\sim T_{boil}}$ (m/s)	Source Type[a]	Flux s^{-1}
He	4	$^3S_1$	7870	1083	19.8	4.2	390	(1)(2)	10^{13-15}
		$^1S_0$	0.0196		20.6			(3)	10^{11-13}[b]
Ne	20.1	$^3P_2$	14.7[c]	640.2	16.6	21.1	250	(1)(2)	10^{13-15}
		$^3P_0$	430		16.7			(3)	10^{11-13}[d]
Ar	49.9	$^3P_2$	55.9	811.5	11.5	87.5	310	(1)(2)	10^{13-15}
		$^3P_0$	44.9		11.7			(3)	10^{11-13}[e]
Kr	83.8	$^3P_2$	85.1	700-	9.9	120.8	250	(1)(2)	10^{13-15}
		$^3P_0$	0.488	900	10.5				
Xe	131	$^3P_2$	149.5	882	8.3	165.1	220	(2)	10^{13-15}
		$^3P_0$	0.078		9.4				

Table 3.2: Summary of atomic, optical and thermal properties of Metastable States of Rare Gases and Sources [12, 64, 99].

[a]Electron bombardment (1), discharge (2), charge transfer (3), separated by range.
[b]Brightness $sr^{-1}s^{-1}$
[c]Recently measured in 2002 [102] the general references [12, 99] quote 24.4 s based on older theoretical predictions [103].
[d]Brightness $sr^{-1}s^{-1}$
[e]Brightness $sr^{-1}s^{-1}$

1. electron-beam bombardment;
2. electron discharge;
3. charge transfer;
4. optical pumping;
5. thermal collision.

Table 3.2 summarises the relevant properties of the rare gas metastable states. This includes the electronic, optical and thermal characteristics of dominant metastable states and the type and flux of common source designs. Clearly for rare gases, where the metastable state energy E^* is of order tens of electron-volts, the last two excitation processes (4, 5) are unsuitable where thermal energies are of order tenths of an electron-volt, and short-wavelength UV photon sources are impractical.

In charge transfer sources (3) a fast beam of ions is neutralized in a target cell. This process has the advantage that the background gas load can be minimized because the ground to excited state ratio is closer to unity [64]. Hence they are particularly popular for experiments with rare gases where this load is a serious problem. A fast ion beam is partially neutralized in a target cell producing ground and excited state atoms. The efficiency of this process is mostly dependent on 1) minimizing the energy defect ΔE between the the target ground state and the projectile metastable state, and 2) matching the incident ion velocity with the target electron

velocity so that the electron is not excessively accelerated. However the velocities required demand high voltage ion beam accelerators and produce a fast beam of metastable atoms and ground state atoms, the latter adding to the background in the experimental region.

Electron-beam bombardment (1) and discharge sources (2) are similar in that the metastable state is excited by collisions with energetic electrons. A flux of electrons with tens or hundreds of electron-volt kinetic energies is easily created in a discharge between an anode and cathode. However the cross-sections for metastable excitations are typically very small ($\leq 10^{-17} cm^2$) which means these classes suffer the same limits of very large electron currents and very low ($10^{-4} - 10^{-5}$) production rates [64]. A significant issue is the spreading of the velocity distribution of the effusing atomic beam by the momentum transfer from electron collisions. This is especially important for light elements, such as helium, and at very low source temperatures or initial velocity distributions.

In e^- beam bombardment sources (1) a well-directed e^- beam collides with the atomic beam. The primary design parameters of the source are the electron beam energy and current, and the overlap with the atomic beam. Given the physical rates noted above, very high current densities and a high degree of precision in overlapping the beams is essential to maximize the efficiency of a source. Often this can be achieved by a combination of electrodes for beam focusing and magnetic fields for confinement. However the relative excitation processes of each metastable state ($^3S_1$, $^1S_0$) are energy-dependent, and the efficiency of excitation is maximal just above threshold, dropping more rapidly for triplet than singlet states. For helium this means that nearly all the metastable atoms are 2^1S states by 100V electron energy [64].

Electron discharge sources (2) are generally the simplest to build and operate, so that a wide range of designs exist. The velocity distribution is broader in general than those of bombardment sources, and sputter erosion of the discharge anode is an operational limiting factor. Cryogenic supersonic sources have reduced the average beam velocity from the very high speeds (2 km/s for helium) at room temperature, and these are the most popular sources amongst atom optics experiments. For reasons both of the ease of manufacture and experience with the design, and the absence of any overriding benefit from any other of these five basic options, the new He* source design has been chosen to be an electron discharge source.

Gas discharge sources

Conventional metastable rare gas discharge sources typically employ a sharp needle cathode inside a gas reservoir, and an exit nozzle to allow gas expansion into a vacuum chamber [104, 105, 106]. Typically these operate in a range of gas pressures and

discharge voltages resulting in a "glow discharge" as exmplified by a fluorescent light tube. In the following sections we review the properties of gas glow discharges and hollow cathodes that guide the new design of the hollow cathode source discussed in depth in Section 3.3.

Glow Discharges

A contained fluorescent gas discharge is a basis for understanding the operation of a gas discharge source. A schematic of a normal gas discharge is shown in Fig 3.2 together with plots of the electric field strength and potential as a function of position [107]. The fluorescent glow is sustained between an anode and cathode in a volume of purified gas. In a discharge the current densities are of order $10^{-5} - 10^{-2} A/cm^2$, with a roughly constant sustaining voltage [107]. Since the current density is constant at the cathode the discharge current scales with the cathode area involved in the discharge, until ultimately the cathode is completely covered, at which point the discharge enters the phase of *abnormal glow.*

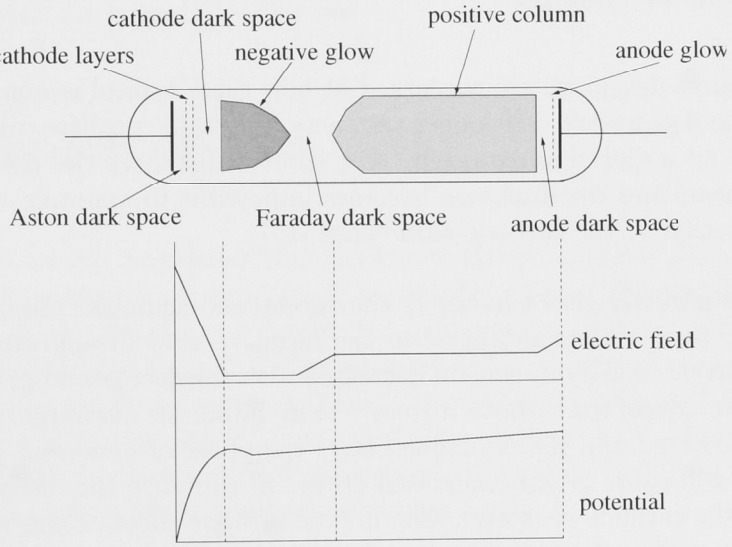

Figure 3.2: A schematic of the components of a normal discharge glow, with plots of the electric field and potential, between a cathode and anode in a sealed gas vessel. The major parts are dark space and negative glow next to the cathode and the positive column next to the anode, separated by the Faraday dark space.

The typical regions and basic discharge properties are illustrated in Fig 3.2. The three major regions are the *cathode dark space, negative glow* and *positive glow* [107]. Electrons emitted from the cathode are accelerated toward the anode until slowed by elastic collisions. In the Aston dark space the electrons have insufficient energy

to excite atoms in collisions. When the electrons do have sufficient energy weak glow lines occur with the lowest energy (red) spectral lines closest to the cathode. Ionization of the gas increases with distance from the cathode, reducing the electric field. In a lower field both excitation collisions become more efficient and the electronic motion becomes more random. In the resulting *negative glow* region excitations with the highest energy (blue spectral lines) occur near the cathode edge, fading through the *relatively* dark 'Faraday dark space'. Electron, ions and photons are lost to the walls.

Finally the electrons crossing the Faraday dark space re-acquire enough energy to ionize gas again, with low energy spectral lines appearing first along a diffuse border because the electrons arrive with a broad energy distribution. In the *positive column*, which takes up most of the remaining space, the density of ions is about equal with that of electrons $\sim e^{-}$ $10^{10} - 10^{12}/cm^3$, and the resulting fields are quite weak, hence this plasma is quite stable and self-sustaining [107]. The electrons drift with a small velocity to the anode.

Hollow cathode gas discharges

For the purpose of source design we are concerned at how these typical regions are modified by pressure and geometry. For longer distances, the stable positive column length increases, but no major changes occur. For shorter distances the positive column length disappears and the discharge becomes impossible to maintain when the anode reaches the edge of the cathode dark space [107].

At lower pressure, the negative glow extends to the anode, and again the discharge becomes substantially harder to maintain when the negative glow disappears. In addition, while the current density in general decreases with the decrease in ground state density, the active area of the cathode increases to maintain the discharge, until the entire cathode is covered and the discharge enters the phase of *abnormal glow*, where the sustaining voltage is greatly increased [107]. In this case the discharge can be influenced by the cathode geometry. The hollow cathode effect occurs when two plane cathodes are sufficiently close together for the negative glows to interact. Then the ions, electrons, metastable atoms and photons leaving the sides of the plasma are not lost from the system. A hollow cathode can increase the current density by two or three orders of magnitude, such that for a particular current the emitting area can be greatly reduced. It follows that a higher current can be sustained in a lower density gas with a lower electric potential, thereby reducing heating by electron momentum transfer of helium, for example [107].

Hollow cathode discharges have found application as stable sources for wavelength standards in atomic spectroscopy (e.g. [108]), ion plasmas (e.g. [109]) and electron beams (e.g. [110]), but not for neutral, metastable atomic beams.

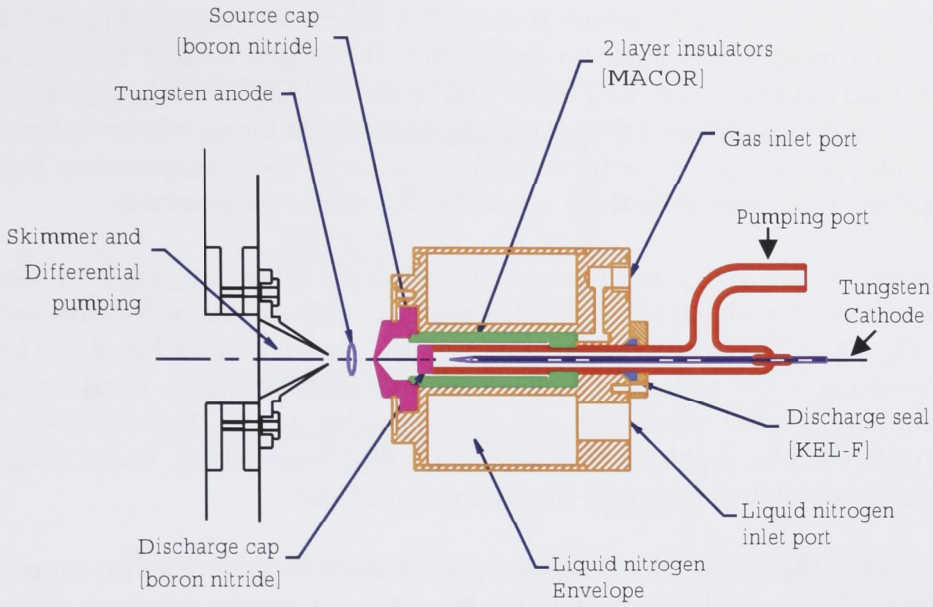

Figure 3.3: The ANU bright beam machine uses this liquid nitrogen cooled electron discharge He* source [66]

3.2 Cryogenic discharge sources

In Section 3.1.2 it was shown that the gas discharge source is probably the simplest method to produce large numbers of metastable atoms. This has been the standard approach in the Atomic and Molecular Laboratories at ANU, following the introduction by Shimizu *et al* of a design for a cryogenic, supersonic gas discharge sources [105]. Liquid-nitrogen cooling of the source reduces the average He* beam velocities to about a kilometre per second. As shown in Sect. 3.1.2, supersonic cooling of the longitudinal velocity spread or thermal width from these sources increases the velocity resolution of experiments using this beam.

At ANU Lu *et al* [93] developed a liquid-nitrogen cooled metastable helium source which yields high fluxes (up to 10^{15} atoms/sr/s). The major features of this design are shown in Fig 3.3. A stainless steel can holds an envelope of liquid nitrogen around the gas flow volume. The electric discharge is struck between a ring anode external to the nozzle and a tungsten needle cathode supported in a glass tube. A $\sim$1000V discharge to the source body is prevented by Macor cylinder insulators and the boron nitride nozzle cap.

This source is a reliable and efficient source of He* atoms for experiments like atom lithography and electron scattering, but only after significant beam slowing and brightening (Sec 2.4) can it be used to efficiently load a magneto-optical trap.

The major constraint on liquid *helium* cooling of a source like that in Figure 3.3 is the additional insulation required to ensure that the helium coolant flows *as a liquid* rather than a cold gas. The LN_2 source also operates at significantly higher gas pressures by one to two orders of magnitude than is suitable for an effusive source. Needle cathodes perform poorly at these lower pressures at room temperature, and may be expected to be very difficult to operate at cryogenic temperatures.

A liquid helium-cooled source has been developed in the laboratory of Peter van der Straten at the Debye Institute, Utrecht University [111]. Its major features can be seen in Fig 3.4 to be essentially the same as a LN_2 source such as Fig 3.3. The principle exception is the replacement of the insulating boron nitride nozzle with an aluminium nozzle plate which also acts as a grounded anode. This introduces one of the most complex problems of cryogenic gas discharge sources, which is the design of the nozzle plate, principally the choice of material.

On the one hand, thermal conduction is greatest in metallic materials like copper or aluminium. This is significant since in practice very few nozzles are short channels (see Sec 3.1.1), and interior surface of the nozzle is the last with which the gas particles have any thermal contact so that the nozzle must be at the lowest temperature.

On the other hand, if the nozzle is an electric conductor, the discharge will most likely strike to inner circumference of the nozzle, and very few atoms will be excited into the metastable state in or after their passage through the nozzle. This reduces the metastable flux compared to a source with an external anode, both because the overlap of electrons with atoms on a path through the nozzle is smaller, and because of the de-excitation of metastable states through atomic collisions during their passage through the nozzle.

Furthermore a metallic nozzle is subject to sputtering loss of its material and deteriorates over time, requiring regular maintenance.

The results with the Utrecht source testify to this problem [34]. Operated at drive pressure three orders of magnitude less than the typical LN_2 source, the average velocity of $\sim$ 300 m/s and FWHM $\sim$ 100 m/s corresponds to a beam temperature of 10-15 K. But the cost is in flux, which at 10^{12} atoms/sr/s is just enough to load a small ($\sim 10^6$ *atoms*) MOT.

We have created a new design for a discharge source that uses liquid *helium* cooling. We adapted a commercial LHe cryostat to cool a hollow cathode discharge source that supports a higher electron current at equivalent atom and current densities and lower electron temperatures. First we review cryogenic systems at liquid helium temperatures.

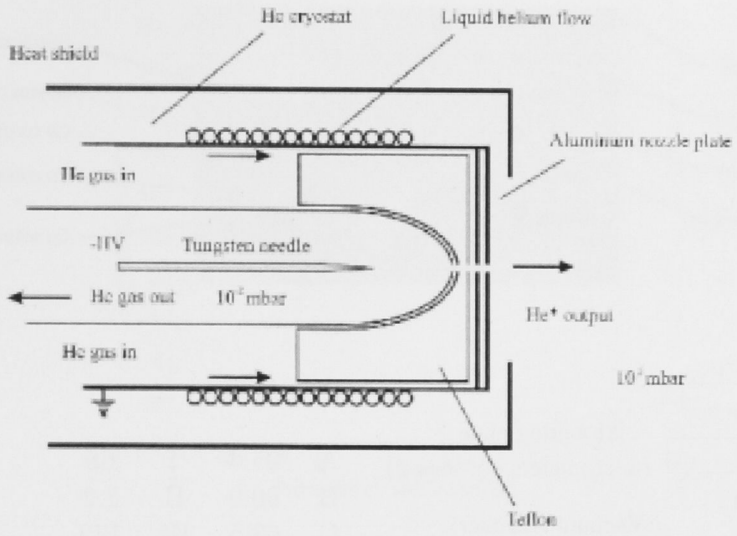

Figure 3.4: The Utrecht Source. Image from Reference [34]

3.2.1 Cryogenic system

This section discusses some elementary considerations when operating a cryogenic system with liquid helium, to achieve the optimum cooling performance. That optimum may be defined as operating as close as possible to the coolant (liquid helium) temperature before taking into account the effects of the discharge.

Liquid helium has a boiling point of 4.2 K and an expansion ratio from liquid to atmospheric pressure and temperature of 1:754, so it is potentially explosive. It is also difficult and expensive to manufacture, so it is important to use it both safely and efficiently. The Research School of Physical Sciences and Engineering has a helium liquefying plant so the exhaust helium gas is collected and recycled.

The cryostat

The source is mounted on a Janis Model continuous flow cryostat seen in Fig 3.5. The key features of the Janis cryostat to note are:

- the copper cold-finger;
- the heater coils just above the cold-finger that in conjunction with a temperature sensor and temperature controller permit the temperature to be set a fixed levels; and
- the copper mount for a cold-shield.

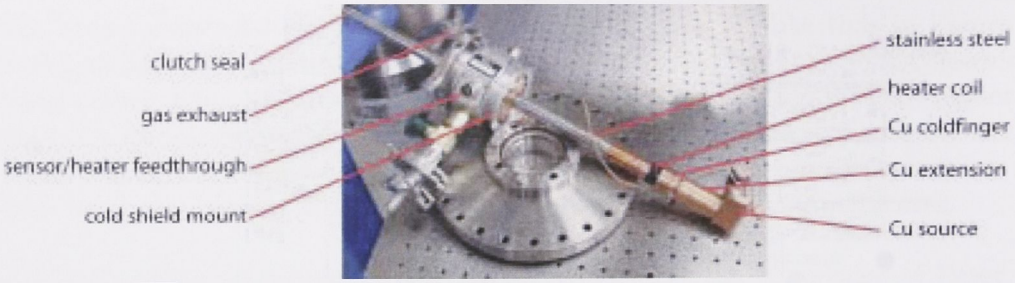

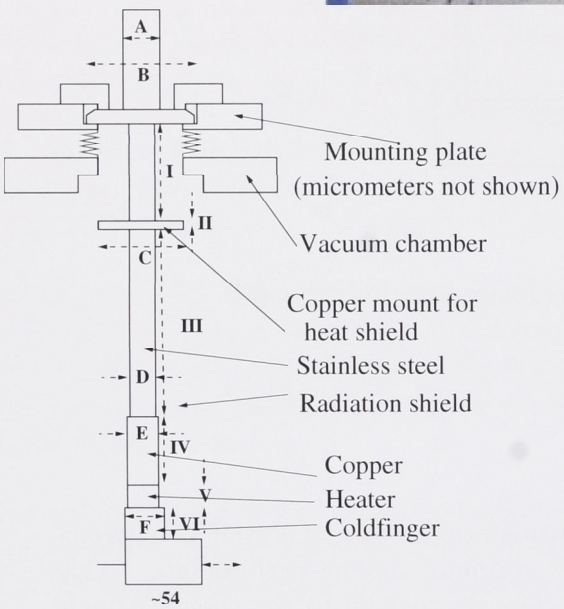

A	25.4	I	68
B	90.9	II	8.2
C	63.5	III	132
D	19.2	IV	47.5
E	21.4	V	15.5
F	28.6*	VI	21

Lengths and diameters in mm (* on flat; 31.8 OD)

Figure 3.5: The Janis Cryostat, with the source block attached via an extension column during testing. Components of the source can be seen on the table.

The temperature of the cold-finger (or any component) is measured using a silicon diode and LakeShore temperature controller with a precision of ± 0.05 K. The coolant (LN_2 or LHe) is transferred in a continuous flow from a dewar via a vacuum insulated transfer tube. The transfer tube is inserted at the top of the cryostat clamped with the seal clamp just visible at the top left hand of the Fig 3.5. The transfer tube extends all the way down to the cold-finger, where the liquid helium flows drop by drop through a 1 mm tube down the centre onto the copper block of the cold-finger. The rate is controlled by a screw needle valve in the transfer tube. The large volume of cold helium gas exhausting around the outside helps to insulate the liquid pipe. The rate of gas flow is measured by a gas flow meter in the helium return line, and since the expansion ratio is constant this is effectively a measure of liquid helium consumption.

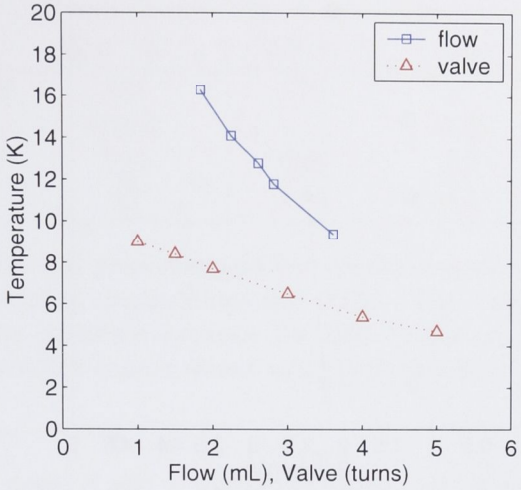

Figure 3.6: Cold-finger temperatures shown against: exhaust gas flow (□, litre (LHe) per minute) as a function of a heat load of 3.6 W; needle valve opening (△, turns) with a heat load of 1.2 W. Reading errors are smaller than the data symbols.

3.2.2 Performance of the cryogenic system

Efficient operation of the LHe cooled source requires some basic data on the performance of the cryostat, but particularly the expected rate of liquid helium consumption. The three variables controlling the cold-finger temperature are the opening of the screw needle valve, the volume of the LHe flow and the heat load applied to the cold-finger using the heater coils. The relationship between the screw valve and LHe flow is neither *a priori* linear nor constant between uses as it depends on the dewar head pressure. The gas flow meter is located in another laboratory, and the valve is the only 'calibrated' measure of the flow 'on-site'. In practice the valve and dewar head pressure will be optimised at those settings that achieve the lowest temperature with the least amount of liquid helium. Three experiments investigate the temperature dependence of each variable, the results of which are shown in Figures 3.6 and 3.7.

First the temperature of the cold-finger was measured in proportion to the consumption of liquid helium, measured by the flow rate of exhaust helium, for a constant heat load of 3.6 W (□, litre (LHe) per minute). Appropriately this is a straight line (within the errors in flow measurement), as it is effectively a measure of the latent heat of vaporization of helium. Note that at this power the minimum temperature was ~10 K even at maximum flow, indicating that this heat load is greater than that which can be dissipated to maintain the cold-finger at LHe temperature.

In the next experiment this heat load is set at 1.2 watt, a load that can be totally

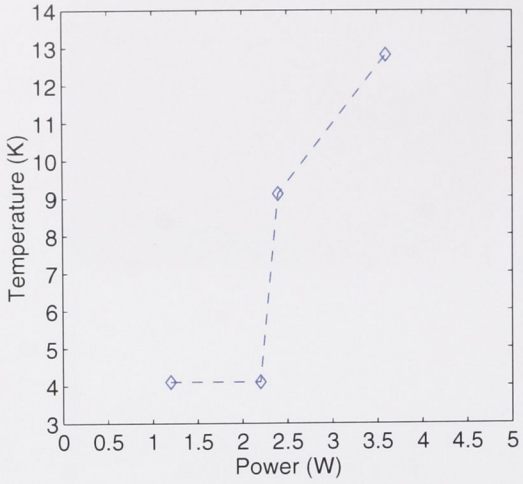

Figure 3.7: Cryostat temperature performance as a function of heat load (◇, watt, erros approximately the width of symbol), with maximum cooling as the needle valve is fully open.

dissipated by the liquid helium. The temperature is measured against the screw needle valve opening (△, number of turns of the screw valve), the control variable that can be observed in the laboratory during operation. The linearity of this data confirms that the LHe flow is proportional to the valve opening.

These experiments show that the temperature of the cold-finger can be controlled with the LHe flow and cooled as low as 4.2 K while subject to a substantial heat load. The final test is the load limit at which that minimum temperature can be reached. The result of this test, varying the applied heat load with the valve fully open, are showing in Fig 3.7.

With this understanding of control of the cooling rate, the system's limit of heat dissipation (◇, watt) is the final and most important test. To measure this the heater power was increased with the needle valve fully open. When the rate of heat dissipation exceeds the heat load the cold-finger temperature sits at the minimum 4.2 kelvin. However above a heat load of 2.2 W the temperature increases, indicating the load exceeds the cooling power. Hence the the cryostat can dissipate heat loads only up to 2.2 W, and maintain the cold-finger at minimum temperature.

Heat conduction

The base material for the source is a copper block attached to the cold-finger. Copper is chosen for its high rate of heat conduction, similarly for the cold-finger itself. Equally the parity of conduction rates between both materials avoids a bottleneck

Medium	Conductivity $Wm^{-1}K^{-1}$	Hardness /MN m^{-2}	Thickness[a] mm	ΔT K
polished Copper	401	879	0	~12
Apiezon N	0.001		0.05	~10
Aluminium foil	235	245	0.1	~9
Indium foil	82	8.83	0.5[b]	0.6

Table 3.3: The thermal properties and test results of cryogenic joining materials (supplier specifications and [112]). The temperature ΔT measures the difference between the LHe cooled copper cold finger and the attached copper source using each material.

[a]Estimates only.

[b]Indium's 'tackiness' makes it able to conform to surfaces also makes it difficult to manufacture into a very thin foil.

in the flow of heat away from the source.

What does reduce the heat flow is the connecting surface between the source block and the cold-finger. Although the source block is larger than the cold-finger, and hence maximizes the possible area for thermal contact with it, the actual contact area is much less because of the roughness of the two surfaces. At an atomic level the two surfaces actually come into contact only where small elevations strike each other, and thus the heat flow is reduced by orders of magnitude. Table 3.3 gives the results of measurements of the temperature difference (ΔT) between the cold-finger cooled to 4.2 K and an attached copper block. The problem of contact area is demonstrated by the ~12 K difference in temperature between two polished copper surfaces.

Heat conduction across a surface can be substantially improved by using a medium to fill the gaps at an atomic level. This is a familiar experience with the thermal paste used to connect electrical components, especially CPUs, with heat-sinks. At cryogenic temperatures properties other than heat conductivity of these mediums become important. If a paste or grease solidifies or crystallizes under these conditions then it is likely to be ineffective. Two materials recommended at cryogenic temperatures are indium foil and a specialty cryogenic grease, Apiezon N.

The properties of various medium materials are tabulated in Table 3.3, together with their effectiveness as measured here by the temperature difference ΔT between the source block and the cold-finger, compared to the mating of just the two polished copper surfaces.

Apiezon N grease is used in equilibrium applications, such as with a temperature sensor. The result with Apiezon N grease suggests it is not suited to conditions where there is substantial heat flow.

Emissivity	Radiation 300K to 77K	from 77K to 4.2K
Aluminium anodized	0.78	0.67
Aluminium-oxidized	0.5	
Aluminium-as found	0.12	
Aluminium mechanically polished	0.1	0.06
Aluminium electrically polished	0.075	0.036
Copper as found	0.12	0.06
Copper mechanically polished	0.06	0.023
Stainless Steel - as found	0.34	0.12
Stainless Steel - mechanically polished	0.12	0.03
Stainless Steel - electrically polished	0.1	0.065
Stainless Steel - as found with Al foil	0.056	0.011

Table 3.4: Emissivities of aluminium, copper and stainless steel, for various methods of surface finishing, as materials for a heat shield of the source held at 77 K [112].

To improve the conformity of the metallic foils to the contact surfaces they were heated while the block was tensioned, with softer materials (indium) being more responsive to such heating. These temperature difference results clearly demonstrate the importance of contact area over even thermal conductivity: even pressed between two polished copper surfaces, the disadvantage in hardness of the aluminium outweighed its advantage over indium in conductivity. At just < 1 K difference the copper block of the grounded hollow cathode source is effectively cooled to liquid helium temperature.

Heat radiation

At LHe cryogenic temperatures the radiation heat load on the copper source block from the surrounding environment has to be taken into consideration. This heat load from a hot object to a cold one can be calculated straightforwardly from the heat flow equation

$$Q = C_{SB}(T_h^4 - T_c^4)/f_V. \tag{3.11}$$

where C_{SB} is Stefan-Boltzmann constant 5.67×10^{-8} W/m^2/K^4. The 'view factor' f_V takes account of the possibility of transmission of thermal photons inherent in the geometry (as area A_i) and materials (as emissivity ϵ_i) of the hot (h) and cold (c) surfaces:

$$f_V = \frac{1}{\epsilon_h A_h} + \frac{1 - \epsilon_c}{\epsilon_c A_c}. \tag{3.12}$$

	R (m)	H (m)	SA (m^2)
Source Chamber	0.15	0.30	0.433
Heat Shield	0.038	0.15	0.0405
Source Block(a)	0.015	0.015	1.41×10^{-3}
Source Block(b)	0.03	0.05	7.09×10^{-3}

Table 3.5: Primary dimensions are given for the source vacuum chamber and heat shield, both cylinders, and the source block at 4.2 K comprised of the cylinder of the cold-finger (a) and the source block (b) L(R)×W(R)×H

			ΔT (K)	f_V (m^{-2})	Q (W)
Source Chamber	$\rightarrow$	Source Block	290	1.848×10^3	0.2292
Heat Shield	$\rightarrow$	Source Block	73	2.528×10^3	0.0008
Source Chamber	$\rightarrow$	Heat Shield	217	2.292×10^2	1.8397

Table 3.6: Various heat loads for a vacuum chamber with an 'as found' stainless steel surface at room temperature, an externally mechanically polished heat shield at 77 K, and an 'as found' copper block at 4.2 K.

The emissivities of copper, aluminium and stainless steel are listed in Table 3.4. Using these and the sizes of the vacuum chamber, heat shield and source block given in Table 3.5 the various calculated heat loads are given in Table 3.6.

Clearly the vacuum chamber is a significant heat burden on the unshielded source block with about a 1/4 W load transmitted by thermal radiation. This can be attributed both to the large temperature difference, but also significantly to the very large surface area of the chamber's interior at room temperature.

The heat shield, which is removed in Fig 3.5 for visibility, is attached to a copper plate at the head of the cryostat. This plate, cooled by the LHe exhaust gases, reaches a temperature just below that of liquid nitrogen, so this effectively is the equilibrium temperature of the heat shield. The source block is effectively shielded from this heat load by a factor of nearly three hundred. The remaining heat load is insignificant considering the cooling capacity of the cryogenic system, and so clearly it is advantageous to use a heat shield around the source and cold-finger.

What may be surprising is the very significant heat load on the heat shield itself from the vacuum chamber, about eight times more than that directly on the source block. The reason for this can be seen in the other columns of Table 3.6. First, recalling that the heat flow equation is quartic in temperature, the difference in temperature is still about 3/4 of the total. Second, the view factor is an order of magnitude smaller than either other heat transfer calculation. Essentially the heat shield makes a larger target for thermal photons from the hotter surface, so it absorbs more heat.

3.3 The LHe cryogenic grounded hollow cathode He* Source

After a brief description of the LHe cooled, grounded hollow cathode (GHC) source and its variations, the remainder of this Chapter is devoted to reporting on the parameters and performance of this design. This includes data on the performance of this simple GHC source using the three lightest rare gas elements at temperatures just above their boiling points. Ultimately the optimum performance of the new source is compared with its predecessors.

3.3.1 Design

Basic hollow cathode

The basic features of the grounded hollow cathode source are shown in Fig 3.8. A hollowed copper block is bolted directly to the cold-finger using indium foil (Section 3.2.2) to maximize thermal flow. Helium is introduced through a copper tube, its sharpened end projecting into the cavity a short distance to attract electric field flux and precipitate starting of the discharge. A boron nitride insulating spacer allows a space for a positive column to ensure a stable discharge, before a metal nozzle/anode plate, both fixed by screws into the copper block, insulated where required. Gas leakage though the tight fitting parts is trivial compared with the flux through the nozzle.

Grounding of the hollow cathode permits many mechanical as well as electrical simplifications of this source design. It means the hollow cathode may be attached to the cold-finger in such a way as to maximize heat flow, and hence minimize the hollow cathode temperature, since good thermal conductors are inevitably good electrical conductors. It also means the helium gas supply can be made from continuous copper tubing, as there is no requirement to quench discharge flowing back through the gas line to ground. The discharge may be operated with a single HV power supply to the anode, requiring only one feed-through. This is permitted by the lowering of the required discharge voltage due to the hollow cathode.

Simple variations

Four permutations of the basic design in Fig 3.8 were tested for optimization of beam flux and beam temperature. These are illustrated in Fig. 3.9. Each has in common the hollowed copper block - the grounded hollow cathode. The permutations in design are achieved by simple variations of the nozzle and anode construction, the basic change being from a conducting to an insulating nozzle plate. In configuration

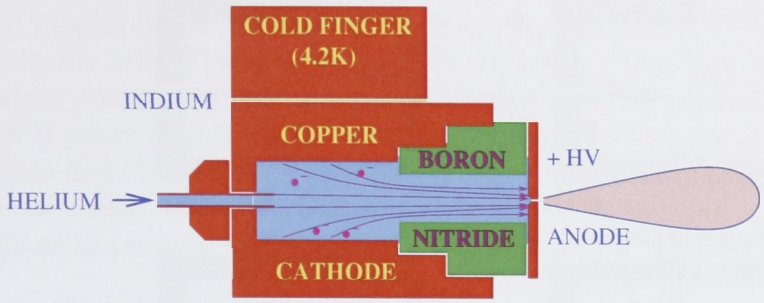

Figure 3.8: A schematic of the grounded hollow cathode source, based on a hollowed copper block ($3 \times 3 \times 5$ cm) attached to a liquid helium cooled cold-finger. Indium foil maximises the heat flow from the block. The large area hollow cathode surface maximises the electron current in the discharge, with the discharge initiated from the gas feed copper tubing. The insulating spacer extends the positive column to stabilise the discharge. The inner edge of the nozzle is rounded to focus the electric flux at the outer edge. Not shown are the screws fixing the nozzle to the block. Diagram not to scale.

A - *C* the insulating collar in Fig 3.8 is present: in configuration D it is removed.

In configurations *A* and *B* the nozzle plate is metallic (copper) and acts as the anode. Configuration A most closely resembles a common discharge configuration in Fig 3.2 punctured by a hole in one wall through which plasma particles leak. Therefore the metastable flux through the nozzle is largely determined by the metastable density within the discharge plasma. The nozzle is shaped to achieve the sharpest curvature at the outer surface in order to initiate the discharge at this point and thus maximize the excitation of atoms traveling through the nozzle itself.

The first variation of this basic design in Configuration *B* is the blanking off of the interior surface of the conducting nozzle plate with an insulating washer, so that the electric field flux is intensified around the nozzle.

Configurations *C* and *D* replace the conducting copper nozzle plate with an insulator (boron nitride), using an an aluminum ring just outside the nozzle as an external anode. This is similar to traditional discharge sources such as the ANU source (Fig 3.3), where the intention is to create metastable atoms within the nozzle or the plume just after, minimizing losses due to collisions within the source or nozzle. It is also obvious that there is a higher density of electrons in the 'sample volume' within the source from which atoms find a path through the nozzle. Configuration D is the same as configuration C but with the insulating boron nitride collar removed to increase the cathode surface area available for the discharge current.

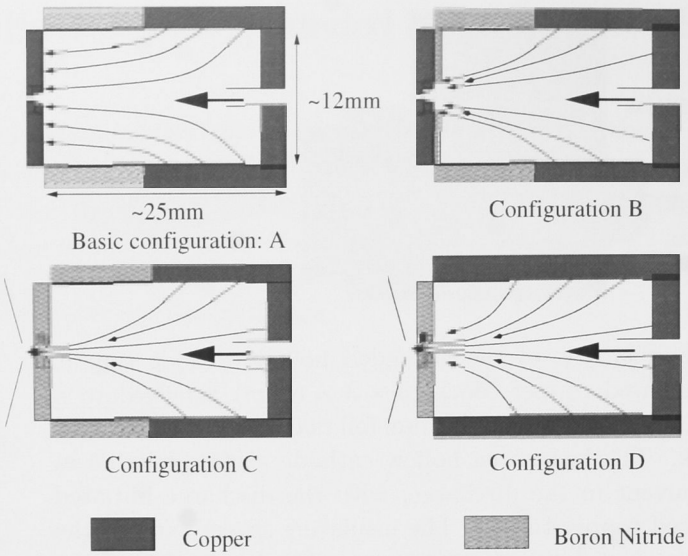

Figure 3.9: Hollow cathode discharge source with four design configurations. Gas inlet - large arrow, right; nozzle - left; other arrows indicate the discharge path. Configurations *C* and *D* have external anodes. Each nozzle configuration is secured by the same screws (not shown).

In general the progression from *A* to *D* increases the electron current density such that we may expect that each subsequent version will produce a higher flux of metastable atoms. However it is well understood that the momentum transfer from the electrons during collisions can substantially increase the velocity of the metastable beam. Our design requirement is to maximize beam flux *given* minimization of the beam temperature. It is not *a priori* obvious which of these designs will satisfy those criteria.

3.3.2 Characterizing the source

Operation in the source chamber

The hollow cathode source is mounted to the Janis cryostat suspended from the top plate of the source chamber as illustrated in Figure 3.5. The aperture for the cryostat in the top plate is extended with bellows so that the height and angle can be adjusted to optimism the location of the source block with respect to the subsequent beamline. Significant percentages in flux transmission are dependent on sub-millimetre alignment of the nozzle with the skimmer. This degree of control is achieved using three micrometers mounted in the seal plate supporting the cryostat on ball bearings.

Four half nipples in the top plate provide access for connections to the source. In addition to the helium gas line and one HV discharge connection, these include the temperature sensor and heater coil feed-through and a vacuum reference for the MKS Mk II gauge used to measure the helium gas drive pressure. Since all internal connections mate the same surface, the top plate can be lifted away from the source chamber as a unit. Ports into the source chamber provide access for measurement of the chamber pressure and optical alignment along the atomic beamline axis.

The source chamber is pumped by a 1400 l/s turbo-pump (Balzers-Pfeiffer TMU1601). The base pressure without a gas load is better than 10^{-8} torr[†]. The gas load is controlled by a calibrated needle valve cross-referenced to the millitorr MKS drive pressure gauge.

With a grounded cathode the source discharge can be maintained by a single power supply. The HV anode potential is connected through a ballast resistor to limit the discharge current. The constant current at operating voltages of a few hundreds of volts is monitored with a permanent milliammeter. The discharge can be started using a short 5 kV pulse at lower temperatures and pressures.

The hollow cathode sources operates easily at any temperature. At high temperatures (77 K to 293 K) and high pressures ($\geq$ 0.5 torr) the discharge will spontaneously ignite at potentials between 400 and 600 volts. At liquid helium temperature the conducting plate configurations (*A* and *B*) can spontaneously ignite at relatively high (900-1500 V) operational voltages. In the insulating plate configuration the lower density plasma between the nozzle and the external anode increases the potential required to maintain and especially ignite the discharge. In these cases (*C* and *D*) the 5 kV potential is used to start the discharge. Over the course of years the ultimate procedure became (for reasons mentioned below):

- set the High Voltage at operating voltage plus 5 kV;
- open the needle valve until the discharge ignites;
- switch off the 5 kV potential; and
- close the needle valve to operational levels, reducing the drive pressure, usually optimizing the beam flux measured down the beamline.

The background helium pressure during operation is $10^{-5} - 10^{-4}$ torr at typical source pressures of $0.1 - 1.0$ torr. Consequently, losses due to collisions in the source chamber are negligible. The metastable beam then passes through a skimmer, located $5-10$ mm from the nozzle, into the differentially-pumped beamline chamber that maintains a pressure of less than 10^{-6} torr.

[†]Aided by cryo-pumping of the cryostat in operation the base pressure has been measured in 10^{-10} torr range.

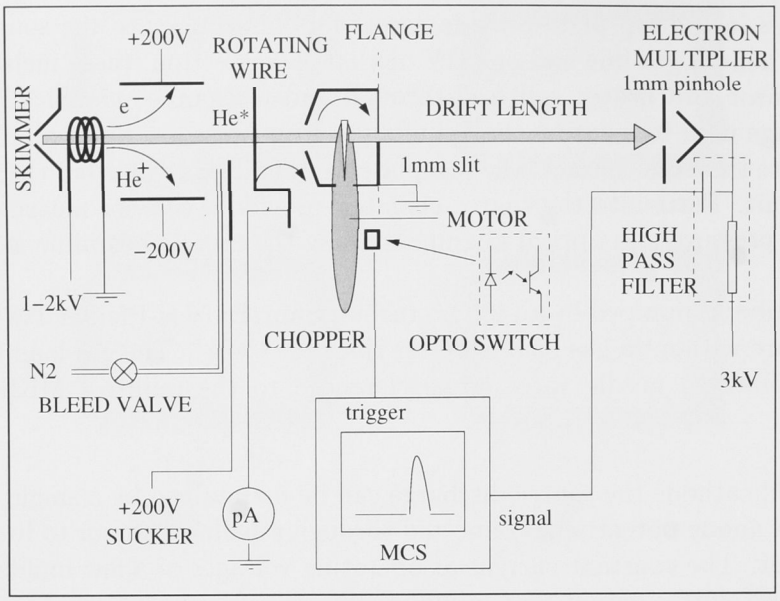

Figure 3.10: Experimental apparatus, showing beam conditioning devices and detectors, with time-of-flight system at right.

Experimental beamline

The components of the beamline used to measure the characteristics of the He* flux from the source are shown in Figure 3.10. This beamline reflects most of the components to condition and characterize a metastable atom beamline discussed in Chapter 2.

The first apparatus the beam passes through immediately after the skimmer is a glass-coil helium discharge tube. When ignited the light from this discharge quenches any atoms in the 2^1S_0 singlet metastable state. This permits the measurement of the ratio of metastable atoms produced in the singlet/triplet states.

Two parallel plates collinear with the beam are charged with a ± 200 V potential. The removal of charged particles in the beam by this electric potential allows the measurement of the ion fraction of atoms excited in the discharge source.

A bleed valve feeds nitrogen gas into the beamline chamber. By collisionally quenching the metastable atoms in the beam the proportion of UV photons in the beam from the source can be measured.

Next a wire detector mounted on a rotational feed-through can be translated across the atomic beam. With a potential on a second wire attracting ejected electrons, this current detector measures the atomic beam profile and divergence. The total

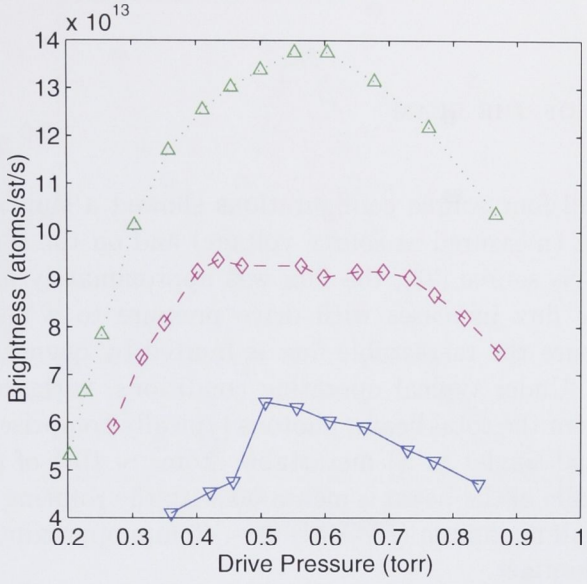

Figure 3.11: Atomic flux (to a precision of $\sim$ 1%) as a function of drive pressure for source voltages: 600V (∇); 1000V($\diamondsuit$); and 1500V ($\triangle$). Note that there is a discharge mode change at $\sim$ 0.45 torr, especially for lower discharge voltages.

beam current is measured by inserting a 40 mm diameter, 50% transmission stainless steel grid (not shown in Fig. 3.10.)

For time-of-flight (TOF) velocity measurements the atomic beam is chopped using an in-vacuo mechanical chopper, a 100 mm wheel with a 1 mm slot rotating at $\sim$ 60 Hz. Both UV photons and metastable atoms in the 2^3S_1 triplet metastable state emitted from the source are detected after the 1120 mm drift distance L_{TOF} by an ETP electron multiplier. The start time $t_{TOF} = 0$ is taken from the photon peak. To control the detected flux and reduce stray UV light reflections that reduce temporal resolution, the beam is collimated by a 1mm fixed slot at the chopper wheel and a 1 mm pinhole at the detector. The electron multiplier signal is collected by a multi-channel scaler (MCS) which is triggered by an opto-reflective switch aligned with a hole in the chopper wheel. Therefore the data file contains three significant time values: the trigger time, the photon peak $t_{TOF} = 0$, and the atom peak t_{TOF}.

3.3.3 Results

General properties of the beam

The atomic flux from all four source configurations showed a similar dependence on the discharge current (measured as source voltage) and on the source pressure. As for the ANU liquid-N_2 source [93], the flux was approximately linear with the discharge current. The flux increases with drive pressure to a maximum at $\sim$ 0.5 torr, at which pressure the metastable flux is limited by quenching collisions, as shown in Fig. 3.11. Under typical operating conditions, with the $\sim$ 50% ion contribution removed from the total beam, photons typically comprise $\sim$ 20% of the remaining beam flux, and singlet (2^1S) metastable atoms $\sim$ 10% of the remaining flux. The transverse profile of the beam is measured with the rotating wire, and has a typical full width at half maximum (FWHM) of $\sim$ 40 mm approximately 260 mm downstream from the skimmer.

Figure 3.11 shows the variation of beam brightness with drive pressure for three discharge powers (measured by source voltage). At first increasing pressure simply increases the number of atoms available for excitation to the metastable state. At higher pressure the increased density in and after the nozzle increases the probability of inter-atomic collisions that quench the excited states. The resulting maxima of the curves are approximately independent of voltage. The three plots also demonstrate the flux increases with voltage typical of a rare gas discharge source (e.g. [93]).

An important quality of the hollow cathode sources is most visible in the lowest energy discharge at 600V (∇ - points), an asymmetric mode change in metastable production. Reducing the drive pressure from higher pressure (0.9 torr) the flux increases to a maximum at $\sim$ 0.5 torr. Below this the flux suddenly decreases by up to 30 percent. Restoring the flux maximum at $\sim$ 0.5 torr requires following a hysteresis path, first increasing the drive pressure to 0.9 torr as well as possibly applying a higher voltage.

Velocity of the beam flux

The TOF spectra exhibits two signal peaks: an instantaneous peak due to UV photons from the discharge, and the 2^3S atom peak following the drift time. The photon peak determines t_0, the zero of the time scale. The velocity distribution Eq 3.7 is derived from the measured atom signal using the transformations in Section 2.1. Comparison of the position and width of the measured velocity distribution with calculated distributions in Fig 3.12 indicates that the source is supersonic, rather than effusive, with a Mach number of $\sim$ 3 under the conditions shown (source con-

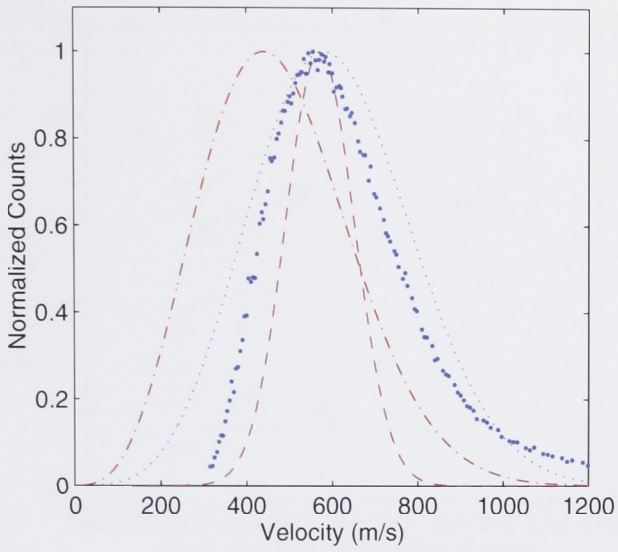

Figure 3.12: Effusive (red dash-dot) and supersonic (M=1, black dots; M=5 magenta dashes) velocity distributions for a source temperature of ~25 K as a function of Mach number. The data points (blue) are taken using the final version of the liquid-He cooled source at a pressure of 0.36 torr, 600 volts.

	B	$\bar{v}$	σ_v	σ_v		B	$\bar{v}$
	(at/s/sr)	(m/s)	(m/s)	(%)			
A	1.82×10^{12}	443	49	11.1	B/A	22×	1.1×
B	4.01×10^{13}	491	21	4.3	C/A	23×	1.0×
C	4.19×10^{13}	455	19	4.2	D/A	66×	1.1×
D	1.21×10^{14}	487	21	4.4	D/C	3×	1.1×

Table 3.7: Summary of brightness and velocity measurements for grounded hollow cathode source configurations A-D, and comparative results

figuration D, pressure ~ 300 mtorr and voltage 400 V). The velocity ranges and atomic flux are shown for the various source configurations in Fig 3.13. Note that at the measured cryostat cold-finger temperature during source operation (5 K), the average velocity for an effusive molecular beam is $1.33\alpha \sim 200$ m/s [70] where

$$\alpha = \sqrt{2kT/m} \tag{3.13}$$

and k is Boltzmann's constant with m the mass of the atom. The fact that the measured average velocities are significantly higher is a combination of the discharge temperature being higher than the surrounding environment, and the source operating in the supersonic regime.

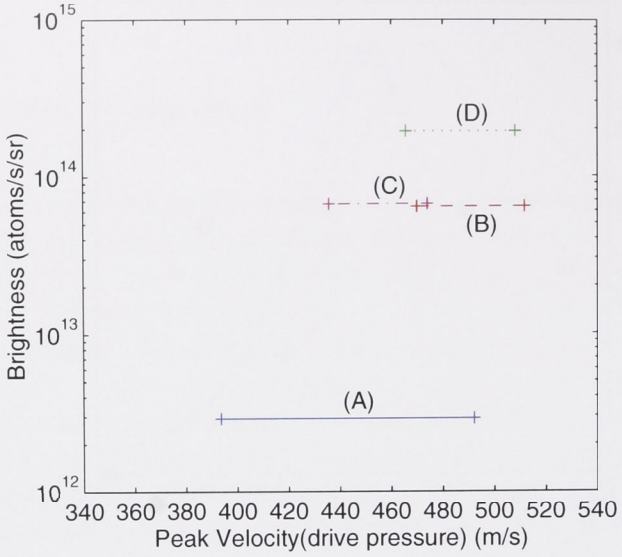

Figure 3.13: The atomic flux and velocity ranges ($\propto$ drive pressure) for the four source versions in Fig.(3.9), at minimum operating voltages.

The optimization parameters of brightness and velocity for the four configurations are plotted in Figure 3.13 and Tables 3.7. There is little difference in average velocity between the source configurations operating under similar conditions. As expected, the external anode sources (configurations *C* and *D*) yield higher fluxes as a result of the discharge being present well into the collision-free region. The highest flux is produced by the external anode source without the insulating collar (configuration *D*) for which there was only a small increase in average velocity. Consequently, this configuration was adopted for subsequent investigations.

To determine whether the source could be operated closer to the effusive regime, the average velocity was measured as a function of source pressure. Figure 3.14 shows a reduction in average velocity to just over 450 m/s at the lowest pressures at various discharge currents. The lower pressures resulted in a significant reduction in flux, so a compromise operating condition of $300 - 350$ mtorr and $400 - 600$ volts was adopted.

The average velocity can also be reduced by optimising the nozzle diameter, while at the same time optimising the flux. Fig 3.15 illustrates the effect of nozzle size on the beam flux at the operating conditions above. Both the highest flux and the lowest velocity were obtained for a 1.0 mm nozzle diameter, which was adopted as the optimum nozzle configuration, illustrating the competition between collision processes in and after the nozzle.

The smaller 0.5 mm diameter nozzle passes the expected 75% reduced flux by nozzle

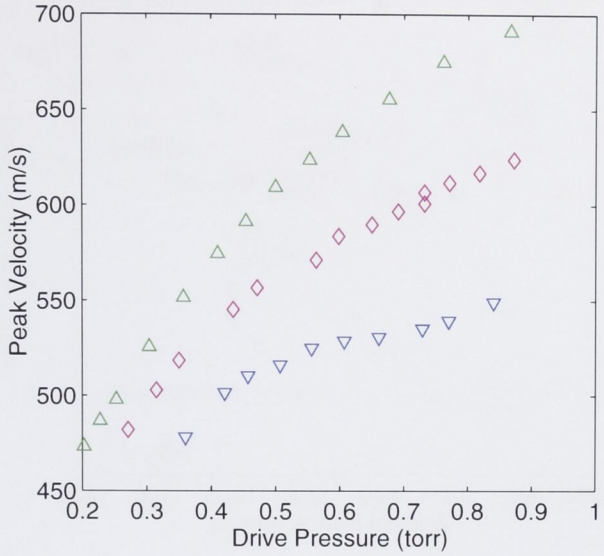

Figure 3.14: Peak velocity, for source D, as a function of drive pressure for source currents: 2.7mA (∇); 5.0mA ($\Diamond$); and 8.2mA ($\triangle$).

area (see Eq. 3.2) but the atoms encounter more thermalising collisions with the nozzle walls transfering kinetic energy from transfers to axial direction, resulting in the higher range of velocities produced by a more supersonic flow.

The larger number of metastable atoms permitted through the larger 1.2 mm diameter nozzle are accompanied proportionately more neutral atoms and ions (see Sec 3.3.3) creating a significantly higher background pressure. As a result there are many more quenching collisions with background atoms in the source chamber, clearly reducing the flux, especially of slower atoms.

The maximum brightness exceeding $\sim 10^{14}$ atoms/sr/s is an order of magnitude less than our previous liquid-N_2 cooled source [93] but the average velocity is reduced by a factor of two.

The continuous flow cryostat could be operated using liquid N_2, and Fig. 3.15 also shows the brightness and velocity obtained at these temperatures. Once again the 1.0 mm nozzle yielded the best performance with a velocity ($\sim$ 1000 m/s) comparable to our liquid-N_2 cooled source reported previously in our needle discharge source [93] and a flux exceeding ($\sim 10^{14}$ atoms/sr/s).

Since the cryostat is capable of operating at a fixed temperature (monitored by the silicon detector and adjusted using a heating element and rate of LHe flow), the source can be used to generate a range of metastable atomic species when operated just above their condensation point. Fig 3.16 shows the source flux and velocity

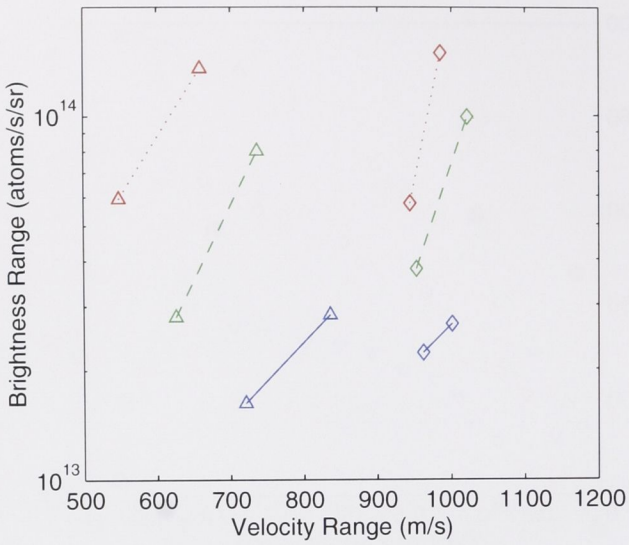

Figure 3.15: Range of beam flux vs velocity for liquid He (△) and liquid N_2 (◇) cooling for nozzle diameters: 0.5 mm - solid; 1.0 mm - dots; 1.2 mm - dashes.

obtained using He (5K), Ne (25 K) and Ar (90 K) at optimum flux conditions. Although the α values (3.13) for He ($\sim$ 200 m/s, 5 K), Ne ($\sim$ 150 m/s, 25 K) and Ar ($\sim$ 260 m/s, 90 K) are similar at these source temperatures, the average velocity for He is found to be considerably higher, suggesting greater susceptibility to electron momentum transfer. The flux for argon is also notably lower under these operating conditions. This is a typical result, attributed to the cluster formation in the discharge plasma.

3.3.4 Optimum source design for a high flux, low velocity beam

The optimal grounded hollow discharge source configuration comprises an external anode placed in the collision-free region downstream from a 1.0 mm diameter nozzle in a boron nitride cap, located at the end of a cylindrical hollow copper cathode (labeled configuration *D* in Fig 3.9.) In this optimal configuration the source generates a metastable helium beam with a brightness exceeding $\sim 10^{14}$ atoms/sr/s and $450 - 700$ m/s average velocities. Its performance is summarized in the plot of brightness versus velocity in Fig 3.16, including the optimum points for producing metastable beams of helium (5 K) (+), neon (25 K) ($\times$) and argon (90 K, $*$).

Ten major He^* sources reported in the past 15 years are plotted for comparison. These include four sources that operate at room temperature (∇) [104, 106, 113, 114], five that operate at liquid nitrogen cooled cryogenic temperatures (◇) [14, 23,

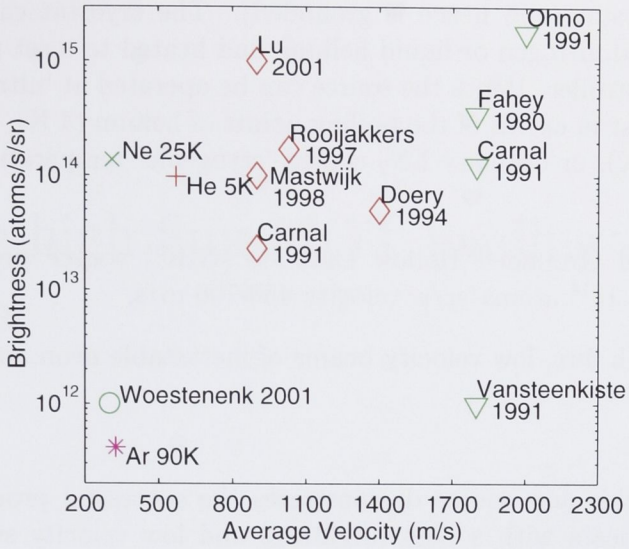

Figure 3.16: Flux and velocity for metastable gas sources: for the new source three metastable species (cold-finger temperature): helium, 5 K (+); neon, 25 K ($\times$); argon, 90 K ($*$); other referenced sources at 300K (∇, Carnal [113] Fahey [104] Ohno [106] Vansteenkiste [114]), 77K ($\diamondsuit$, Carnal [113] Doery [115] Lu [93] Rooijakkers [14] Mastwijk [23]) and $\sim$5 K($\circ$, Woestenenk [34]) .

93, 113, 115] and one that operates at liquid helium temperature ($\circ$) [34].

Of particular interest are the LN_2 cooled source of the ANU bright beam machine [93], and the LHe cooled source in Reference [34]. The LHe cooled GHC source brightness is an order of magnitude lower than the ANU liquid-N_2 cooled source but with considerably lower average velocities. In comparison with the LHe cooled source in Reference [34], the somewhat higher average velocity of the GHC source is offset by the two orders of magnitude increase in flux.

3.4 Conclusion

This chapter has presented a novel design for a metastable gas source of an electron discharge type, the first component of our compact, MOT loading beamline.

- The source utilises the increased electron current density of a hollow cathode design to sustain a higher discharge current, exciting more metastable states, at a lower gas pressure.
- Easily fabricated from a copper block, the source is connected directly to a

commercial cryostat (and hence is grounded). The cryostat can be cooled with either liquid nitrogen or liquid helium, and heated to a set point with a temperature controller. Hence the source can be operated at 'ultra-cryogenic' temperatures just in excess of the boiling points of helium (4 K), neon (25 K) and argon (90 K), or ordinary LN_2 cooled 'cryogenic' temperature ($\sim$80 K) for He and Ne.

- The LHe cooled Grounded Hollow Cathode (GHC) source produces high brightness 1.2×10^{14} atoms/sr/s, velocity 450-700 m/s.
- Comparably high flux, low velocity beams of metastable neon and argon can be achieved.

The performance of this new source demonstrates the successful production of a metastable rare gas beam with a high brightness and low velocity suited to the application of a compact MOT loading beamline. This beamline is explored in the next Chapter.

CHAPTER 4

A simple high flux MOT loading He* beamline

A metastable helium beamline between the source and magneto-optical trap must satisfy two principle criteria: differential pumping between the source chamber vacuum and the MOT chamber; and slowing and guiding the maximum number of atoms emitted by the source to trapping velocities in the trapping volume.

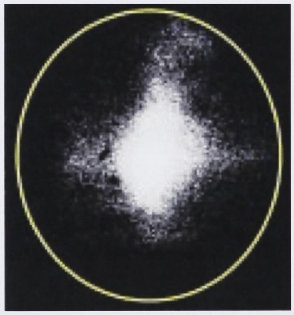

Figure 4.1: The LHe cooled He* beam collimated by 2-dimensional molasses in the retro-reflecting mirror array shown in Fig 4.2. The image is captured on a 40 mm diameter MCP and phosphor plate, the edge of which is circumscribed.

The operating pressure in the first beamline chamber is still $\sim 10^{-6}$ torr. Several differential pumping stages, with limiting apertures between vacuum chambers, are required to reach MOT experimental pressures. Steering the He* beam through those apertures (as well as any slowing of the atoms), requires atom optic stages in the beamline. An added complication for discharge sources is that the direct beam of metastable atoms is accompanied by a direct beam of ground state atoms that loads background gas in the final vacuum chamber. Steering the metastable atoms off axis means the ground state atom path to the MOT chamber can be blocked. This chapter considers the development of the atom optical stages of the compact MOT loading beamline.

4.1 Simple atom optics for a LHe MOT loading beamline

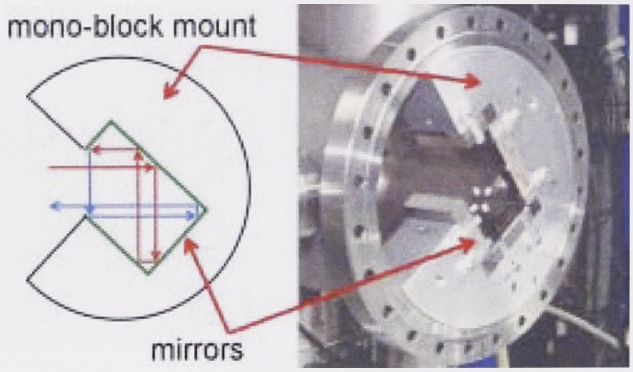

Figure 4.2: The 2-D retro-reflecting mirror array is mounted *in vacuo* in a mono-block, here pictured in the mouth of the first beamline vacuum chamber. The mono-block mount is aligned with the optical port just visible at the photo's left for injection of the single laser beam. The first chamber is part of a T-chamber containing the source (out of view to left) and skimmer mounting plate for differential between the two vacuum chambers.

The initial plan for the compact LHe cooled He* beamline proposed to dispense with atom slowing and load the MOT with trappable atoms from the low end tail of the beam's velocity distribution. A minimum number of stages of simple two dimensional optical molasses would direct those slower atoms along a path enabling differential pumping into the MOT trapping region.

For simplicity and low cost the 2-D molasses are made using an *in vacuo* retro-reflecting mirror array with a single optical port for the injected laser field, as illustrated in Fig 4.2. Each interaction region is 25 mm in height/width and 50 mm in length. Since the mirrors and mounts are both flat and parallel there is no Doppler tuning effect (compared with the curved wavefronts in the ANU Bright Beam Machine, Sec 2.4) and the light field only interacts with those velocities within the linewidth of the laser.

4.1.1 Collimation

The divergent atom beam should be collimated as close as possible after the skimmer aperture into the first beamline vacuum chamber. Taking into account the height of the skimmer cone and the construction limitations of the blocks and the chambers, this is about 10 cm. Assuming a worst beam divergence of $\sim$0.1 rad all of the atoms are still in the light field when they enter the interaction zone, hence the collimated beam width is about the size of this zone, about 2 - 2.5 cm diameter.

An image of the LHe cooled source beam collimated by these molasses is illustrated in Figure 4.1. The image was collected by a 40 mm MCP and phosphor plate a metre downstream. Even at this distance the high flux of the divergent He* beam totally saturates the full face of the detector, circumscribed in Fig 4.1, so that the focusing in two dimensions is evident by the narrowed beam image. The transverse spatial profile of the He* beam was measured using a wire probe. The performance of three different molasses fields is shown in Figure 4.3, each achieving some degree of collimation of the diverging atom beam. This is sensitive to the laser detuning, which adjusted around ~-10 MHz to maximise collimation.

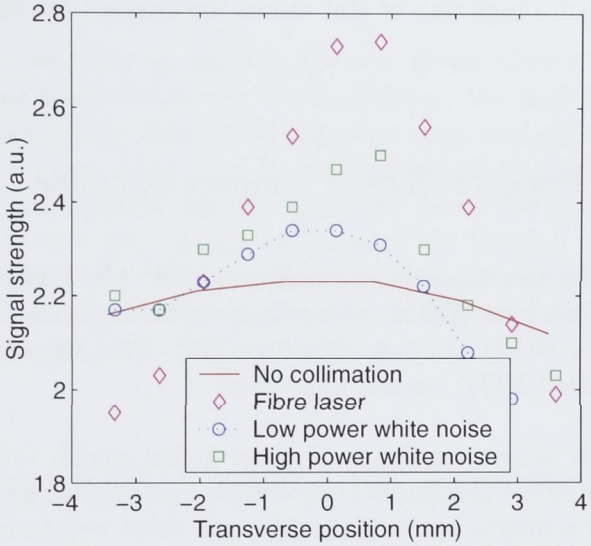

Figure 4.3: The results of optical molasses collimation of the GHC source He* beam in 2-D retro-reflecting array using the linear polarisation 50 mW SDL 6702-HI diode laser with its ordinary linewidth Fig 2.4 ('low power white noise'), the white noise broadened linewidth of the modulated diode laser ('high power white noise'), and the fibre laser at a fraction (100 mW) of total power. In each case the detuning (~-10 MHz) was adjusted to maximise collimation. The small shift in the peak centre is most likely due to variation in alignment of the block and injection beam between each configuration.

1. The base laser available was the SDL 6702-HI diode laser producing a maximum 50 mW optical power. The laser's ordinary linewidth (Fig 2.4) is unaltered by low power frequency modulation ('low power white noise').

2. The linewidth broadening 'white noise' technique investigated in Sec 2.3.1 with this laser was utilised for the collimation molasses.

3. Spectrally narrow but intense light was available from a fraction (100 mW) of output from a fibre amplified diode laser.

The atom beam is clearly collimated by the light field with the normal laser linewidth at 'low power white noise'. Applying broadband light ('high power white noise') achieves a small gain in collimation, but with the SDL 6702-HI diode 50 mW power distributed over a broadened spectral ranges the collimation effect was less than that of the power broadened fibre laser at just 100 mW. The small shift in peak locations is most likely caused by small shifts in the injection angle of each laser field or the alignment of the mono-block.

It is impossible to precisely measure the beam collimation from such a broad source with just one detector, but these results indicate that the simple in vacuo retro-reflecting stage can direct a high flux of He^* atoms towards a 1 cm target at about one metre.

4.1.2 Reconceptualising an efficient compact beamline

In the background of the development of our second He^* MOT loading beamline the ANU bright beam machine (BBM) is regularly operating with a high loading rate sufficient to achieve MOTs of a few 10^9 atoms [27]. This set a benchmark for performance of a dedicated MOT loading apparatus.

This is reinforced by the source results of Chapter 3 that match the performance standards of the BBM source. The implication is that a reasonable beam line design could achieve MOTs of a magnitude comparable with those regularly produced at ANU and elsewhere.

In this context the performance of the MOT loading LHe cooled beamline in Reference [34] was instructive: accounting for the different He^* production of the respective sources (two orders of magnitude below that of the GHC source) the cost of the 'simplified' beamline in their design was a further order of magnitude loss in trapped atoms. This is before consideration of the higher velocity distribution of our LHe cooled GHC source.

Reconsidering the short beamline design was assisted at this time with the release onto the market of high power fibre-amplified diode lasers at 1083 nm capable of more than an order of magnitude more optical power per experimental dollar with turnkey operation. These lasers reversed the practical consideration that sought simple atom optical stages to minimize power requirements.

Therefore the short beamline was re-conceived using a new set of principles:

- The best beam slowing tool is a standard Zeeman slower, but specifically designed to optimise performance and minimize length.

- Reference [34] demonstrated the success of capturing divergent atoms directly from the exit of the slowing region, so the Zeeman slower is positioned as close as possible to the MOT.
- A simple collimator is located as close as possible to the skimmer so that the maximum number of atoms are captured into the beam at the smallest possible diameter.
- A simple 'push' beam deflects the He* atoms off the central axis into the mouth of the Zeeman slower, so that the ground state gas load is blocked from the MOT chamber, to achieve the required differential pumping.

With the 35 mm diameter, ~1 m long Zeeman slower tube comprising the final differential pumping stage before the MOT chamber, the final requirement of this beamline is an intermediate differential pumping stage and the removal of the on-axis gas load. The beam collimated in the first chamber passes through a 1 cm aperture into the intermediate vacuum chamber. Here the He* beam is deflected by the 'push' beam into the off-axis entrance of the Zeeman slower, from which the ground state atoms are blocked. This completes the load reduction from the source to the MOT chamber in the required length. The experiment now is compact enough to fit on a single 1200×2400 mm optical table.

4.2 The compact MOT loading He* beamline

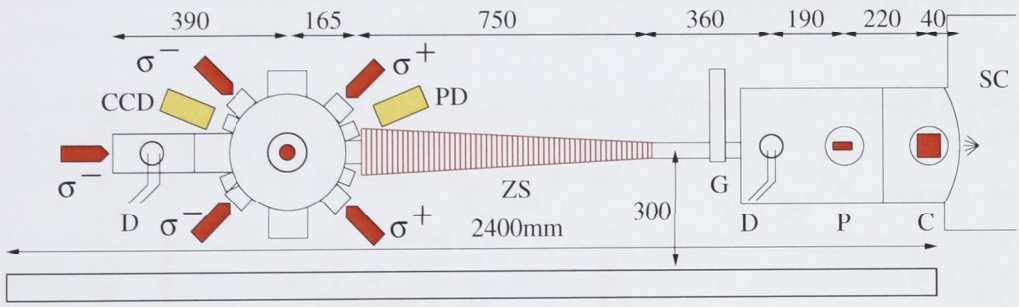

Figure 4.4: The side view of the Compact He* Beamline above a 2.4m optical table, with the source chamber (SC) and vacuum pumps omitted for clarity. Indicated are: C - collimator; P - push beam; D - wire detectors; G - vacuum gate; ZS - Zeeman slower; PD - photodiode; and CCD - camera. All measurements are in millimetres.

A schematic of the compact beamline is shown in Fig. 4.4. Immediately after the skimmer the He* beam is first collimated in 2-D molasses with a 5 cm interaction length (C), using the recirculating in-vacuo mirror array of Section 4.1. By manufacturing a single T-chamber for the source chamber and first beamline chamber the

Laser beam	δ_{rel}	δ_{rel}/Γ	P	Size	I	I/I_{sat}
Collimator	-11.6	-7.3	100	50×25	8	40
Push	-11.6	-7.3	100	50×5	40	250
Slower	-637.2	-400	190	25Ø	38	30

Table 4.1: Principal light field frequencies (MHz), powers (mW), sizes (mm) and hence average intensities (mW/cm^2).

spacing between the source and collimation stage was reduced to 4 cm. Collimation maximizes the flux through a 1 cm aperture, 25 cm downstream from the source, to the second chamber. Here the atomic beam is bent approximately 1.7° by another 5 cm interaction zone (P). After 55 cm the metastable beam is 1 cm off-axis where it passes into the Zeeman slower (ZS). The direct path for ground state atoms from the source is blocked, and they are pumped away. This second chamber maintains a background pressure of a few 10^{-8} torr.

Differential pumping through the Zeeman slower is enhanced by its length (0.75 m) and a 270 mm long, 10 mm diameter tube located in the slower's entrance. The MOT centre is 165 mm after the slower exit so that the Zeeman slower immediately loads the MOT chamber. Base pressure in the MOT chamber reaches a few 10^{-10} torr with baking, but working MOT pressures can be achieved within a turn-around of one day of venting to atmosphere.

4.2.1 The optical layout

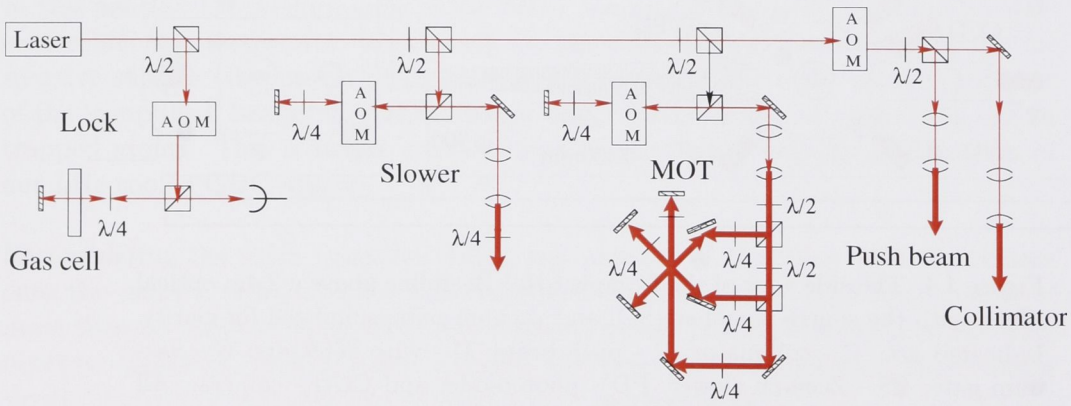

Figure 4.5: All light fields for the compact He* beamline are derived from the one laser. The major beams shown are for the lock, push/collimator beams, Zeeman slower and MOT beams.

All the light fields for this experiment, including collimation, slowing, trapping

and probe beams, are derived from a single laser using acousto-optical modulators (AOMs) to detune each to the required frequency shift. The laser is a Keopsys fibre-amplified diode laser capable of a total output of three watts. The optical layout is shown in the schematic in Figure 4.5

Approximately 25 mW of this output is double passed through a helium discharge gas cell, shown in the left hand of Fig 4.5, in order to lock the laser to the 2^3S-2^3P_2 transition by the saturated absorption spectroscopy method described in Lu *et al.* [116]. The retro-reflected beam passes over itself, eliminating the Doppler broadening of the absorption profile, since the only atoms that don't absorb light from the retro-reflected beam are the $v_{||} = 0$ atoms that were saturated on the first pass. Thus in the centre of the broadened absorption profile is the narrow saturated peak that, converted into a dispersion signal with a lock-in amplifier, is used to lock the laser detuning. The lock beam is double passed through a 125 MHz AOM before the gas discharge cell so that the main beam is shifted by ~-250 MHz.

All the major beams (push-beam, collimator, slower, the three MOT beams) are split off the main source beam using half-wave plate and polarizing beam splitting (PBS) cube pairs, allowing control of the power in each beam. The detuning of each beam is set using AOMs before they are expanded to experimental size. The operational values of intensity and detuning (relative to the atomic resonance) are shown in Table 4.1.

The push and collimation detuning is set by a common AOM shifting the frequency back to a range close to resonance. They are then separately enlarged for their 50 mm long interaction length using cylindrical lenses. Stray magnetic fields have a negligible effect compared to beam power balancing and He^* velocities.

The slower laser beam converges from an initial ~25 mm diameter such that it is just larger than the 1 cm aperture in the Zeeman slower entrance, approximately 1.2 m from the rear view port.

To facilitate the ease of day-to-day MOT loading a series of simple detectors are installed in the beamline. The first measures the current at the entrance to the Zeeman slower. This is a 1 cm diameter stainless steel disk mounted on a rotational feed-through can measure the He^* flux in the MOT direction.

At the end of the compact beamline is a cross chamber after the MOT chamber (just visible in the RHS of Fig 5.2). The perpendicular axis of this chamber supports a pair of stainless steel plate detectors on a rotational manipulator. The flux through the trapping region can be measured with the second identical one centimetre disk or with a 25 mm diameter ring located approximately 25 cm after the MOT centre.

Both signals are measured with a picoammeter. With this pair of detectors the whole beamline can be recursively optimised to maximise the (unslowed) beam flux

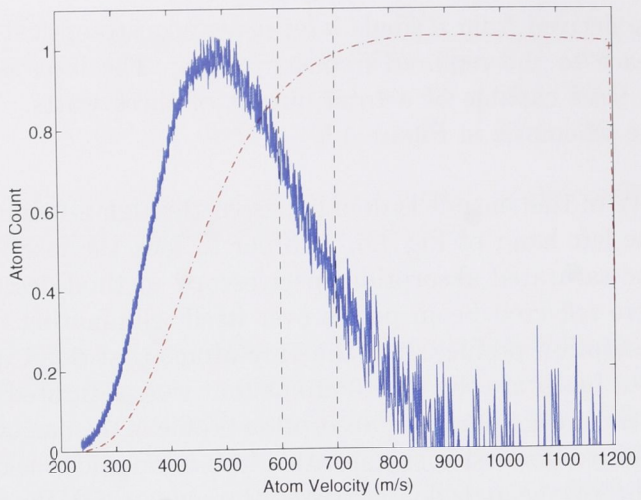

Figure 4.6: The TOF data of the beam of atoms entering the Zeeman slower, i.e. after the push beam, from the compact beamline is shown as the normalised velocity distribution peaked at ~450 m/s. The cumulative velocity distribution shows that > 90% of atoms in this beam are below the capture range 600-700 m/s of the Zeeman slower.

into the trapping region.

The end of the beamline is the optical entrant port for the Zeeman slower laser field. A micro-channel plate (MCP) to examine the atomic beam can alternatively be mounted to the beamline's end.

4.3 The slower loading performance

A high flux of atoms into the Zeeman slower requires the efficient collimation and bending of the low velocity (i.e. less than the Zeeman slower's capture velocity) component of the source flux. The collimator stage uses the simple retro-reflecting array of four mirrors mounted *in vacuo* examined in Sec 4.1.1, and the atomic beam is bent by a single 50 mm long laser beam. Both these light fields are derived from the same laser and hence are at the same detuning given in Table 4.1. In practice the maximum atom signal was found for approximately equal power in each of the light beams. The current detectors measure an equivalent of $7.5 \times 10^{10} s^{-1}$ typical flux in the bent beam, and $1.5 \pm 0.5 \times 10^{10} s^{-1}$ atoms at the end of the beamline.

The properties of this atomic beam at the end of the beamline were measured using a 40 mm micro-channel plate (MCP) and phosphor screen. The MCP blocks access for the slower laser beam so this permits only the measurement of the spatial

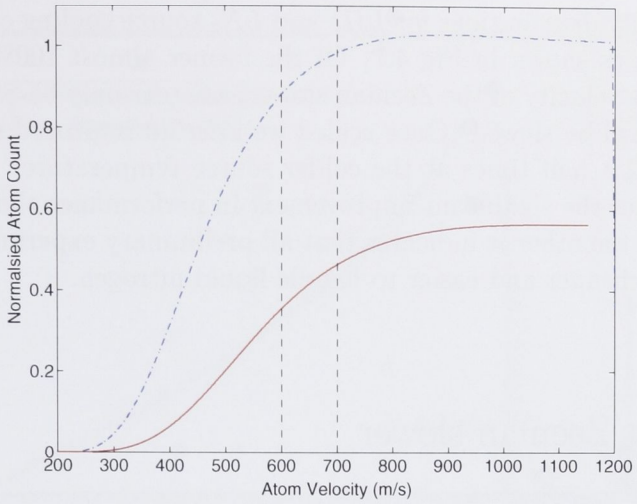

Figure 4.7: The cumulative velocity distribution for LHe cooling of the source compared with that for LN_2 cooling scaled by the total measured flux.

and velocity distributions of the collimated and bent atomic beam arriving in the trapping region. The image of the beam with MCP and phosphor gives us an estimate of the FWHM of ~20 mm, which means that the 10 mm diameter disk underestimates by $\sim 3\times$ the beam flux. This width is at a distance 1.295 m after the end of the 10 mm constriction tube in the entrance to the Zeeman slower, at which point we estimate the atomic beam has a FWHM of ~6 mm. Making a linear approximation of the expansion of the atomic beam the divergence is $(\sigma_f - \sigma_i)/L = 4.6$ mrad.

As discussed in Sec 2.2.1, transverse heating by recoil momenta causes significant diffusion of the beam during the slowing interaction. Using the same basic calculation the divergence of the beam slowed from 700 m/s to 70 m/s is estimated at $\sim$ 100 mrad. It is expected the beam will expand to ~40 mm width crossing the distance of 165 mm between the Zeeman slower and the trap centre. This is slightly larger than the 38 mm diameter trapping beams so that all but the most divergent of the slowed atoms are expected to be captured.

Using the phosphor as a collector plate instead of an imaging plate and the collimator/push beam pair as a gate permits collection of TOF data on the velocity profile of the atomic beam as it enters the Zeeman slower. A sample profile is plotted in Fig 4.6. This figure shows the velocity distribution of the optically bent atomic beam peaks about 450 m/s. Also plotted is the cumulative distribution that illustrates the important property that more than 90 percent of atoms in this beam are at a velocity less than the capture range of the Zeeman slower shown in the following Section 4.4. This means that the total beam current at the end of the beamline measured above should be slowed to trappable velocities.

The cumulative velocity distributions for LHe and LN_2 source cooling can be scaled by the measured flux as shown in Fig 4.7. Of the former almost 100% are within the maximum capture velocity of the Zeeman slower, whereas only 65-85% of atoms from a LN_2 sources will be slowed. Once scaled we infer an improved trap loading rate of up to two and a half times at the colder source temperature. On the one hand this demonstrates the significant improvement in performance though cooling the source to 4 K: on the other it indicates that all preliminary experiments can be performed using the cheaper and easier to handle liquid nitrogen.

4.4 An efficient Zeeman slower

The Zeeman slower for the compact LHe beamline was designed by Johanna Nes and tested by Tom Hanna and its major features reported in detail in [10].

In Section 2.3 it was noted that the choice of sign in Eq 4.1 for the Zeeman slower magnetic field poses a design question that has generated a range solutions. Combined with the additional criteria for close spacing between the end of the Zeeman slower and the MOT, the most elegant solution is a σ^- slower [117], where the sudden reduction of the field to zero near the exit rapidly shifts the atoms out of resonance. The MOT on axis with the atomic beam is then far off resonance with the slower laser.

The optimum magnetic field for Zeeman slowing was given in Eq 2.30:

$$B(z) = B_b \pm B_t\sqrt{1 - z/z_0} \tag{4.1}$$

Producing a magnetic field that follows this equation to a high precision produces a high slowing efficiency by accurately keeping the atoms in resonance. Therefore the efficient design of a Zeeman slower coil can shorten the length of the beamline. Loss of flux due to atomic beam divergence is in turn reduced because the whole slower is shorter. So a more precise magnetic field will allow a correspondingly lower power.

The coils of the Zeeman slower are wound round a 750 mm vacuum tube with a 38 mm internal diameter, with water-cooling between the inner tube and the copper coils to prevent overheating. The field coils were carefully designed to produce a magnetic field that closely matches that of the model based on Eq 4.1, as illustrated by Fig 4.8. In the compact beamline this is combined with a nulling coil at the exit of the slower to reduce the magnetic field to a negligible magnitude (< 50 mG) in a short distance ($\sim$165 mm), as shown in Fig 4.8. Hence the MOT can be formed within 200 mm of the slower exit.

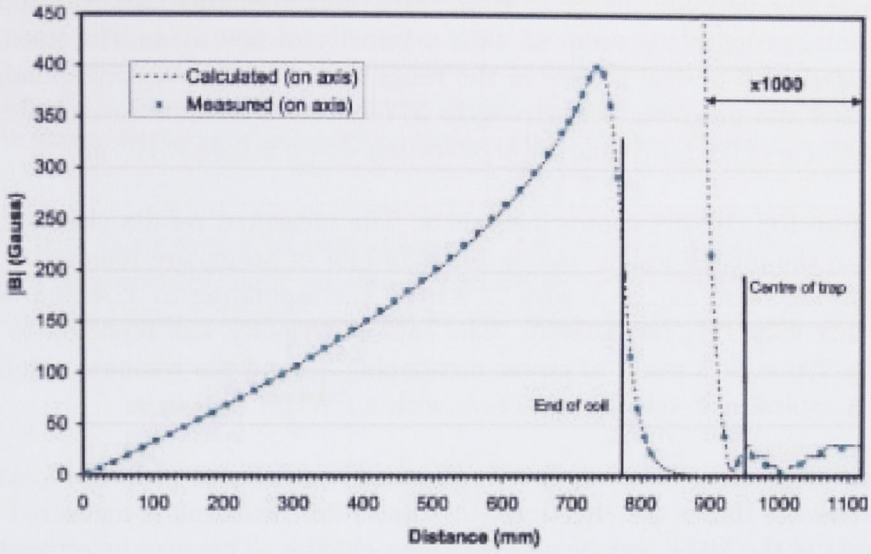

Figure 4.8: The measured magnetic field strength along the axis of the Zeeman slower closely follows the form calculated using Eq 4.1 to maximise the slowing efficiency by keeping the atoms in resonance. The large magnetic field at the exit is effectively reduced over four orders of magnitude at the trap centre by the nulling coil. Illustration from Ref [10].

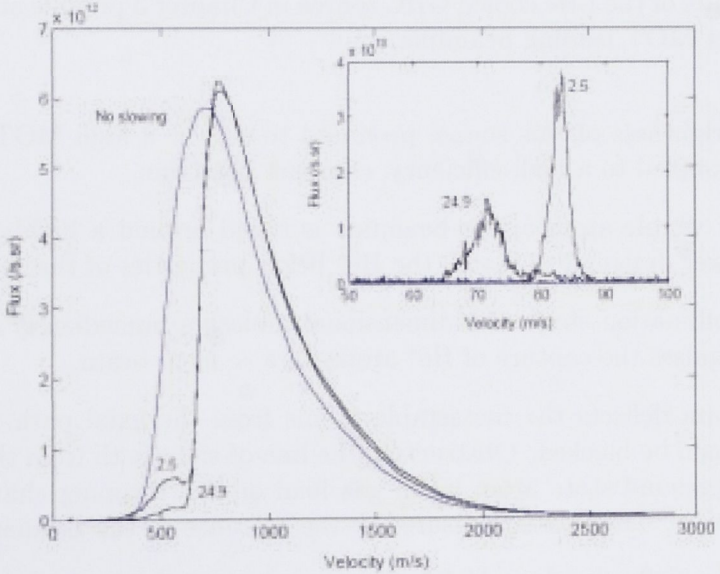

Figure 4.9: The Zeeman slower efficiently slows ~80% of the flux below 700 m/s with powers from 2.5 to 25 mW. A typical exit velocity is 70 m/s with a FWHM ~10 m/s (inset). Illustration from Ref [10].

The Zeeman slower detuning is set to -637 MHz, corresponding to the Doppler shift of a counter-propagating atom at with a velocity of 690 m/s. The Zeeman slower was tested with optical powers in the range 0.96 - 24.9 mW, corresponding to $s_0 = 10 - 264$ and magnetic field strengths 377.7 - 432.2 G. This corresponds a design parameter η of 0.68-0.70 and an acceleration $a = \eta \times 0.69 \times 10^6$ m/s^2.

The results from Ref [10] are shown in Fig 4.9. The measured results closely corresponded with the model design. Below 700 m/s 71% of atoms are removed with 2.5 mW of slowing light, and 82% with 24.9 mW, corresponding to 32% and 38% of the total flux with LN_2 respectively. The capture velocity was reported to be approximately 700 m/s, a result of power broadening around the resonant velocity of 690 m/s. A typical exit velocity is 70 m/s with a FWHM ~10 m/s.

In the compact beamline the slowed He* flux cannot be measured without blocking the Zeeman slower. Hence the effectiveness of the total beamline is measured by the loading rate of the MOT, examined in the next chapter. This may be estimated at $1.2 \times 10^{10} s^{-1}$ combining the results from Sec 4.3 with the performance of the Zeeman slower.

4.5 Conclusion

The excellent results of the LHe cooled GHC source in Chapter 3 provide an optimal start to a compact MOT loading beamline.

- The high brightness of this source promised to deliver a high MOT loading rate when coupled to a high efficiency, compact beamline.
- A relatively simple atom optics beamline is based around a highly efficient Zeeman slower designed to match the He* beam properties of the source.
- A simple collimation stage of 2-dimensional molasses immediately after the source maximises the capture of He* atoms in a $\sim$ 1 cm beam.
- A single beam deflects the metastable atoms from the axial path from the source that can be blocked. Obstructing the line-of-sight path from the source reduces the ground state atom beam gas load on the trapping chamber. A flux of 7.5×10^{10} atoms/s is measured at the entrance to the Zeeman slower.
- This beamline delivers a 1 cm He* beam through the Zeeman slower with flux $1.5 \pm 0.5 \times 10^{10}$ atoms/s and brightness 6.7×10^{10} atoms/sr/s measured after the MOT chamber.
- An optimal design of a Zeeman slower reduces the atom beam velocity from 700 m/s to $\sim$ 70 m/s with ~80% efficiency. Nearly 100% of the velocity

distribution entering the Zeeman slower from a LHe cooled source, and $\sim 75\%$ of atoms from a LN_2 cooled source, is below this capture velocity.

- The MOT chamber is located immediately after the Zeeman slower to capture the slowed atoms in the trapping region centred 165 mm after the slower exit.

At just 1.4 m from source to trap centre the LHe cooled beamline is a compact, efficient, easily operable and reliable source of He^* atoms with which to load a magneto-optical trap. This is verified by the trap results examined in the next chapter.

CHAPTER 5

Properties of He* Magneto-Optical Trap

The primary objective of the construction of the compact LHe cooled beamline is to serve as a simple Magneto-Optical Trap (MOT) loading beamline. So it is an important milestone that the high performance of the compact LHe beamline translates into a He* trap equal of the best contemporary experiments, including the ANU's own loaded by the 'bright beam machine [27]. This would vindicate the principles of optimized performance that guided the beamline design.

The motive for this aim is that the MOT is merely the starting point for further experiments. The performance of this trap is important to the performance of trapping chamber used as a Low Velocity Intense Source in Chapter 6. The overall size and temperature of the MOT are likely to affect the basic flux and quality of the LVIS beam. The MOT variations with detuning, intensity and magnetic field gradient will affect the trap loading rate, and hence affect on the performance of the LVIS.

The focus of this chapter, then, is the investigation of the basic properties of the compact LHe beamline loaded MOT with a view to making these comparisons. The first section describes the MOT chamber and the detectors used to collect data about the trapped atom cloud. The second section describes the data collection system, and the third section describes the collection and analysis of information about the atom cloud. The final section discusses the meaning of these results in the contexts of the comparison and expectations to be made.

5.1 Apparatus

The overall assembly of the compact MOT loading beamline is discussed in Sec 4.2, and only those details specific to the magneto-optical trap are discussed in detail here.

The He* MOT chamber layout and apparatus is shown in the schematic in Fig 5.1, and in closer detail in the photo in Fig 5.2. The stainless steel chamber is designed to minimise the separation of the magnetic field coils and hence maximise access to the vacuum system on the strong magnetic field axis, while maximising optical and other access around the weak axes. The chamber is constructed from two re-entrant plates separated by 140 mm either side of a 28 cm diameter cylinder supporting a range of standard half-nipples from 150 to 38 mm in diameter. This includes four spare optical ports as well as optical ports for the radial MOT beams, the vacuum pumping port, and the base port. The base port is capable of mounting an MCP but none was used in the experiments of this thesis. A Pfieffer turbo-pump achieves a 10^{-10} torr base pressure and maintains a few 10^{-9} torr under load with a MOT.

The water cooled magnetic coils are held in aluminium pre-forms in the tight spaces around the strong axis view port. This allows the magnetic coils to be located just 50 mm from the MOT centre. The coils produce an axial field gradient of 41 G/m/A, or 21 G/m/A radially. The strong z axis is orthogonal to the atomic beam x axis entering from the Zeeman slower on the left of Fig 5.1, and the atom beam enters the trapping volume at 45° between the radial plane MOT beams. The Zeeman slower exit feeds directly into the MOT chamber, so to minimise the effect of the Zeeman field in the trap centre a compensation coil is used, mounted off the exit flange of the slower.

The slower laser beam is injected along the x-axis through the trapping volume from the right of the MOT chamber in Fig 5.1. As noted in Chapter 4 the Zeeman slower is a σ^- design such that the slower beam detuning is ~640 MHz below resonance with the trapped atoms.

The MOT itself is a three, retro-reflected beams type. The three beams are derived from a single large ~38 mm beam using 40 mm wave plates and 50 mm mirrors and beam splitting cubes, shown in Fig 5.3. All three beams share the same detuning (-10 to -45 MHz) and size (38 mm diameter), but the relative power balance between the three is controlled by a pair of half wave plate and PBS cube sets. In particular the first set controls the power balance between the axial laser beam and the radial pair of crossed beams. This permits the adjustment of the power balance in proportion to the magnetic field gradients in the axial and radial directions. The relative beam intensities for each configuration is measured individually with the beam size restricted by an iris set with a standard 5 mm rod. The total MOT intensity is about 80 mW/cm^2.

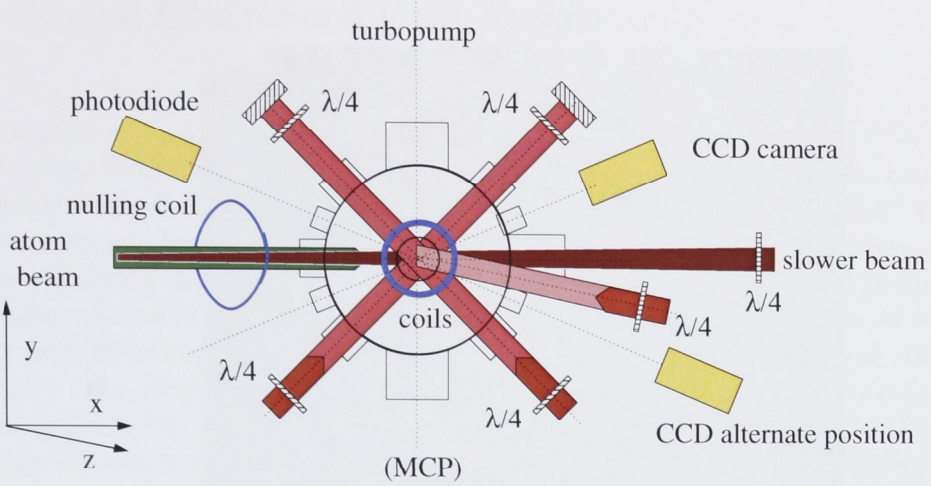

Figure 5.1: A schematic of the MOT chamber located at the end of the compact beamline with the emerging atom beam (green) slowed to trapping velocities by Zeeman slower beam (maroon) in the x-axis. The atoms enter at 45° to the radial beams (red) of a retro-reflected three beam type MOT. The trap chamber is specially constructed so that the magnetic field coils (blue) are as small and close to the centre as possible. The remnant magnetic field of the Zeeman slower is removed by a nulling coil (blue). Auxiliary ports provide access for optical detectors (yellow) as well as an MCP at bottom, although this was not installed.

Two methods of optical detection of the atom cloud are used. A high sensitivity, high gain photodiode measured the number of atoms in the trap by fluorescence, and the size of the atom cloud is measured by imaging on an IR sensitive CCD camera. These are both visible in the schematic and photos in Figs 5.1 and 5.3.

The photodiode is mounted in a 3-axis optical mount including a 25 mm focal length lens. The lens can be adjusted axially for focusing the MOT image on the photodiode, while the photodiode can be adjusted transversely to be located properly in the optical axis. After the photodiode is centred on the optical axis using a collimated beam, the photodiode signal is maximised on the fluorescence signal of the He* MOT itself.

The KP-160 is a CCIR standard CCD camera, running 2:1 interlaced, 625 lines, 50 fields per second, 25 frames per second. The camera can also be run in a non-interlaced external sync mode. In this mode the shutter time and integration period can be controlled by a single digital input signal. At the same time the frame transfer signal has to be synchronised so that the transfer commences a minimum period after the image collection has ceased. This timing of these two signals imposes constraints on the experiment control system. This is discussed in the next section that discusses the automated data acquisition system.

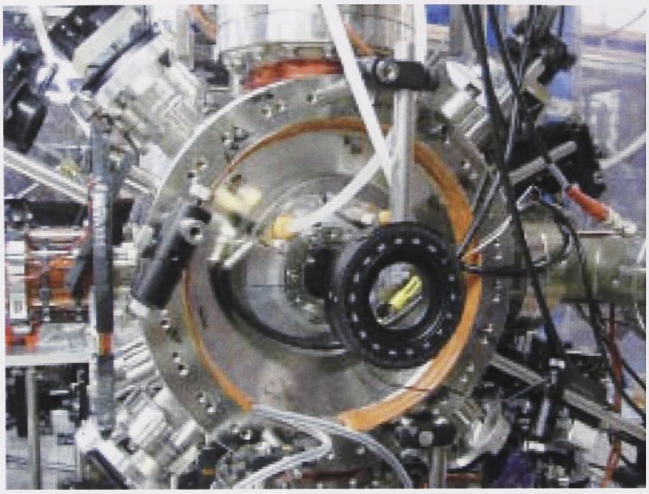

Figure 5.2: MOT chamber close up. The Hitachi camera can just be seen in the lower right corner of the photo in its alternative position opposite the photodiode. The MOT magnetic coil preform can be seen around the transverse optical port. The slower compensation coil can be seen between the the Zeeman slower and the MOT chamber on the left.

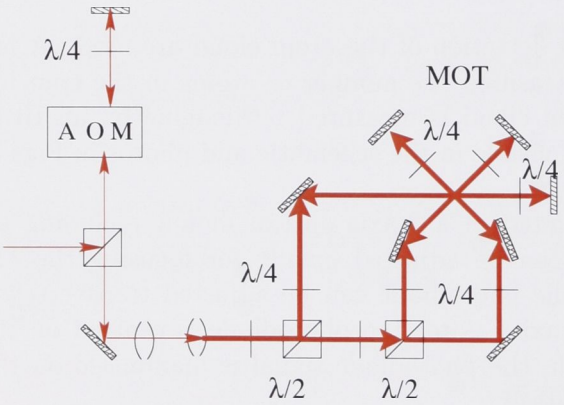

Figure 5.3: Schematic of the optical components in the preparation/production of the three laser beams used in the magneto-optical trap. The trap frequency is tuned by the double passed acousto-optical modulator. The beams are expanded to ~40 mm diameter before split into the three beam configuration using half wave plates and 50 mm polarising beam splitting cubes. In particular the axial beam is separated from the radial pair first, permitting optical power balancing between the axial and radial beams.

5.2 Digital Control and Data Acquisition System

The experiment is operated and observed using a National Instruments PXI RealTime system with 6602 Timing and 6070E Multifunction I/O cards, and a 1409 Image Acquisition card. The RealTime Operating System uses a simplified kernel that bars normal interrupts and can allocate priorities to experimental programs to achieve especially high levels of precision timing of processes. Almost all peripheral tasks after control of the DAQ and control cards are dispensed with, reduced to I/O data communication with the desktop machine via any available protocol (RS232, IP, etc[†].) The RealTime program is composed and executed in Labview from a second desktop PC, whence the DAQ control program is downloaded to the PXI machine for execution. The front panel of the control/DAQ program is displayed on the desktop PC and updates the control values and data displays based on these communications with the PXI/RealTime core module. Importantly the efficiency of this operation will depend on the magnitude of the information transmitted between the two machines, and therefore the period of time for which the RealTime OS pauses data collection. These communications between the control RealTime machine and the remote desktop user-interface are given lower priority than DAQ processes.

Large data transmissions will occur during low priority periods of the DAQ cycle, typically the end/beginning of the major experiment loop where MOT environment parameters are reset to their default values or incremented to their next value. This includes, for example, transmission of the image data from the CCD camera captured by the Image Acquisition card. In some cases, then, it becomes inconvenient for this transmission to occur every cycle. The image can still be displayed shot to shot on the monitor connected to the PXI system, as the RealTime OS can connect the Image Acquisition card to its video card using simple VGA with minimal CPU demand during the DAQ cycle.

This PXI system can control tens of channels with μs accuracy, Fig 5.4. In particular the control signals can be generated with this accuracy to set exposure properties of the CCD camera, such as integration period, trigger time, and synchronise the data retrieval from the CCD camera to the capture card. Together with control of the black and white levels of the capture card and software image mathematics, this data collection system can average and amplify numerical and image data, increasing the signal and decreasing the noise of measurements. The experiment cycle to load, measure and download data is usually 0.5-1.0 s. This allows rapid repetition of experiments to build statistical data. This allows fluorescence imaging of dull MOTs such as when the atom cloud is small, low density or the light fields are far off resonance.

[†]In this case both machines were connected to and communicated with each other via the normal IP network.

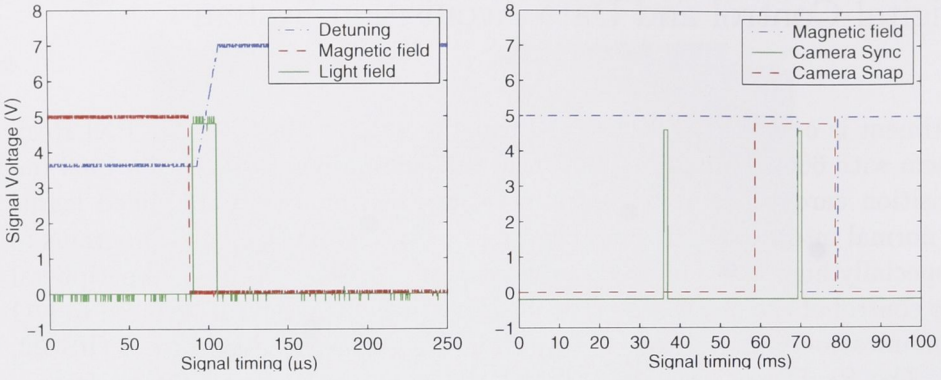

Figure 5.4: Timing control of fluorescence and image collection. Digital-Analog (DA) channel on a 0-10 V scale, Digital I/O channels between zero and five volts.

The DAQ program written in Labview controls both the experiment environment (light field intensities, detunings, magnetic field on/off) and data acquisition from the photodiode (PD) and CCD camera. It systematically records both the programmed control settings and the corresponding raw and processed data (both PD signal and CCD images) for each shot of the experiment using time stamp filenames, and compiles a log of shots for each total experiment at a given set of parameters. For example a single data time record of an experiment can be linked to a summary file of the statistically finished signal/image file and a log file for reanalysis and cross-referencing against the summary result.

Control of MOT parameters

The timing signals for the experiment control of the trap intensity and frequency are shown in the left hand plot of Fig 5.4. In this example two 5 V DIO channels switch the light and magnetic fields on and off, while the laser frequency is set by a 0-10 V input to the AOM generated from a Digital-Analog (DA) channel. The laser amplitude can also be controlled by a DA channel in this way but this is not shown in this example. Note the light field switching is inverted in the AOM control so a 'high' DAQ signal turns the light field off. The signals in this example illustrate a typical fluorescence measurement, where the magnetic field is turned off, as is the light field while the detuning is ramped closer to resonance.

While the temporal accuracy of the DA channels is very high, there are small discrepancies in accuracy and repeatability of their magnitudes. This occurs between the 'internal' magnitudes, both the numerical programmed values and the 'internal' voltages reported from the DA cards, and the output voltages. Typically a given channel would have a small systematic difference for the duration that the PXI ma-

chine is turned on. Since this occurs every time the PXI machine is taken into or out off the RealTime operating system, this is an incentive to develop the software such that this is rarely necessary. The effect can then be limited to individual 'periods of duty', i.e. each day. These channels were used to control the frequency and intensity levels of the AOM drivers, which are not free of systematics themselves. These in turn control the frequency and intensity of the light beams. Therefore in practice it was found more useful to calibrate the initial program values against the ultimate physical values. For intensity that was the intensity of the laser beams measured at the MOT. For frequency the AOM drivers were constantly monitored by external frequency meters.

Accurate knowledge of the MOT beam intensities and detuning is essential both to the controlled, repeatable variation of MOT configuration, and the measurement of trapped atom number from the photodiode signal. In particular the linear relationship between photodiode voltage and atom number can be reduced to a simple coefficient, $N = C \times V$, when the intensity and detuning are known (see Section 2.5.1). These calibrations yielded a coefficient that varied by a maximum 4% between each 'period of duty' of ~15 hours continuous operation.

Photodiode signal: acquisition and processing

The peak atom number measurements were taken after a rapid frequency shift, seen in the left hand plot of Fig 5.4, from the MOT loading detuning to a near resonant detuning (typically ~ -6 MHz) that maximised the photodiode measurement. The voltage signal produced by the photodiode amplifier is collected through an Analog-Digital channel and saved to a file as well as communicated to the desktop display. An example is illustrated in the plot of Fig 5.5, showing the peak in fluorescence measurement before the atom cloud disperses in the near resonant light. Subtracting the background light level from the peak voltage the trapped atom number is calculated live using the calibration based on measurements of the laser field intensities and detunings. The average total intensity was 82 ± 4 mW/cm^2 or $s_0 \sim 400$ where the increased saturation intensity $I_{sat} = 0.2$ mW/cm^2 is used to account for the random re-orientation of Zeeman states in the intense three dimensional molasses of the trap (see Sec 2.5.1, [74].) The display of this number in real time provides immediate feedback for optimisation of the MOT or during studies varying a MOT parameter.

Automatically collected data typically averages twenty experimental cycles for each parameter setting. This usually yields a measurement with an average statistical variation of 0-2%. Occasionally post-processing is required when an individual cycle fails to load the MOT, and the photodiode measurement corresponds to the background only. The reason for this loading failure is that one of the three switched parameters, magnetic field, laser intensity or detuning, has failed to reset to the

correct value in time or at all. Most probably it is the current controller driving the magnetic coils. In these cases short batch process can quickly identify which data sets contain null measurements and recalculate the average of real measurements.

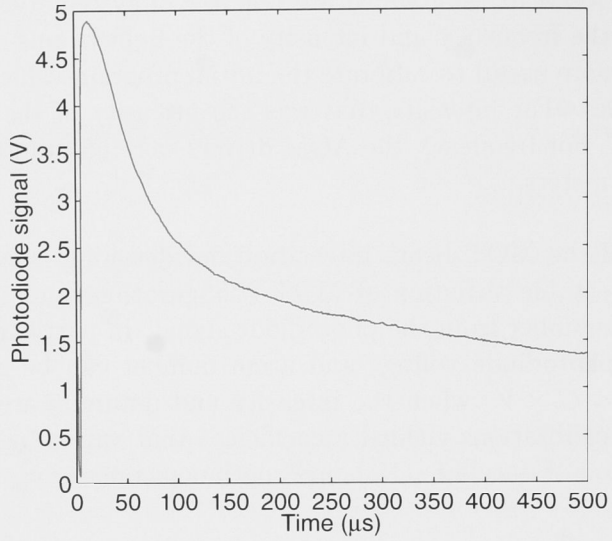

Figure 5.5: A fluorescence signal from the photodiode, taken from a typical file data set.

CCD IMAGE ACQUISITION

The control signals for the CCD camera are shown relative to the magnetic field switch in the right hand plot of Fig 5.4. Two 1 ms signals are required to synchronise the camera for data collection and transmission to the image acquisition card. After the first signal the camera is synchronised to capture an image on the second signal. It can be seen that this signal train commences far in advance of the 'experiment', and in fact this is the leading signal, from which all relative timings must be set. The camera 'snap' signal both sets the integration time and triggers the data download to the capture card. Together an image of fixed integration time can be taken at any time relative to the 'experiment'. The image acquisition cards saves the image to a file and displays the image on the PXI machine monitor for immediate assessment.

The quality of the image can be varied by control of the integration time of the CCD camera and the gain of the image capture card. Images can also be numerically manipulated, so that an average picture can be produced of a sequence of background subtracted individual image shots. All of these parameters can be controlled in software, allowing rapid reconfiguration for optimisation of image collection in each trap setup. This generally allows the collection of good quality images.

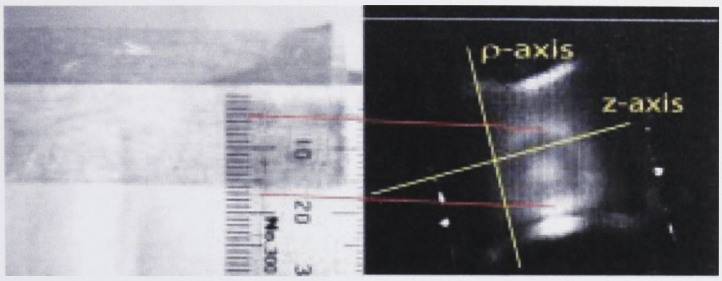

Figure 5.6: A trap image with a scale for comparison. The ring image is the reflection of light on the welding edge of the 15 mm diameter half-nipple behind the MOT. The camera mount is twisted $\sim 30^\circ$ counter-clockwise such that the strong and weak axes are approximately horizontal and vertical respectively.

A trap image is shown in Fig 5.6. Note that the CCD camera mount is twisted $\sim 30^\circ$ counter-clockwise, as seen in Fig 5.6. Behind the trap is a blanked mini-port making a 15 mm diameter dark background that is, however, surrounded by a ring of reflected light. This ring can be partial or complete, depending on image capture parameters. These reflections are dominant in the vertical axis, as seen in this view. Sometimes this causes problems in extracting a measurement of cloud size.

In the 'steady state', the atomic cloud is imaged in the trap at large detunings with a long (10 ms) integration time. In time-of-flight imaging the positions of the atoms after a period of expansion in the dark is 'frozen' by the trapping beams at low detunings, forming an optical 'freezing molasses' in zero magnetic field [118]. The atomic cloud image is collected in a short (1-2 ms) integration time.

CCD IMAGE PROCESSING

The size of the atomic cloud is measured by the density of fluorescence intensity in the CCD image. The CCD camera is located in the xy-plane as shown in Fig 5.1 so that the horizontal and vertical axes correspond to the strong (axial z) and weak (radial ρ) axes of the trap respectively. Assuming that the atomic distribution is Gaussian, each of these images is matched to a 2-D ellipsoid Gaussian shape, characterised by Gaussian radii σ_ρ and σ_z for the weak and the strong axis respectively, and angle of rotation from the image's original frame of reference.

Two algorithms were employed to find the Gaussian radii of the resulting cloud image. A Labview routine optimises two orthogonal line fits, including rotation of the axes, during data collection. This was cross-referenced in post-processing with the results of an IDL routine that fits the cloud with a 2D Gaussian surface. Two examples of the MOT images and their corresponding plots of fit residues from the

2D IDL routine are illustrated in Figs 5.7 and 5.8.

Despite the generally good quality of the image of the MOT itself, the other patches of light interfere with the ability of each of these routines to fit the image to a Gaussian shape. The line fit frequently fails to fit the y-width due to high background signal and the inability of the Labview routine to select a Region-Of-Interest (ROI). In these cases the surface fit routine often successfully retrieves these widths by careful selection of ROI. However the surface fit frequently fails to work at all with images that have too much deviation from a smooth Gaussian surface, e.g. by saturated background speckle in a low intensity image, or insufficient pixel depth between foreground and background, even in an image with a bright MOT. In the best cases both routines generate matching values for both widths and, generally speaking, rotation angles. This gives confidence in the efficacy of both algorithms, such that in those cases where one algorithm is clearly inferior to the other one can select valid data with confidence.

However this difficulty in fitting images is a major source of error in these measurements, measured by the reproducibility of σ_ρ and σ_z from the IDL 2D Gaussian fit. Running the routine on some images, such as Fig 5.7-a, produce radii with $\leq 2\%$ variability, despite the remnant area of scattered light after cropping the image. By comparison other images, such as Fig 5.8-a, are considerably more difficult to fit with confidence, producing $\sim 10\%$ variation in σ_ρ and σ_z.

The widths are converted from pixels to millimetres using the calibration factor 0.0859 ± 0.0004 mm/pixel[†]. This process yields up to four fit results for each image:

- vertical (σ_ρ) and horizontal (σ_z) fits from the Labview linear fit routine;
- similarly vertical (σ_ρ) and horizontal (σ_z) fits from the IDL surface linear fit routine.

From these values four average values can be derived. The Gaussian widths σ_x and σ_y average the two routines in x, y-axes. The width σ_r averages all the measurements for a single image. Finally the width σ_a averages the measurements of all images for the same time-of-flight period. An error $\Delta\sigma$ is calculated for each width that takes account of the pixel calibration error, the fitting error, and the cloud drift in the freezing molasses that was measured as 0.05 mm per millisecond integration time for the image capture. The image size data is tabulated in Tables C.2 to C.9 of Appendix C.

[†]The method for obtaining the pixel calibration has been reinsterted in Appendix B at examiners request.

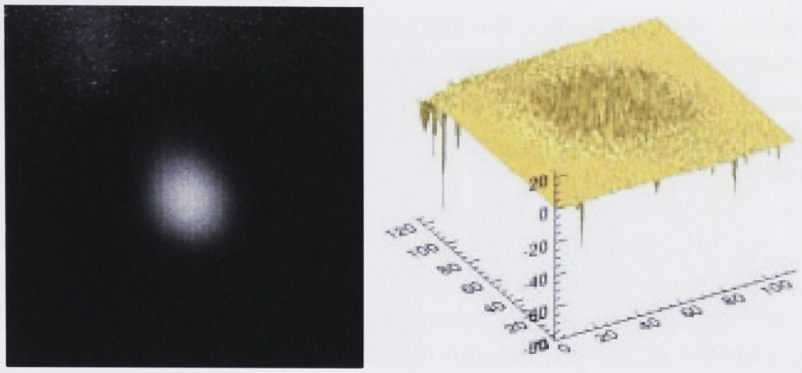

(a) (b)

Figure 5.7: An example of a better quality image of the MOT (a) and the corresponding image of the residues (b) produced by the IDL Gaussian surface fit routine - the scales in pixels are indicated in the x, y axes of the residue plots. The quality of the fit is shown by the small, random residues in the region of the MOT, and the high contrast with the negligible residues across the dark background. The remaining scattered light in the top left-hand corner of the image not excluded by cropping (a) produces substantial residues in the corresponding corner of the residue plot (b). Despite this repeated fits produced $\leq 2\%$ variability in σ_ρ and σ_z.

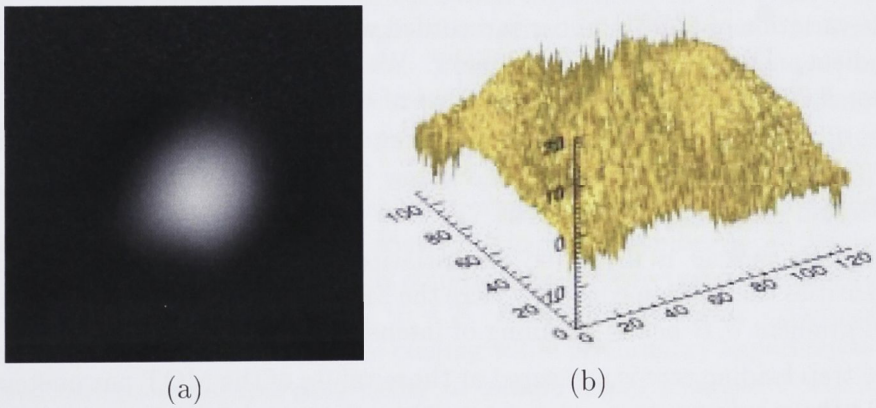

(a) (b)

Figure 5.8: The cropped area of this image of the MOT (a) is approximately, though not exactly, the same area as the image in Fig 5.7-a. However the corresponding plot of fit residues shows a reduced contrast and systematic variations - a concentric peak and trough marking the centre and edge of the MOT and turned down corners. These produce significantly more variation ($\sim 10\%$) in the fit Gaussian radii σ_ρ and σ_z.

5.3 Characterisation of the He* atom cloud

There are two modes of operation of the compact MOT loading He* beamline that are likely to have a significant effect on optimum performance. As seen before in Chapters 3 and 4, cooling the source with liquid helium delivers substantially different and improved operation over liquid nitrogen cooling. It is to be confirmed that this contributes significantly to the loading rate of the trap. There are two principal modes of operation of the trap itself, based on the relative optical power balance between the axial and radial axis of the MOT magnetic coils. The two main options are a balance of equal powers (referred to as EPB) or of equal light forces. The latter may be expected to produce a more symmetrical, round MOT (RMOT). The question is whether it also traps more atoms?

5.3.1 Measurements of the He* Magneto-Optical Trap

There are three MOT parameters, detuning, intensity and magnetic field gradient, for determining the optimum trapping environment. After preliminary resolution of this question a detailed study of the MOT parameter space is based on measurement of atom number data with variation of intensity and magnetic field gradient at each of eight MOT detunings from -10 MHz to -45 MHz in 5 MHz intervals:

1. The variation of MOT number is recorded while scanning of the magnetic field gradient, using maximum light power. We determine the magnetic field gradient $\partial_z \vec{B}$ which maximises the number of trapped atoms, $N_{max} = N(\partial_z \vec{B}_{opt})$, then measure the $\partial_z \vec{B}_{opt}$ variation between half this maximum number, above $[N(\partial_z \vec{B} > \partial_z \vec{B}_{opt}) = \frac{1}{2} N_{max}]$ and below $[N(\partial_z \vec{B} < \partial_z \vec{B}_{opt}) = \frac{1}{2} N_{max}]$ the optimum magnetic field gradient.
2. The trap number is measured for variation in intensity across the range of intensities that we can control [†]. Here the MOT size was optimised by intensity and gradient $\partial_z \vec{B}$ before scanning of intensity.
3. The trap loading rate is measured at those values of the MOT parameters that yield the maximum trapped atom number, the trap loading rate is measured.
4. A number of CCD images are collected for each MOT setting for which number data is collected. The trapped cloud size is captured in a 'steady state' image with a long (10 ms) integration time. For time-of-flight measurement of the cloud temperature the atoms are released from the trap to drift in the dark for a period before capture and imaging in freezing molasses. A series of images captured at increasing delays up to 5 ms after the atom cloud has been released from the trap.

[†]Because the AOM efficiency varies with frequency, the range is not necessarily the same for all detunings.

The parameter values for each measurement are manually and automatically logged for cross checking together with such post-processing of the photodiode signal, Fig 5.5, as required [†]

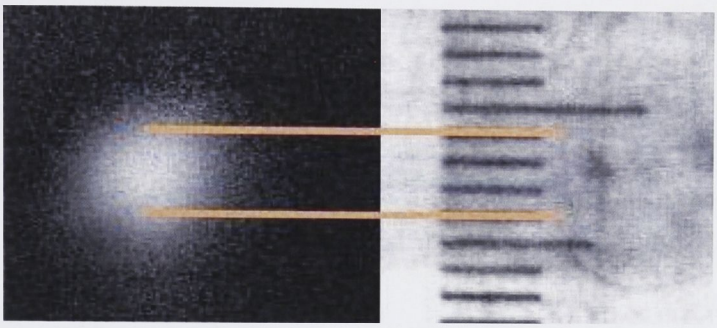

Figure 5.9: A (cropped) MOT image alongside a ruler, with a 2σ diameter estimate at 3-4mm.

5.3.2 Maximum atom number

The peak number results for variation of detuning are compared in Figures 5.10 and 5.11 for the two variable modes of operation introduced in Sec 5.3.1: source cooling and MOT power balance. Clearly the optimum detuning, at -30 MHz, is independent of these variations of mode. This is to be expected, as each mode change has an impact on the anisotropic rate of transfer of atoms from the beam to the trap, but no effect on overall isotropic trapping potential.

The first Figure 5.10 demonstrates the improvement in trapped atom numbers achieved by extra cooling of the He^* source. The total number is $\sim 2\times$ larger with LHe cooling than LN_2 cooling. This confirms the improvement in performance through cooling the source from 80 K to 4 K. Hence the optimum experimental results can be achieved with LHe source cooling while preliminary experiments can be performed using the cheaper and easier to handle liquid nitrogen in the same apparatus.

The second Figure 5.11 shows a further improvement in maximum number, achieved by adjustment of the relative laser power between the axial and radial axes of the MOT magnetic coils. Redistributing the optical power, with the axial beam ~60% that of the radial beams, makes a closer balance in the light forces. This produced a more symmetrical, round MOT cloud (the RMOT,) compared in Fig 5.11 with the equal power balance (EPB) configuration. The total number is consistently $2-3\times$

[†]The errors in Figures 5.10 to 5.13 are up to 15% of peak value. This estimate has been attribtued to the reproducibility of the detuning ramp used to measure the atom number [2].

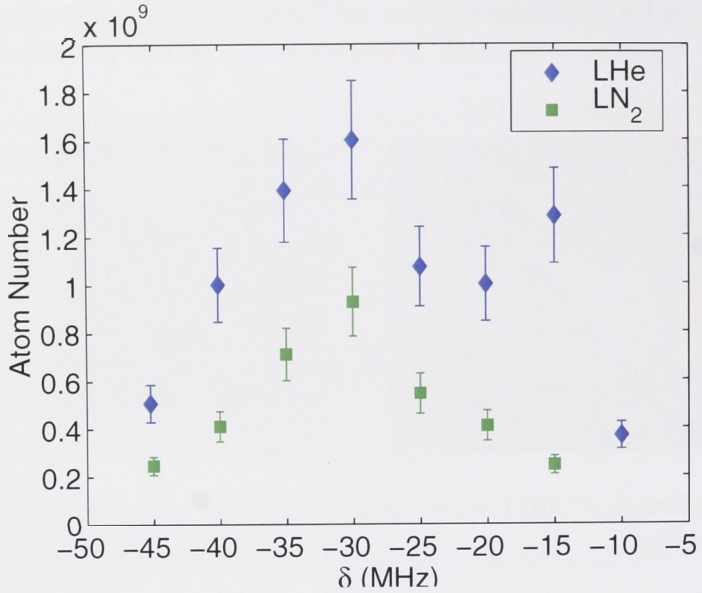

Figure 5.10: Variation of the peak trapped atom number with MOT detuning, changing the He* source cooling between LHe mode ($\diamond$) and LN_2 mode ($\square$). The MOT light fields are in equal power balanced (EPB) mode in both cases.

larger, consistent with having proportionately more power in those beams that help slow the atom beam entering the trapping region.

The overall result is a trapped number $3-4\times$ larger with the RMOT loaded from a LHe cooled source. The maximum number of $2.7 \pm 0.3 \times 10^9$ atoms was achieved in a LHe cooled RMOT configuration at a detuning $\delta = -30MHz$ and axial gradient $\partial B = 8.7$ G/cm. Compared with other traps (Table 1.1) we are able to create one of the largest He* MOTs yet measured.

$-\delta$	(MHz)	10	15	20	25	30	35	40	45
N_{max}	(10^9 atom)	0.65	0.78	1.0	1.4	2.7	2.0	1.7	1.5
ΔN	(10^9 atom)	0.07	0.08	0.1	0.1	0.3	0.2	0.2	0.2
I	I_{sat}	430	480	400	450	130	340	250	230
∂B	(G/cm)	7.4	6.6	4.1	6.6	8.7	9.6	16.2	20.7

Table 5.1: Peak MOT sizes: for each MOT detuning the maximum trapped number is given together with the intensity I and magnetic field gradient ∂B settings at which it was attained in the RMOT configuration.

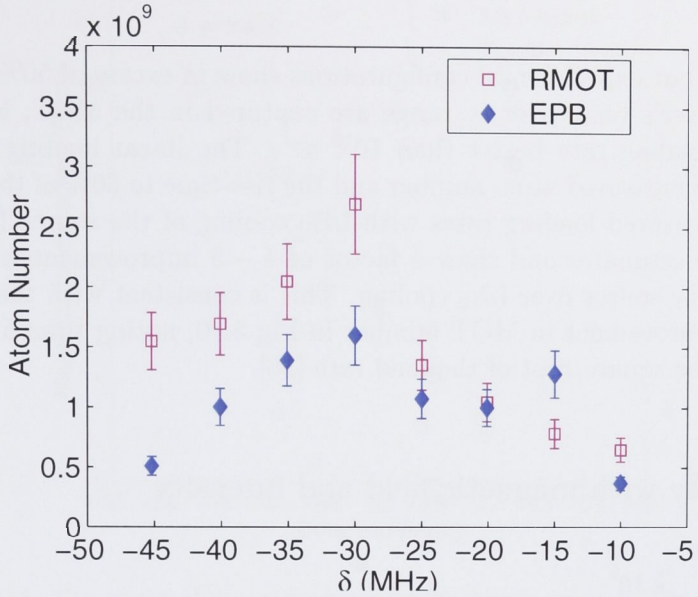

Figure 5.11: Variation of the peak trapped atom number with MOT detuning for the two data sets with equal light force (RMOT - □) versus equal power balancing (EPB - ◇). The He* source cooling is in LHe mode in both cases.

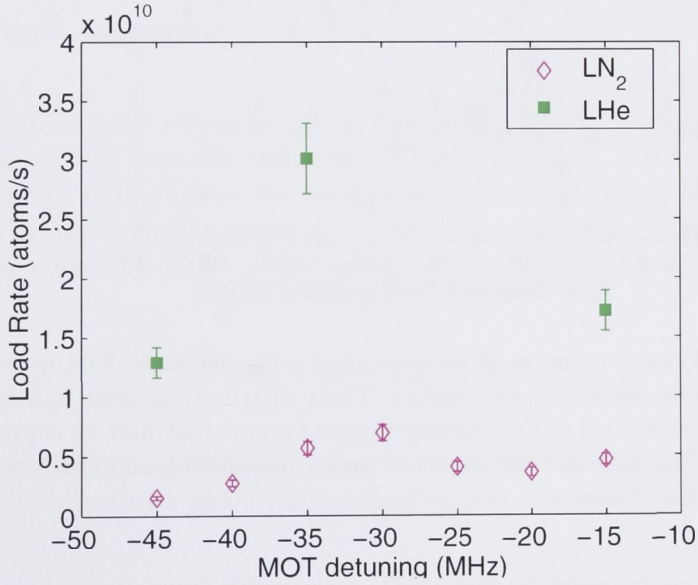

Figure 5.12: The linear loading rates are calculated from the measured rise-time to 60% of the maximum photodiode signal.

The simulations of our experimental configurations show in excess of 50% of atoms in the Zeeman slower's final velocity range are captured in the MOT, leading us to expect a LHe loading rate better than 10^{10} s^{-1}. The linear loading rates are calculated from the measured atom number and the rise-time to 60% of the number maximum. The measured loading rates with LHe cooling of the source (Fig 5.12) both confirm these estimates and show a factor of $4 - 5$ improvement with liquid helium cooling of the source over LN_2 cooling. This is consistent with the approximately two fold improvement in MOT number in Fig 5.10, noting than final MOT number scales as the square root of the load rate [16].

5.3.3 Variability with magnetic field and intensity

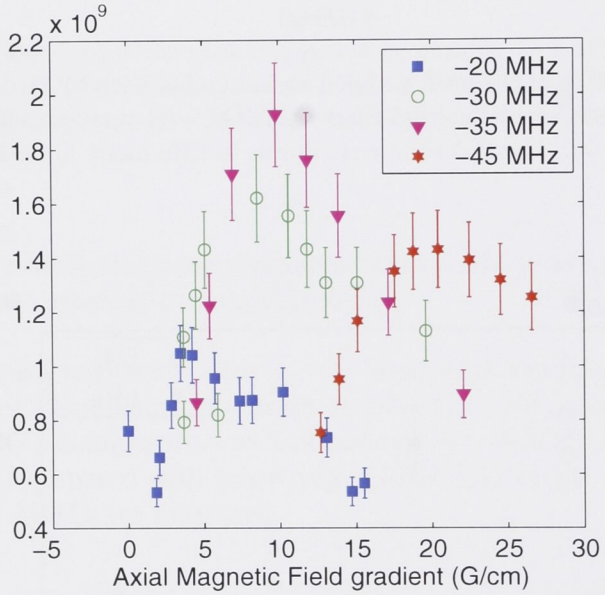

Figure 5.13: Typical maxima of atom number with magnetic field gradient (only four profiles are shown for clarity). These distributions with $\partial_z \vec{B}$ show the typical width related to the velocity range of atoms that may be captured by the MOT. This includes the effects of power broadening and the Doppler width of the atom beam.

The number of atoms trapped by the MOT varies with laser power and trapping magnetic field. At larger detunings a 'stiffer' trap with more laser power and stronger trapping gradients is required to prevent the loss of high energy atoms. The results of the measurements taken by methods (§5.3.1 - 1) and (§5.3.1 - 2) are shown in Figures 5.13 and 5.14, and 5.15 respectively.

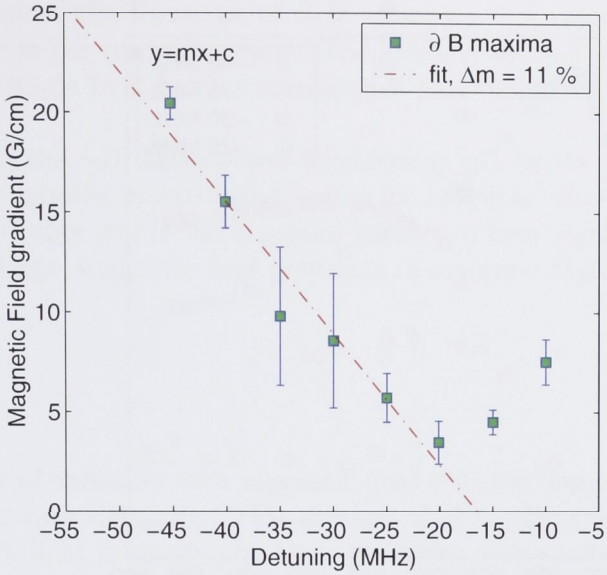

Figure 5.14: The peaks of the magnetic field gradient curves in Fig 5.13 for all measured detunings (§5.3.1 - 1). The plotted error bars are estimated from the width at 95% of $\partial_z \vec{B}$ peak value. Within these errors there is a good linear relationship consistent with Eq 5.4 below -15 MHz. Above this the probable cause of the displacement is power broadening, which at 10 MHz will heat instead of cool as significant fraction of the atoms in the MOT capture region.

Magnetic Field Gradient

The plot of atom number versus magnetic field gradient (Fig 5.13) shows the measured variation of four separate detunings. These illustrate two features, a clear optimum magnetic field gradient for each detuning, and the displacement of these maxima to higher gradients for larger detunings. The ~15 MHz FWHM $\Delta\delta$ of these peaks varies by only 10% across all detunings. From the resonant detuning

$$\delta = \delta_L + kv - \mu' B(z)/\hbar, \tag{5.1}$$

the width $\Delta\delta$ is the sum of the power broadening of the MOT laser fields and the Doppler width of the atomic beam exiting the Zeeman slower (neglecting the smaller Zeeman width)

$$\Delta\delta_{\pm} = \Delta\delta_L + \vec{k} \cdot \Delta\vec{v}. \tag{5.2}$$

The 10 m/s FWHM of the Zeeman slower velocity profile corresponds to a Doppler

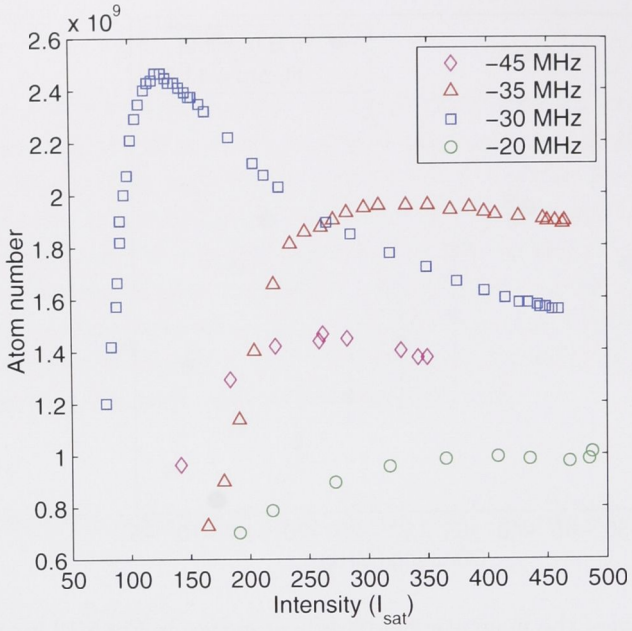

Figure 5.15: Typical saturation of trapped atom number with the increase in optical power (only selected profiles are shown for clarity.) The maximum power available is frequency dependent due to the AOM efficiency. Errors are estimated at 10%.

width of 6.5 MHz, accounting for the 45° intersection between the atomic and laser beams. This is power broadened at $\sim 50\ I_{sat}$ by ~10 MHz, giving a total of 16.5 MHz in agreement within experimental variation.

The peaks in Fig 5.13 show a distinct displacement toward higher axial magnetic field gradients with larger detuning. The peak $\partial_z \vec{B}$ are plotted for those and the other measured detunings in Fig 5.14. The data above 15 MHz shows a reasonable linearity that may be related to the atomic motion within the region of over-damped motion in the MOT [72]. In this region the frequency shifts in Eq 5.1 are small and $\frac{\mu B}{\hbar} \sim kv \sim \delta_0$ within the limits of a 'capture velocity' $v_{capture}$ and corresponding 'capture radius' $r_{capture}$. Then the spontaneous force can be rewritten for a damped harmonic oscillator [72]:

$$\vec{F} = -\beta\vec{v} - \kappa\vec{x}. \tag{5.3}$$

Then for a given intensity, with $kv = kv_{capture} =$ constant, and Eq 5.1 reduces to

$$\delta_L \propto \frac{\mu}{\hbar}\, \partial_z \vec{B} r_{capture}. \tag{5.4}$$

Hence the gradient of the linear fit of $\partial_z \vec{B}$ versus δ_L can supply the size of the over-damped zone in the trapping region. The gradient of the linear fit in Fig 5.14, in units of kHz·m/G, is 15 ± 2. This corresponds to a radius 9 ± 1 mm.

At small detuning the ~10 MHz power broadening will be the cause of a disproportionately large number of scattering events for atoms at very low velocities and Doppler shifts. In other words the trapping lasers will heat significant numbers of atoms, requiring larger magnetic field gradients to maintain higher trap potentials.

Intensity

The measurement of variation with magnetic field gradient was conducted at maximum intensity at each detuning. This assumes that trapping efficiency increases monotonicaly with light intensity. At high intensities atoms entering the trapping region can be heated just as easily as cooled and those with velocities closest to the MOT capture velocity may be scattered instead of trapped.

Ultimately optimum performance in capturing atoms in the trap is a 'mode-matching' exercise between the properties of the atom beam exiting the Zeeman slower and the trapping region dynamics. At a fixed intensity and ∂B, variations in detuning affect the rate of Zeeman slowing in the trapping region, limiting the uppermost loading velocity that that can be captured by the trapping region.

These crude assumptions are abandoned in the second experiment §5.3.1 - 2 that measures the captured atom number with intensity, after first explicitly optimising the trapping number with intensity and magnetic field gradient. In some cases the optimum trapping configuration is at significantly less than the maximum intensity available at a given detuning [†].

The plot of atom number versus intensity of the trapping lasers (Fig 5.15) shows the measured variation of just four detunings of §5.3.1 - 2 for clarity. These illustrate the expected increase in trapped number for a trapping force proportional to intensity [72],

$$F_{spon} \propto \frac{I}{I + c} \tag{5.5}$$

Such a force saturates for $I \gg c \simeq (2I_s\delta/\gamma)^2$, and this is clearly seen in the atom number, which apart from the -30 MHz result increases with more power to some limit that is roughly maintained until maximum available power is reached.

The -30 MHz detuning shows the effect of optimum mode-matching with the Zeeman slower - the trapped number increases to a significantly higher maximum at a power

[†]As noted above, the AOM efficiency varies with frequency so that maximum intensity is not the same for all detunings.

(110-120 I_{sat}) significantly lower than the saturation levels of other detunings. This indicates that this configuration is especially effective at further slowing the atom beam as well as capturing and storing atoms in the trap.

Furthermore at still higher intensities fewer atoms are captured at this frequency than at -35 MHz, as seen also in Figure 5.14. This shows how optimisation of two variables is insufficient given the complex three dimensional dynamics of the trap.

In the experiments §5.3.1 - 1 and §5.3.1 - 2 the magnetic field gradient was independently optimised. This raises the question of whether the optimal value was used for each method. However the same magnetic field gradient used for the data in the data in Figures 5.10, 5.11 and 5.13 within the width at 95% of $\partial_z \vec{B}$ peak.

5.3.4 Volume, Density and Temperature

δ -MHz	σ_z mm	σ_ρ mm	V cm^3	N_{max} 10^9	n_0 $10^{10}cm^{-3}$
-10	0.72	1.09	0.013±0.003	0.71	5.3±1.6
-15	1.26	1.30	0.03±0.01	0.86	2.6±1.2
-20	1.11	1.03	0.019±0.001	1.15	6.2±1.0
-25	2.06	1.84	0.11±0.02	1.49	1.4±0.4
-30	1.79	1.66	0.08±0.01	2.96	3.8±1.0
-35	1.90	2.14	0.14±0.01	2.24	1.6±0.3
-40	1.76	1.59	0.07±0.01	1.86	2.6±0.8
-45	1.74	1.41	0.05±0.01	1.70	3.1±1.0

Table 5.2: Volume measurements and the calculated atom densities.

Table 5.2 provides the average Gaussian radii σ_ρ and σ_z derived from steady state MOT images. The Gaussian volume, which contains 68% of the atoms, is obtained from the the widths by $V = (2\pi)^{3/2}\sigma_\rho^2\sigma_z$. This volume conveniently connects the central density n_0 and the known trap numbers by $N = n_0 V$. The densities for each detuning are shown in Table 5.2, with an average value of $3.4 \pm 1 \times 10^{10}$ cm^{-3}. This value is considered high compared to the apparent limit due to Penning ionisation limit experience in other laboratories, although densities of 10^{10} cm^{-3} have been quoted [119].

The radius data at eight MOT detunings is recorded in Tables C.2 to C.9 for each image collected for free flight periods up to five milliseconds. These may be analysed using the time-of-flight relationship to obtain the cloud temperature from the gradient of Eq 2.40, making systematic errors negligible. The experiment changes one parameter, the time-of-flight period t_{tof}, and measures the variance of one

other, σ_i, the atomic cloud radius. The error in the final value of a such compound measurement can be reduced by the statistical contribution of many individual measurements by regression analysis (see Appendix D) [97].

Given the MOT symmetry at each detuning these images four values of the cloud temperature can be obtained in the strong (z) axis, the weak (ρ) axis, radially 'symmetric' and averaged over all images. This analysis provided 24 values of the temperature in a range 0.1-0.5 mK range with typical $\Delta T = 0.1$ mK. This value is generally considered unreasonably low compared with the typical measurements (~ 1 mK) of the He* community in Table 1.1.

Both the measurement and the analysis of the atomic cloud radii has withstood multiple degeneracies in methods, so that there can be no doubt in the data in Tables C.2 to C.9. In order to change the gradient of Eq 2.40 substantially the actual drift period t_{act} must be multiplicatively in error of the time-of-flight period: $t_{act} = f \times t_{tof}$. The gradient, and hence the temperature, would then be in error by a factor $1/f^2$. Since the experiment was dismantled and relocated within days of this data collection, it is not easily repeatable, and the reassembled compact beamline has proceeded with the next steps toward BEC. Therefore this data is not reported further.

5.4 Conclusion

This chapter reports on the performance of the compact beamline loaded magneto-optical trap:

- Large atom clouds ($\sim 10^9$ atoms) are achievable over a wide range of detunings, intensities and magnetic field gradients.
- This corresponds with high loading rates, over 10^9 atoms/s with liquid nitrogen and over 10^{10} atoms/s with liquid helium.
- The maximum number of $2.7 \pm 0.3 \times 10^9$ atoms in a Gaussian volume 0.08 ± 0.01 cm^3 was achieved in a LHe cooled equal light force (RMOT) configuration at a detuning $\delta = -30MHz$ and axial gradient $\partial B = 8.7$ G/cm, with typical variation about these optimum values.
- Liquid helium cooling contributes to a significant increase ($\sim 2\times$) in trap size over LN_2 source cooling consistent with $\sim 4\times$ higher loading rates.
- Balanced light forces contribute to a significant increase ($2-3\times$) in trap size over equal power balanced MOT laser beams.

- The capture of nearly 100% of atoms from the compact beamline into a large He^* MOT verifies the expectations of MOT loading performance of the compact beamline from Chapter 4 as an efficient MOT loading beamline.

This large MOT cloud, captured with the maximum efficiency from the compact LHe beamline, provides sound base for conversion into a high intensity, low velocity atom source of He^* atoms.

CHAPTER 6

The He* Low Velocity Intense Source

The magneto-optical trap has become the standard starting point for contemporary experiments in atom optics, especially the formation of Bose Einstein Condensates. This creates a need for a simple, reliable MOT loading apparatus. The Low Velocity Intense Source (LVIS) is a case in point, making a small modification of a standard MOT apparatus to form the source for a high quality atomic beam. In the previous chapters the emphasis has been on constructing the next generation of standard atom optical components to build up the compact He* MOT loading beamline. This has proved itself a reliable source of large He* atom clouds. This is the best possible start for the production of a Low Velocity Intense Source of metastable helium atoms, the subject of this chapter.

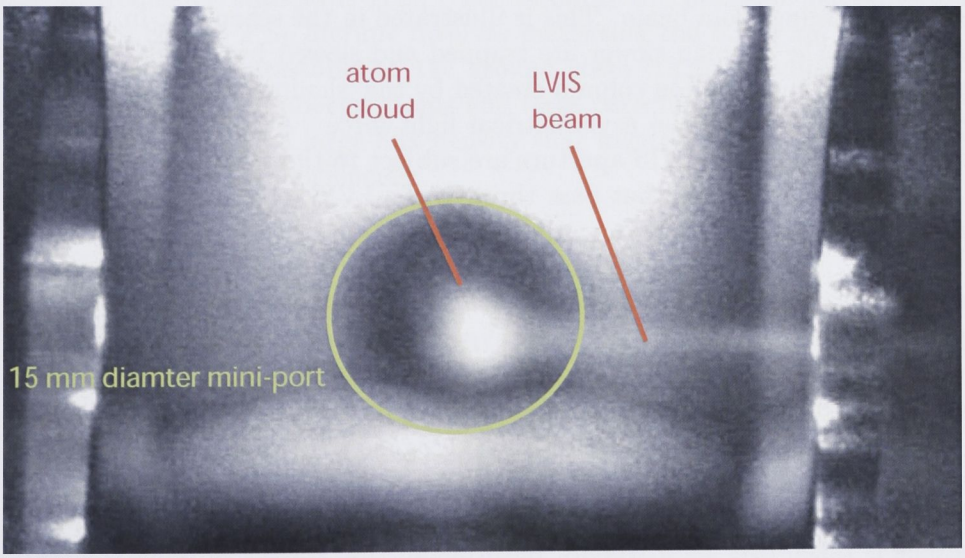

Figure 6.1: The trapped atom cloud is converted into a He* source with a simple optic modification, producing a beam sufficiently intense to fluoresce.

6.1 The He* LVIS Experiment

The bright, slow He* beam developed here uses a method similar to that of Lu *et al.* who coined 'Low Velocity Intense Source' or LVIS to describe their apparatus that converted a standard MOT into a reservoir for an intense and slow atom beam [36]. The large variety of techniques developed for efficiently ejecting atoms from a trapped atom cloud into a well collimated atom beam were examined in Sec 1.6. The essence of the technique in Reference [36] is simple: a narrow centre of one beam of the MOT is blocked, creating an extraction column in which atoms experience an asymmetrical optical force and are pushed from the trap centre into a beam.

A practical design of a He* LVIS, that is one that takes advantage of the electronic detection of the metastable state and where the dense slow He* beam can be used in a subsequent experiment in a vacuum chamber separate from the MOT, requires a single retro-reflected MOT beam on the LVIS axis. An electronic detector or vacuum chamber aperture would block the path of a two-beam MOT light field on this axis, as seen previously when measuring the flux through the Zeeman slower in the compact beamline in Sec 4.3. Hence the He* LVIS is simple modification of a standard three beam magneto-optical trap as in Lu *et al.*.

The special *in vacuo* LVIS optic is made by penetrating one of the retro-optics (quarter wave plate and mirror pair) with a small hole. No light is retro-reflected at the hole, creating the 'dark' extraction column. The aperture also geometrically collimates the emerging atom beam. This is illustrated in the schematic in Fig 6.3. The atoms exiting the Zeeman slower are trapped and slowed by the MOT fields. When atoms enter the extraction column created by the 'shadow' of the LVIS aperture they are accelerated by the asymmetrical light force. Atoms that leave the extraction column before the LVIS aperture are subject to the trapping forces, and recycled into the MOT. Atoms that pass through the LVIS aperture make up the LVIS beam.

One disadvantage of this apparatus is that He* atoms are always coupled to the MOT light, as there is no dark state due to hyperfine splitting unlike other atomic species which have been used to demonstrate MOT based beams. This is true even after the LVIS optic, potentially further accelerating and heating the atom beam. The second configuration in Figure 6.5 is designed to overcome this fault and minimize the leakage of MOT light into the LVIS beam vacuum chamber. With the centre of the MOT beam blocked, the extraction column is dark. The acceleration duty of atoms is taken over by a second 'push-beam' that passes through the trap centre to the LVIS optic just above the aperture. This combination of LVIS and push-beam designs we call the 'LVIS$^+$'.

For the experiments studying the LVIS/LVIS$^+$ beams reported in this chapter the

short LVIS beamline composed two instruments to analyse the LVIS beam, a wire scanner and the MCP/phosphor (Fig 6.3). In the ACQAO BEC experiment these are to be replaced by the second trapping chamber where a second MOT will capture the atoms for transfer into the magnetic trap for condensation.

The use of the He* LVIS/LVIS$^+$ as a highly collimated, intense beam of low energy atoms to be captured in a magnetic trap or second MOT creates three objectives:

1. Delivery of a substantial flux of He* atoms together with large differential pumping between the BEC chamber and the MOT chamber, where the background pressure of 5×10^{-9} torr is too high for condensation.

2. Low beam velocities permit smaller diameter laser beams as the slowing distance scales as the square of the capture velocity. Hence LVIS velocities 1/2 the Zeeman beam velocity of 70 m/s will allow laser beams diameters one quarter the 38 mm required in the MOT in Chapter 5.

3. Low divergence of the atoms maximises the capture in a small trapping volume, permitting the magnetic coils to be separated by a small gap. As a result a tight confining magnetic trap is possible with only a few amp-turns required.

Other applications require a low divergence, high flux beam for maximum measurement signal-to-noise. These include atomic and molecular spectroscopy [89, 120] and atom frequency standards [121]. For example the precision measurement of the helium $\sim$ 8000 s 2^3S_1 lifetime involves measuring the 62.55 nm photons from the decay from the metastable to the ground state [122]. Maximising signal-to-noise requires a large number of atoms and large detector solid angle. A high flux, low velocity beam offers a large flux density that together with the low divergence promises high collection efficiencies.

6.1.1 The LVIS optic

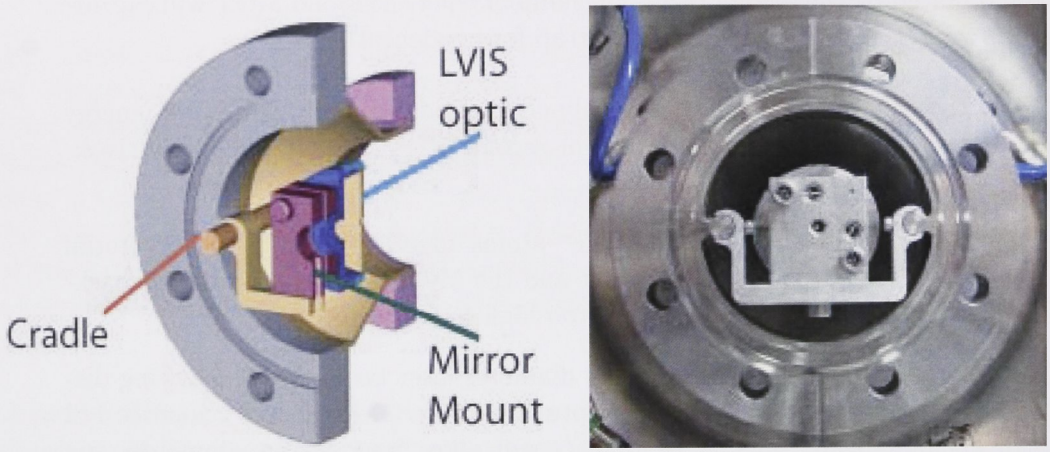

Figure 6.2: A schematic and photograph of the LVIS optic and mount. A standard *in vacuo* adjustable mirror mount is attached to a cradle that slides on tow rods for adjustment of the LVIS-MOT separation. The aperture in the LVIS optic is visible with the back lighting in the photograph.

Our LVIS optic is a single piece retro-optic is made by drilling and mirror-coating one face of a 30 mm wave plate with 1083 nm anti-reflective surface coatings. One surface is coated by gold vapour deposition. Gold is an excellent reflector of both S and P polarisations at the 1083 nm wavelength.

A diamond drill bit was used to successfully drill a 1.5 mm hole in the centre of the wave plate. Drilling all the way through the wave plate produced chips to occur on the exit face. These scatter light around the hole which is detrimental to the performance of the LVIS. A good finish with minimal chipping was produced by drilling the hole from one side of the optic to the center and repeating the process from the other side.

The result, seen in the schematic and photo in Fig 6.2, is a single piece LVIS optic which is mounted in an adapted 1 inch *in vacuo* mirror mount, supported on a cross-bar cradle between two rails on which the MOT centre to LVIS optic separation L_{sep} (Fig 6.3) is simply adjusted. The full extent of travel on the rails is 30 mm, positioning the LVIS optic at L_{sep} from 42 to 72 mm from the trap centre. The retro-reflection mirror alignment of the MOT beam is adjusted with the mirror mount sprung screws. A micrometer is used to maintain the relative parallelity and the cross-bar can be locked to each rail with grub screws.

The mount is reset in minutes once the vacuum chamber is let up to atmospheric pressure with nitrogen and exposed for adjustment. After locking the cradle at each separation the retro-reflected beam is fine tuned with the insertion optics. Once

closed the vacuum chamber pumps down overnight, with some additional baking, to typical MOT vacuum pressures.

6.1.2 The He* LVIS

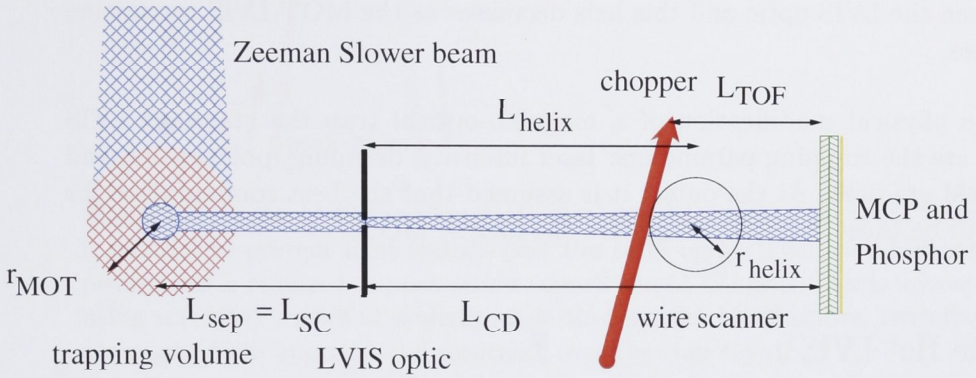

Figure 6.3: He* LVIS beamline showing the atom beam entering the trapping region perpendicular to the LVIS geometry. Major dimensions are indicated: for experiments, the LVIS optic - MOT separation L_{sep}, distance to and radius of the helix scanner, and the time-of-flight drift length. Calculating the geometrical collimation by the LVIS optic the key length are the 'source' to 'collimator' distance (using Ramsey's notation [70]) $L_{SC} = L_{sep}$ and the collimator - detector separation L_{CD}.

The magneto-optical trap is transformed into an LVIS with the installation of the LVIS optic. The schematic of the LVIS beamline in Figure 6.3 shows the major features of the LVIS apparatus. The cylindrical shape of the MOT chamber (visible in Fig 5.2) was designed to facilitate the extension in the atom beamline perpendicular to the Zeeman slower axis. This allows for significant differential pumping achieving a reduction of approximately 1000 in the partial pressure of helium in the BEC chamber, satisfying objective 1 in Sec 6.1.

Initially, in order to maximize the probability of detecting the LVIS current, the LVIS optic was installed at the closest separation L_{sep} from the MOT centre[†]. A 16 cm long vacuum cross-chamber supports the detectors for these experiments shown in Figure 6.3. The main detector was the MCP/phosphor screen at the end of this drift length. Since the total distance separating the MOT centre and the MCP plane is constant, the distance to the detector from the collimating LVIS aperture L_{CD} decreases as the MOT-LVIS separation L_{sep} increases. A horizontal laser beam parallel to the Zeeman slower axis pushes the LVIS flux off the MCP a

[†]This length is equivalent to the source-collimator length L_{SC} in Ramsey's notation [70] employed to calculate the theoretical divergence in Sec 6.2.5

constant distance L_{TOF} before the MCP. This beam acts as a 'chopper' for time-of-flight measurement of the beam velocity.

A helical wire scanner rotating about the perpendicular axis measures the two dimensional profile of the atom beam. Each orthogonal 1-dimensional scan occurs in a different plane along the LVIS axis, at distances $\pm r_{helix}$ to the location of the rotation axis. Again, the location of the rotational feed-through is fixed, so the length L_{helix} between the LVIS optic and this axis decreases as the MOT-LVIS separation L_{sep} increases.

As a simple physical modification of a magneto-optical trap the standard LVIS parameters are the trapping parameters: laser intensity, detuning, polarisation and magnetic field gradient. At the outset it is assumed that the best configuration for the LVIS will be those values that capture the largest MOT.

6.1.3 The He* LVIS$^+$

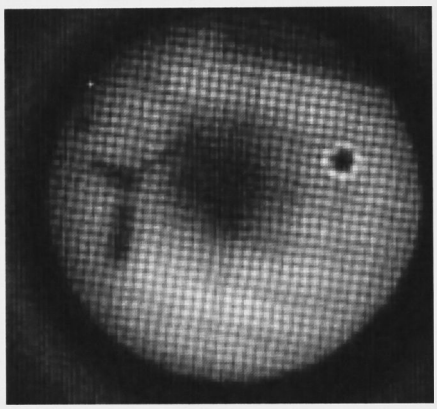

Figure 6.4: Imaging the LVIS beam: the atomic beam is clearly seen to be lighting up most of the 22 mm MCP imaging area (note the protective mesh shadow). Although there are some defects in the MCP and phosphor such as the ring of saturated channels in the upper right quadrant, the LVIS beam is very clearly seen to be hollow, and this spot could be directed around the imaging area by tuning of the MOT wave plates or the MOT beam mirror.

A draw back of the LVIS configuration is the collinear alignment of the retro-reflecting MOT light fields means the laser light which passes through the hole in the centre of the LVIS optic is exactly on axis with the atomic beam. The He* atom has no hyperfine splitting of the ground-state, and hence no dark state. Therefore a He* atom is constantly coupled to the MOT light, and continuing scattering of photons heats the atomic beam. This heating was so severe in the LVIS that the beam was observed to have a dark centre (Fig.6.4) not previously seen with

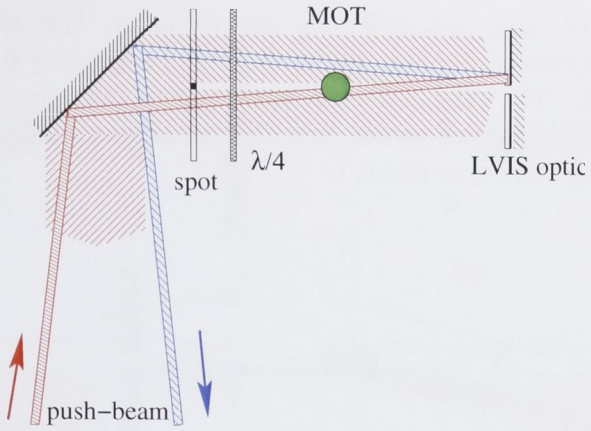

Figure 6.5: In the LVIS$^+$ configuration the central 1.5 mm of the MOT beam is blocked to prevent light leakage past the LVIS optic. Then an additional push-beam is required to push atoms toward the LVIS optic. This is injected using the MOT optics at a slight angle through the MOT centre, reflecting above the LVIS aperture and returning over the trap cloud.

alkali experiments, where the transverse temperature of the beam is several orders of magnitude lower than the He* MOT temperature [36]. The hollow region proved independent of MOT detuning and power balancing, although it could be 'steered' by small changes in the wave plates of the radial MOT beams or small changes in the injection angle of the light field on the LVIS axis.

The LVIS$^+$ is a further modification of the LVIS apparatus, principally 'fine-tuning' the LVIS light fields, as shown in Fig 6.5. The MOT beam co-propagating with the atom beam is blocked using a ~1.5 mm dark spot on an AR coated window inserted into the input beam (Fig 6.5). The shadows of the spot and aperture are overlapped in the retro-reflected beam such that the LVIS$^+$ extraction column is 'empty' of ingoing and reflected light.

After diffractive refilling by the 38 mm MOT beam this reduced the light intensity transmitted through the LVIS optic by a factor of almost five to 14 μW or 5 I_{sat}. At the peak MOT detuning of -30 MHz this is still sufficient for atoms to scatter about 20 photons in the $\sim$ 10 ms journey from the LVIS optic to the MCP detector.

While the transmitted light is reduced in this configuration this also means that there is minimal light pressure pushing atoms out of the centre of the magneto-optical trap toward the LVIS aperture. An additional laser beam is introduced to replace this function, the 'push-beam', making the 'LVIS$^+$'. A slightly focused beam, inserted via the final input orientation mirror for the MOT beam, passes through the trapping region with a 1/e radius of 0.75 mm at the MOT centre, as illustrated in Fig. 6.5. The push-beam does not pass through the LVIS aperture

but reflects off the LVIS optic just above the central hole. This makes it unlike the push-beam experiments of Section 1.6 as there is no guiding function of the beam after acceleration. The retro-reflected beam passes over the MOT with no significant interaction with trapped atoms, and allows continuous monitoring of the push-beam power during the experiment.

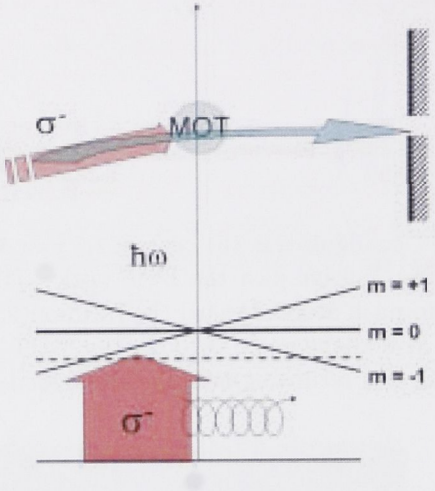

Figure 6.6: Atoms in the push-beam with a trapping polarisation experience a stronger acceleration upstream of the trap (in this case to the left) - the principle of a MOT.

The atomic beam is now accelerated out of the MOT along the LVIS$^+$ push-beam. The optical parameters of the LVIS$^+$ push-beam that extracts atoms into the atom beam are totally independent of those of the MOT that load atoms into the extraction-column/push-beam. This doubles the number of parameters for optimisation of the LVIS$^+$. The peak acceleration is a product of the rate of optical pumping - hence directly in proportion to the laser field intensity and moderated by the coupling co-efficients of the magnetic sub-states with the light field polarisation. The relationship with intensity is expected to be direct and straightforward - increased flux on the LVIS$^+$ beam for increased laser beam intensity. For polarisation the story is more complicated - including the polarisation standing-wave in the region of overlap with the collinear MOT beam.

In Reference [36] Lu *et al.* note that for the standard LVIS the MOT configuration with circularly polarised light causes the atoms to feel a stronger acceleration upstream of the trap centre than on the downstream side, Fig 6.6. This creates a difference in the acceleration experienced by atoms entering the extraction column upstream or downstream of the trap centre, leading to a wide spread in velocities [36]. An elliptical polarisation made the acceleration weaker but more balanced (Fig 6.7-a) leading to a smaller velocity spread. Increasing ellipticity of the MOT beam decreased the LVIS flux because the trap capture rate decreased.

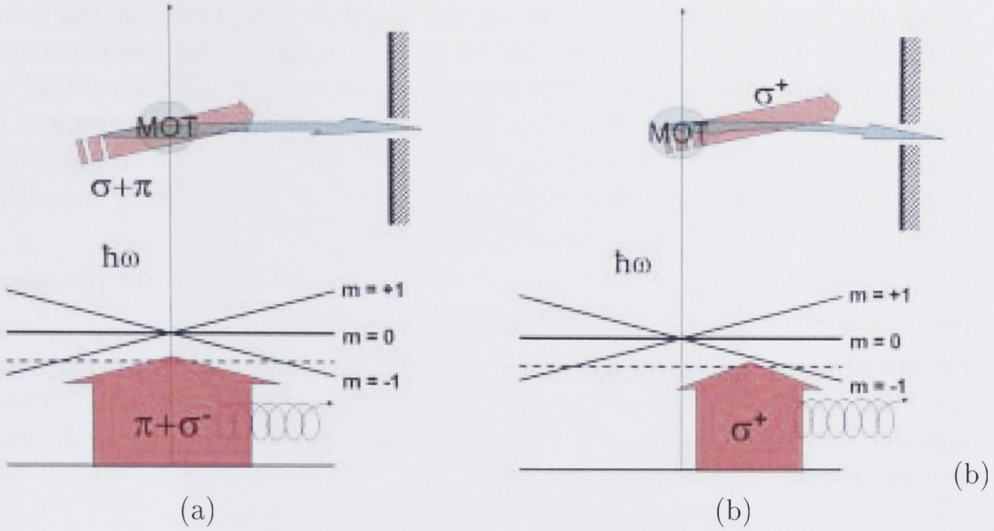

Figure 6.7: The push-beam polarisation, independent of the MOT polarisation, can vary through elliptical/linear polarisation (a) and anti-trapping polarisation (b). In an elliptical polarisation (a) the acceleration, although weaker, is nearly equal upstream and downstream. In an anti-trapping polarisation (b) the acceleration is stronger downstream (here to the right) of the MOT centre.

In the LVIS$^+$ the push-beam polarisation pushing the atoms into the beam is totally independent from the MOT polarisation trapping atoms. This means the polarisation can be varied from trapping circular polarisation through elliptic polarisation to anti-trapping circular polarisation. In an anti-trapping circular polarisation atoms will experience a stronger acceleration downstream of the trap centre, Fig 6.7-b. In general we can anticipate strongest effect and sharpest changes in σ polarisation parallel and anti-parallel to the MOT beam polarisation, and weaker effect and slow changes with elliptic polarisation.

6.1.4 Detecting the He* beam

The short LVIS beamline supports two detectors that provide measurements of the LVIS/LVIS$^+$ beam flux, divergence and velocity to investigate objectives 2 and 3 in Sec 6.1.

The primary means of detecting the He* beam is a Multi-Channel Plate and phosphor screen detector mounted directly in the beam path after ~12 cm drift distance from the collimating aperture of the LVIS optic. This detector can be connected in different configurations, as applied above in Section 4.3, in order to extract a variety of measurements:

1. Given the intensity of the LVIS beam the stainless steel mesh on the front of the MCP (visible in Fig 6.9) can be used to measure the beam current directly using a picoammeter. This mesh has a known transparency (50%) so that while the beam size is less than the mesh diameter this measurement is related directly to the beam flux. In its operating mode this mesh is connected to a bias voltage to repel ions attracted by the high voltage away from the MCP so that we detect only neutral atoms.
2. In its standard operating mode the He* beam can be imaged on the phosphor plate. This image is captured with a CCD camera.
3. Instead of biasing the phosphor plate for imaging it can collect charge from the MCP stack, hence amplifying the beam signal by the MCP gain. Then a charge sensitive amplifier can provide a measurable voltage with high time and signal resolution[†].

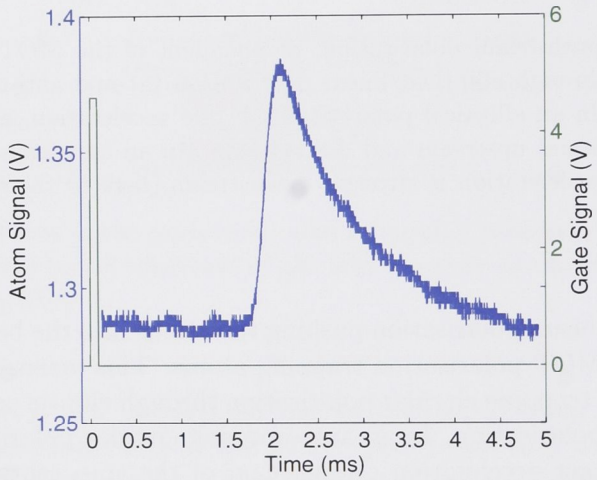

Figure 6.8: An example of the LVIS time-of-flight data collected by the MCP/phosphor with a digital CRO, with a 100 μs gate signal controlling the chopper beam (an high signal means the beam is off).

Combined with a transverse laser beam upstream to chop the LVIS beam this data collection mode can collect Time of Flight (TOF) data for measuring the LVIS beam velocity, Fig 6.8. A 3 mm laser beam is sufficient to break 80% of LVIS beam current. This optical chopper 4.5 cm before the MCP is switched off by an AOM for a few hundred microseconds to allow through a pulse of atoms. The $I(t)dt$ signal is converted to the $P(v)dv$ distribution identically as in Chapters 3 and 4.

Using the MCP in these modes we can measure the flux, size and velocity of the LVIS beam. However given the narrow range of MCP gain available and the intensity of

[†]A warning: this is a dangerous mode of operation, with the possibility of *in vacuo* discharge between the biased MCP and proximate grounded phosphor plates.

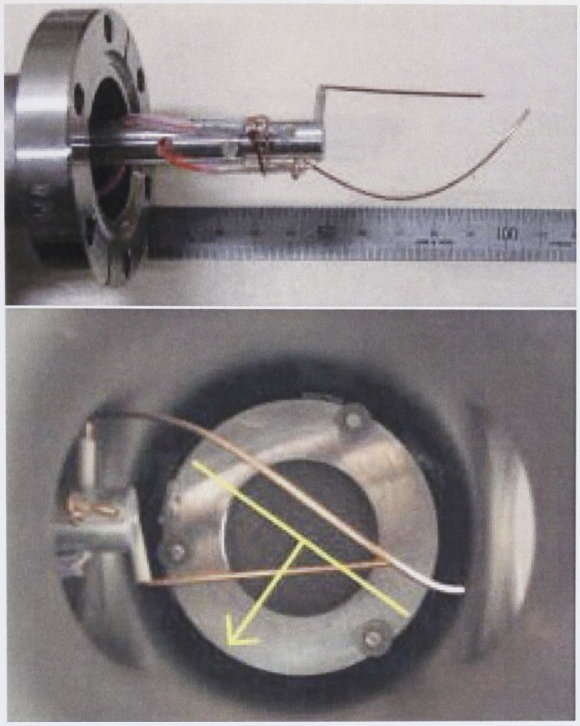

Figure 6.9: Helical wire detector, shown against a ruler for scale and in the orientation as seen by the LVIS beam. Here in the forward plane the wire at an angle 135° from x-axis scans across the 45° axis, and vice versa in the rear plane. In the MCP view these angles are reversed. A second wire attracts electrons, or the roles can be exchanged for a linear scan.

the atomic beam, images of the beam tend to suffer from saturation effects so that only the most basic estimate of divergence can be made from CCD images (see for example Fig 6.18). For this reason a second helical detector is employed to measure the beam profile.

Automated helical beam profile monitors such as the NEC Model BPM-80 [123] are commonplace in nuclear physics, since the error compared to linear translation detectors is minimal and operation is hugely simplified. As the helix is rotated the projection of the helix onto the transverse plane sweeps across the beam axis as a straight line (at 45° to the axis of the rotational mount), first in one axis then in the orthogonal axis. Each sweep occurs in a different plane, one forward, one rear of the axis of the rotational mount, at the radius of the helix. In this case (Fig. 6.9) the helix was manufactured by winding copper around a pre-form in a helix with a 30° pitch making the 45° angle to the rotational angle. The deviation from a linear probe of a 15 mm diameter, 30^0 pitch helix is insignificant to ~ 5 mm increasing to 5% at 10 mm radius. A second wire attracts electrons, or the roles can be exchanged for a linear scan.

6.2 Characterizing the slow, bright He* beam

Initial testing of the LVIS, with a LN_2 MOT loading rate of 6.6×10^{10} atoms/s captured a flux of 1.5×10^9 atoms/s. Immediately the He* LVIS is comparable with the highest flux sources in Table 1.2. This is prior to a detailed study of the LVIS variability or realising its full potential in terms of the objectives expressed in Section 6.1. These first tests suggested that higher LVIS currents were available at higher magnetic field gradients than the optimum gradient for large traps in Chapter 5. Further enhancement of the beam properties are expected in the LVIS$^+$ configuration, including the dependence on push-beam polarisation. Therefore we consider the performance of the LVIS/LVIS$^+$ as relates to

1. magnetic field gradient,
2. push-beam polarisation,
3. flux,
4. divergence and
5. velocity

6.2.1 Magnetic Field Gradient

In Section 5.3.3 it was found that the optimum magnetic field gradient for large clouds of atoms trapped in the MOT was a current of 21 A in the magnetic coils producing $\partial_z \vec{B}$ of 8.5 G/cm. The first trials of the LVIS suggested that significantly higher beam currents were available at higher magnetic field gradients than this optimum for trapping. A thirty percent gain in flux could be achieved at 12 G/cm, as shown in the LVIS data at 42 mm in Figure 6.10.

This optimum magnetic field gradient for LVIS trapping was investigated more closely for the LVIS$^+$ at larger MOT-LVIS separations, also plotted in Fig 6.10. The result is a maximum in LVIS$^+$ flux at a relatively constant magnetic field gradient ($\sim$30 A $\equiv$ 12 G/cm) in each case. Extrapolating this data with a Gaussian fit the width derived ($\sim$10 A $\equiv$ 4 G/cm) is also relatively constant for each separation.

At each value of MOT $\partial_z \vec{B}$ the beam flux was optimised with MOT detuning and the Zeeman slower magnetic field for a constant push-beam configuration. In each case optimisation of the Zeeman slower provided no further improvement in LVIS$^+$ flux. However the maximum flux was a product of optimum pair $(\delta_{opt}, \partial_z \vec{B}_{opt})$ of MOT detuning and magnetic field gradient. The pairs corresponding to the data in Fig 6.10 are plotted in Figure 6.11. In concordance with our findings for the

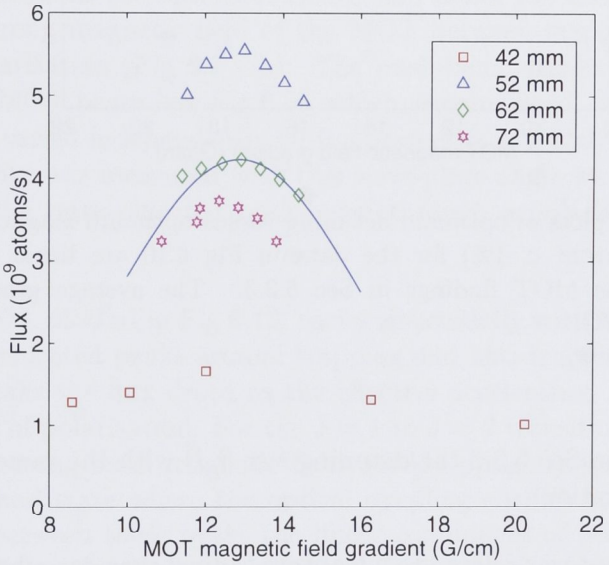

Figure 6.10: The LVIS (L_{sep}=42 mm) and LVIS$^+$ (L_{sep}=52, 62, 72 mm, errors $< 1\%$) flux showed a clear maximum with magnetic field gradient centred at 12 G/cm, higher than the 8.5 G/cm for maximum MOT size. At each $\partial_z \vec{B}$ the maximum flux was found by variation of MOT detuning. An approximate peak width (4 G/cm) was found by extrapolating with a Gaussian fit (example shown).

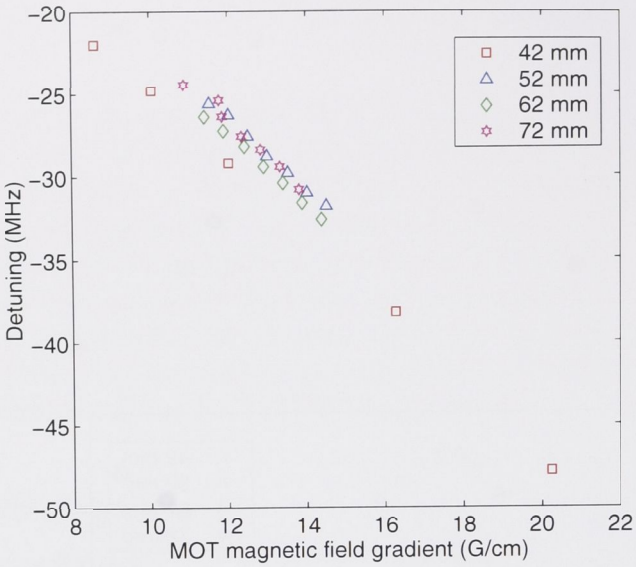

Figure 6.11: The plots of optimum detuning versus optimum magnetic field gradient (both errors $< 1\%$) for the data in Fig 6.10 are linear in concordance with the MOT findings in Sec 5.3.3. The average gradient is 21.7 ± 0.5 kHz·m/G.

magneto-optical trap in Sec 5.3.3 the detuning $\delta \propto \partial_z \vec{B}$ with the same gradient for each MOT-LVIS separation.

In Sec 5.3.3 this gradient was related to a 'capture radius' that describes the volume of over-damped motion in the trapping region [72]. The average gradient of this line, in units of kHz·m/G, is 21.7 ± 0.5 (compared to 14.4 ± 1.6 for the MOT). This is the same for all four LVIS separations within the error ($<10\%$) of the gradient fit. This gradient converts into a capture radius of 13.6 ± 0.3 mm for the LVIS, compared to 9 ± 1 mm for the MOT.

Why is this radius larger? Inherent in the LVIS/LVIS$^+$ geometry the flux of atoms passing through the LVIS optic aperture is dependent on the collimation of atoms within the extraction column. Atoms with large transverse velocities that leave the extraction column before the aperture re-enter the MOT trapping fields and are recycled back into the trap. This larger volume of over-damped motion means that atoms approaching the LVIS extraction column spend longer periods in the retarding force of the optical molasses and are slowed to lower longitudinal and transverse velocities. With proportionally more atoms with low initial divergence the LVIS/LVIS$^+$ flux is higher. Detunings higher or lower than the optimum detuning in Fig 6.10 would decrease the amount of slowing, hence increasing the divergence of the LVIS/LVIS$^+$ beam and decreasing the flux (Sec 5.3.2). However the trapping efficiency of the MOT field, which can be infered from the MOT loading rate in

Fig 5.12, decreases as the magnetic field gradient moves away from that optimum for a large MOT. Hence the data in Fig 6.10 is the result of mode-matching between loading atoms into the extraction column/push-beam and accelerating those atoms into the LVIS/LVIS$^+$ beam.

6.2.2 LVIS$^+$ push-beam polarisation

The flux and velocity of the LVIS$^+$ beam are expected to vary with the polarisation of the push-beam as the optical coupling, and hence the effective acceleration, changes in the strong magnetic field of the MOT between trapping (Fig 6.6) and anti-trapping polarisation (Fig 6.7 - b). The push-beam passes through the final $\lambda/4$ plate for the MOT beam (see Fig 6.5), which remains fixed. The polarisation of the push-beam is varied independently with a preceding $\lambda/2$ plate. The variation of current and velocity was measured with this wave-plate angle while also measuring the intensity of the retro-reflected push-beam through a polarising beam-splitter cube.

The LVIS$^+$ flux ($\diamond$), plotted in Fig 6.12, varies sinusoidally with the push-beam polarisation, with saturated peaks around trapping and anti-trapping configurations. Between these peaks the flux drops as the effective acceleration is reduced by the linear component of polarisation. For the J = 1 to J = 2 transition in helium σ polarisation in the strong axial magnetic field quickly optically pumps the atom to the $m = \pm 1$ ground state where the optical coupling coefficient is one, as shown in Sec 2.2.5. In between these peaks the linear component of polarisation reduces the coupling coefficient, as discussed in Sec 2.2.6, and the acceleration is weaker. In addition, as noted by Lu *et al.* this reduced acceleration is more equal each side of the trap centre (Fig 6.7 - a).

The LVIS$^+$ peak velocity ($\square$) and peak FWHM ($\diamond$) are plotted in Fig 6.13 with principal features 'out of phase' with those of the flux. Both the velocity and velocity width are at a minimum with circular polarisation, while at a maximum for linear polarisation, the opposite result from the original LVIS [36].

There Lu *et al.* argued that the elliptical polarisation $< 20°$ sufficiently equalised the acceleration each side of the MOT that all atoms were accelerated to near the same (smaller) velocity, resulting in a narrower spread. Outside $\sim 20°$ this is overwhelmed by the acceleration over longer distances as the spatial size of the MOT increased in the elliptical MOT beam.

Here the MOT capture rate and the MOT size are unaltered as the MOT beam polarisation is independent of that of the push-beam and constant. We assume that it is the second factor, different distances for acceleration, that dominates. Taking the ansatz for the reduced saturation factor from Sec 2.2.6, the reduced effective

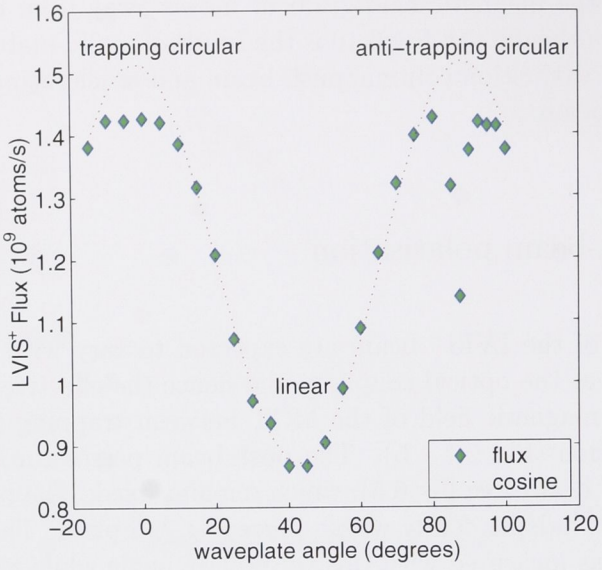

Figure 6.12: The variation of the LVIS$^+$ flux ($\diamond$, errors $< 1\%$) with push-beam polarisation is nearly sinusoidal (shown) with flattened tops in trapping and anti-trapping σ polarisations, and a sharp decrease in the anti-trapping configuration where the MOT beam and push-beam oppose one another.

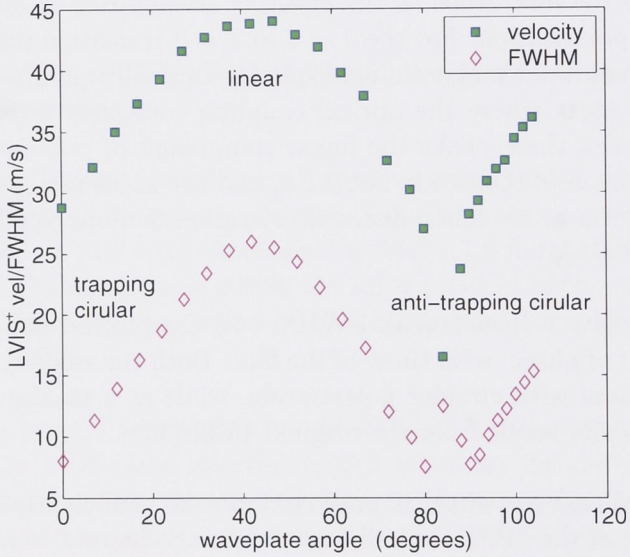

Figure 6.13: The LVIS$^+$ peak velocity ($\square$) and FWHM width ($\diamond$) similarly vary with the push-beam polarisation, but 'out of phase' with the flux. Deceleration of atoms by the MOT beam in the anti-trapping configuration produces a sharp decrease in velocity, while alternating acceleration and deceleration randomly broadens the velocity width. The error in peak velocity is estimated as $\sigma = 1/2.36$ FWHM.

acceleration with linear polarisation is ~80% of the maximum acceleration with circular polarisation. The difference in acceleration lengths can be estimated by kinematics for the velocities in Fig 6.13. Irrespective of the actual acceleration then the linear polarisation acceleration length is ~2.5 times that for circular polarisation. The difference in velocity spread ($\diamond$ in Fig 6.13) is then explained in terms of the initial starting position of atoms in the push-beam.

Both the LVIS$^+$ flux, velocity and velocity width exhibits dramatic behaviour in the anti-trapping configuration. There is a sharp decrease in flux at at the peak's centre, with corresponding with a decrease in velocity while the width simultaneously increases, combining in an almost 3$\times$ increase in fractional velocity width from 0.28 to 0.75.

The simplest reason for this is just the reduced overlap between the atom cloud (Fig 6.1) and the region of optimum acceleration downstream in the push-beam (RHS of Fig 6.7 - b). In addition atoms entering the extraction column downstream from the MOT will have a velocity predominantly opposite to the acceleration. Those entering the extraction column upstream, although the acceleration experienced in here is negligible, are nonetheless travelling toward the region of optimum acceleration. Furthermore atoms that exit the extraction column are prepared in the magnetic substate for the strongest deceleration by the MOT laser beam. In concert the effect is a weaker total acceleration resulting in a lower overall velocity, hence more atoms lsot from the LVIS$^+$ beam, while the wide ranges of inital locations and velocities produces the largest fractional velocity width.

6.2.3 LVIS and LVIS$^+$ Flux

The LVIS and LVIS$^+$ flux variation with the detuning of the light pushing the atoms out of the trap is plotted in Fig 6.14, showing the same peak shape for different magnetic field gradients.

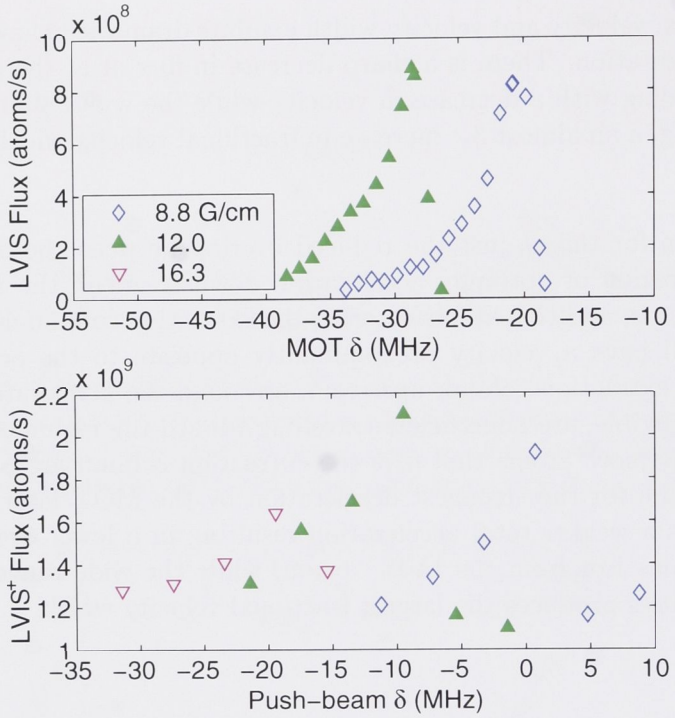

Figure 6.14: Plots of the LVIS flux (upper) and LVIS$^+$ flux (lower) for different magnetic field gradients at $L_{sep} = 42$ mm. These show the peak shape with detuning of the MOT beam or push-beam respectively. The flux data (error $\sim 1\%$) demonstrates the expected detuning shifts with $\partial_z \vec{B}$ and peak width with the power broadened linewidth.

In both configurations the atom flux is higher at $\partial_z \vec{B} \sim 12$ G/cm ($\triangle$) than at the optimum magnetic field gradient for forming a MOT ($\diamond$ - 8.5 G/cm) as discussed in Sec 6.2.1, although the gains of 4% and 9% for the LVIS and LVIS$^+$ respectively in Fig 6.14 are not as significant as seen in Fig 6.10. All the data demonstrates the expected shifts with $\partial_z \vec{B}$ for the coefficient 2.17 MHz·cm/G found in Sec 6.2.1.

The peaked form can be understood qualitatively in terms of the acceleration due the atom-light interaction, as a 'Zeeman accelerator'. Atoms that are tuned into resonance by their velocity Doppler shift and the trap Zeeman shift are accelerated by the light beam, either the MOT beam for the LVIS or the push-beam in the LVIS$^+$. Atoms accelerated to a sufficiently high axial velocity before their trans-

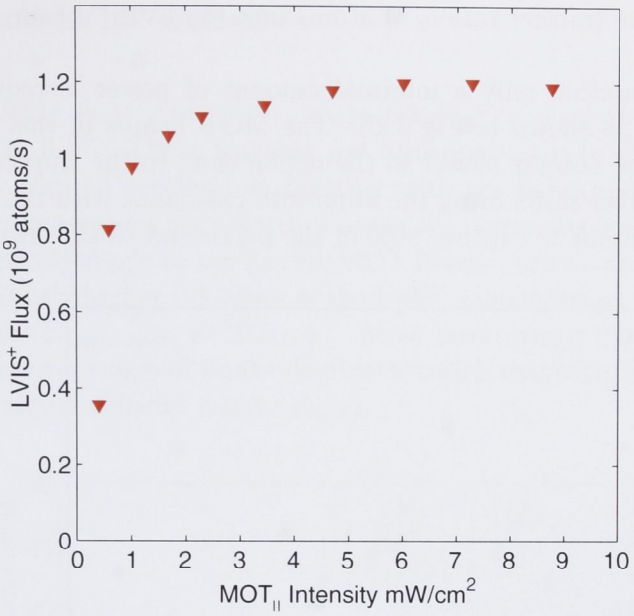

Figure 6.15: The LVIS$^+$ flux requires only minimal power in the parallel MOT beams at -30 MHz to confine atoms in that part of the extraction column where the atoms are in resonance with the -11 MHz push-beam due to their Zeeman and Doppler shifts.

verse velocity takes them out of the extraction column are likely to transfer into the LVIS/LVIS$^+$ beam. Otherwise atoms are recycled into the trap (see Sec 1.6.1 or [36]). The frequency width of the data then should be the order of the power broadened linewidth γ' of the accelerating beam.

For the LVIS data in Fig 6.14 the MOT beam intensity is 12 I_{sat} and power broadened linewidth $3.6\gamma \sim 6$ MHz. This corresponds well with the FWHM of the LVIS peaks, especially considering the asymmetrical shape. The LVIS$^+$ peaks appear truncated in a similar way, while having a power broadened width, although the data does not extend far enough to estimate the FWHM properly. Still this is consistent with a power broadened width greater than 20 MHz produced by a LVIS$^+$ push-beam intensity $I \gg 200 I_{sat}$.

The LVIS beam flux F is related to the MOT loading rate R and collision loss rate r_c by $F = R/(1 + r_c/r_t)$, where r_t is the transfer rate of atoms into the beam [36]. For the LVIS$^+$ configuration, where the MOT loading rate R is a constant with fixed MOT parameters, the variation of flux is a direct sign of the changing transfer rate r_t. Then the LVIS$^+$ data in Fig 6.14 is indicative of mode matching the loading performance of the MOT with the extraction performance of the push-beam. The loading rate R with MOT parameters (-30 MHz, 12 G/cm) is maximised for capturing atoms in the extraction column/push-beam, while the push-beam detuning

10 MHz maximises the transfer rate r_t of atoms into the LVIS$^+$ beam.

In the LVIS$^+$ configuration only a minimal amount of power is required in the parallel MOT beams as shown in Fig 6.15. The MOT beams in this axis confine the atom flux from the Zeeman slower to the region close to the trap centre, where the Zeeman and Doppler shifts bring the atom into resonance with the push-beam. Just a few I_{sat} is sufficient to capture 90% of the maximum LVIS$^+$ flux.

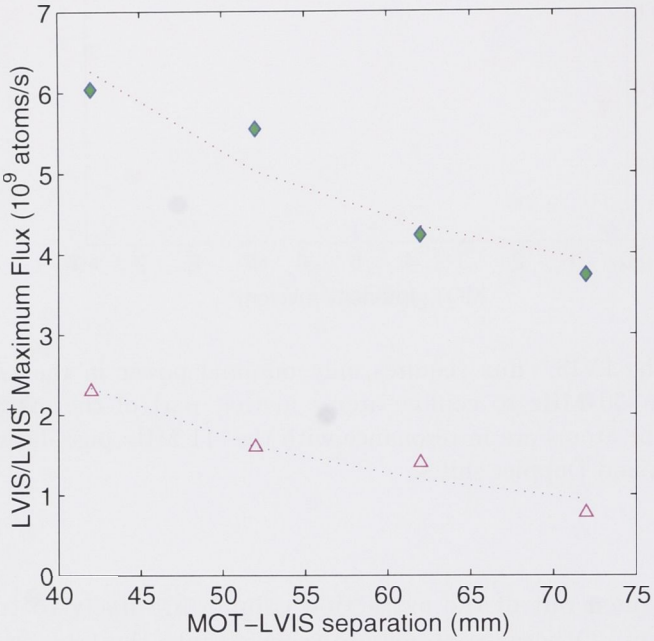

Figure 6.16: The atom flux (error $\sim$ 1%) of the LVIS ($\triangle$) and LVIS$^+$ ($\diamond$) decline with the expected inverse square relationship with the collimation distance, the MOT-LVIS separation L_{sep}, shown by the plotted fits to the data, within the reproducibility of experiments.

The flux as a function of the collimation distance L_{sep} is plotted in Fig 6.16 for the both the LVIS and LVIS$^+$. The data reasonably follows the expected proportionality with $1/L_{sep}^2$ (see Sec 3.1.1), with some variability probably due to the reproducibility of experiments after venting the chamber to change the collimation distance.

The maximum LVIS$^+$ flux recorded was 6.0×10^9 atoms/s at $L_{sep} = 42$ mm in Fig 6.16. The ACQAO objective is to use this flux load a second MOT for transfer into a magnetic trap and evaporation toward BEC. The size of this second MOT is estimated from this loading rate as $\sim 9 \times 10^8$ atoms using the MOT data and the scaling law $N \propto \sqrt{R}$ in Chapter 5. This is ~30% of the maximum first trap number, with a reduction of $\sim$ 1000 in background pressure, enabling the basic ACQAO objective 1 in Sec 6.1, that of making a large He* trap capable of condensation.

6.2.4 LVIS and LVIS$^+$ Velocity

The LVIS and LVIS$^+$ final velocities v_f corresponding to the flux data in Fig 6.14 are plotted in Fig 6.17. These features are also qualitatively understood in the same model of a Zeeman accelerator, together with the behaviour of atoms in the trapping field. In general higher velocities occur for increasing scattering rate, and hence larger accelerations, from the forcing MOT beam/push-beam, i.e. toward blue detuning. The slightly higher velocities in the LVIS$^+$ configuration are probably due to higher intensity ($I_{push-beam} \sim 20 I_{MOT}$). Most interestingly both the LVIS and LVIS$^+$ show a uniform range of final velocities for each magnetic field gradient and nearly equal fractional velocity widths dv/v_f.

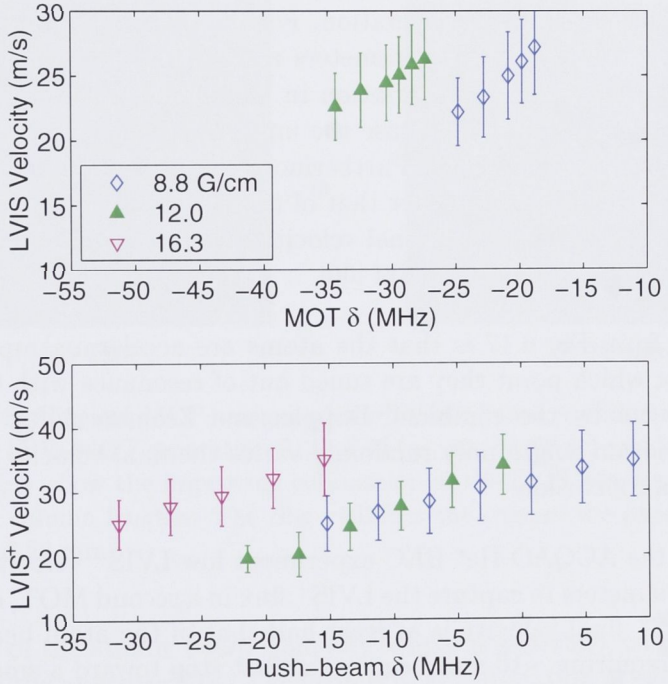

Figure 6.17: Plots of the LVIS velocity (upper) and LVIS$^+$ velocity (lower) corresponding to the flux data in Fig 6.14, showing the variation with MOT beam detuning or push-beam beam detuning respectively at different MOT magnetic field gradients. In both cases the final velocity increases with increasing scattering rate from the forcing beam, while the fractional velocity spread remains nearly uniform as found in Lu *et al.* [36]. The plotted widths are FWHM of the velocity peak.

It has been argued in Sec 6.2.1 that the LVIS/LVIS$^+$ flux is maximised by reducing the atom beam's divergence with the lowest possible initial transverse velocity. In this isotropic MOT this is also the lowest initial longitudinal velocity. Then the uniform final velocity ranges for different $\partial_z \vec{B}$ show that the final velocity of the

atom beam is independent of the initial velocity of atoms entering the extraction column. First the final LVIS velocities in Fig 6.17 vary monotonically with detuning either side the detuning of the peak flux in Fig 6.14, rather than reflecting this minimum in initial longitudinal velocity, as the detuning affects the trapping properties. Second, although the trapping conditions do not change in the LVIS$^+$ configuration within each data set, the final velocity ranges are uniform for different $\partial_z \vec{B}$ despite the significant differences in the those trapping conditions, and hence the initial velocities of atoms entering the extraction column/push-beam.

The fractional velocity spread dv/v_f remains nearly the same, as observed by Lu *et al.* [36]. For the data in Fig 6.17 dv/v_f ~0.25 for the LVIS and ~0.3 for the LVIS$^+$. In Sec 6.2.1 we attributed the velocity width to the same mechanism as Ref [36], namely the distance over which atoms enter the extraction column/push-beam and hence the length of their acceleration. For the LVIS$^+$ the size of the atom cloud remains constant as the MOT parameters remain unchanged. In the LVIS configuration we note the MOT size variation in Chapter 5 was $\sim$ 10% at these gradients and detunings. Then in each case the uniform initial spatial width leads to a uniform fractional velocity width. Furthermore the maximum acceleration of rubidium (1.13×10^5 m/s^2) is one quarter that of the He* atom [72]. Therefore the fractional FWHM dv/v_f of the longitudinal velocity distributions is expected to be broader than the ~0.2 found for Rb in Ref [36].

Overall the picture from Fig 6.17 is that the atoms are accelerated up to a final velocity ~30 m/s, at which point they are tuned out of resonance with the forcing MOT beam/push-beam by the combined Doppler and Zeeman shifts. Moreover increasing the collimation length only randomly varies the final velocity within 20-30%, reinforcing this conclusion.

For the purposes of the ACQAO He* BEC experiment low LVIS$^+$ velocities require smaller laser beam diameters to capture the LVIS$^+$ flux in a second MOT, objective 2 in Sec 6.1. The LVIS$^+$ final velocity is at least half that of the atom beam exiting the Zeeman slower, requiring ~10 mm beams, the first step toward a small capture volume.

6.2.5 LVIS and LVIS$^+$ Divergence

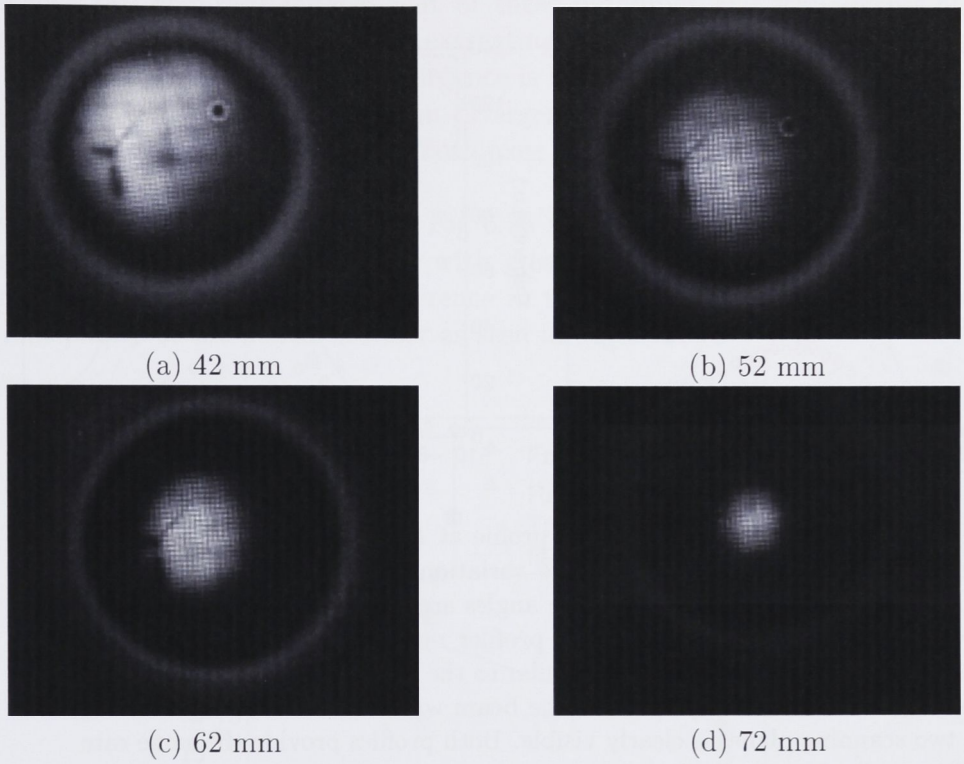

(a) 42 mm (b) 52 mm

(c) 62 mm (d) 72 mm

Figure 6.18: Typical MCP images of the LVIS$^+$ beam are illustrated with increasing LVIS-MOT separation L_{sep} of 42 (a), 52 (b), 62 (c) and 72 mm (d). These clearly show the improving collimation of the LVIS beam with longer extraction column lengths. The ring visible is the edge of the phosphor at a diameter of 22 mm.

The divergence of the atomic beam from any source is generally set by the collimating geometry of the aperture [70]. The geometrical collimation of extraction column can be at best the LVIS aperture diameter (1.5 mm) over the LVIS aperture - MOT centre separation ($L_{sep} \geq 42$ mm), or ≤ 30 mrad. The images of the LVIS$^+$ beam in Fig 6.18 clearly show the changing collimation of the atom beam, in this case with collimation length. The hollow centre of the atom beam image in Fig 6.4 is not visible in the LVIS$^+$ beam images in Fig 6.18. However this mechanism heating the atom beam may still have an effect on the beam's divergence.

Figure 6.19 plots the two orthogonal 1D beam profiles, measured with the helical beam profiler in Fig 6.9, at $L_{sep} = 52$ mm collimation length. The rotating beam profiler measures the flux across each axis in two different planes perpendicular to the beam axis, separated by the profiler diameter, as discussed in Sec 6.1.4. The expansion of the beam width in the distance between the two scanning planes is clearly visible.

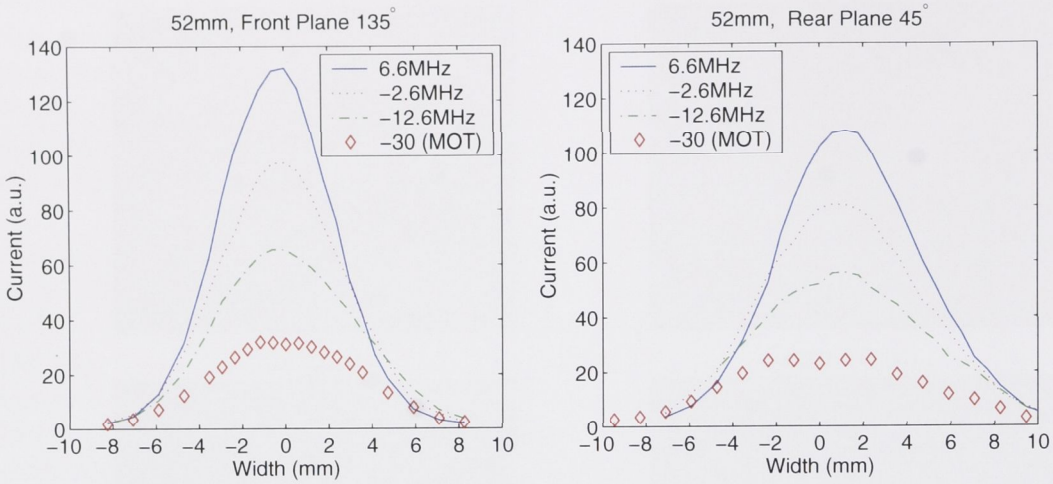

Figure 6.19: The LVIS/LVIS$^+$ beam profile at $L_{sep} = 52$ mm, measured by the helical beam profiler, shows little variation with changing detuning of MOT/push-beam. Note that the scan angles are the opposite of those in the view of Fig 6.9. The rotating beam profiler measures the flux across each axis in two different planes perpendicular to the beam axis, separated by the profiler diameter. The expansion of the beam width in the distance between the two scanning planes is clearly visible. Both profiles provide the same rate (~ 24 mrad) of beam divergence.

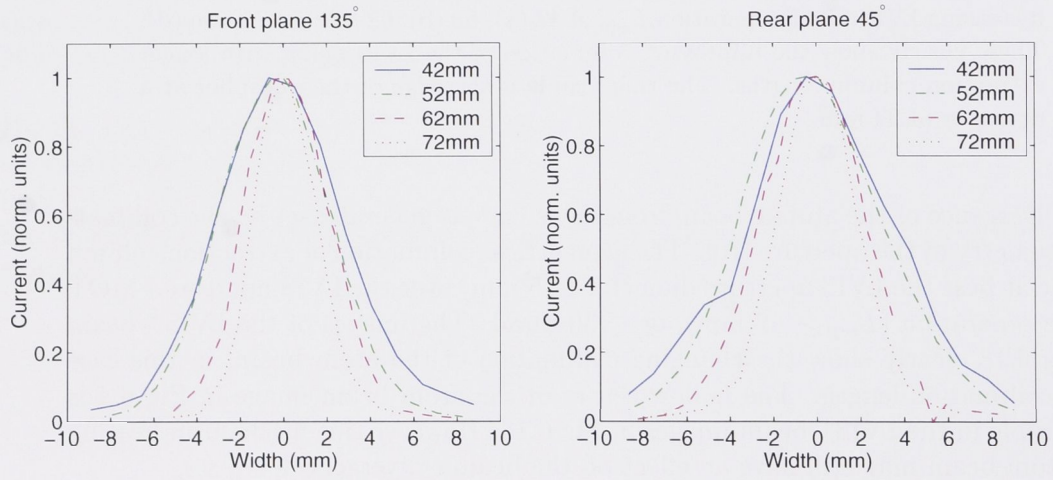

Figure 6.20: The LVIS$^+$ beam profile clearly narrows with increasing collimation length L_{sep} between the MOT centre and the LVIS optic. For comparison of FWHM all plots have been normalized to the peak at 42 mm.

Three different detunings of the LVIS$^+$ push-beam are shown in Fig 6.19 as well as one LVIS profile. The profiles in both the 45° and 135° axes show the same divergence ($\sim$ 24 mrad) independent of these detunings and irrespective of the overall efficiency of the optical force extracting atoms into the atom beam at each detuning. Hence the atom beam divergence is independent from factors other than the geometry. Furthermore the beam divergence in Fig 6.19 is consistent for the experiment's geometry at 52 mm in both axes.

Conversely the helical scan plots in Fig 6.20 very clearly demonstrate decreasing divergence of the atom beam profile with greater collimation. Once again on the beam axis there is a significant difference in the widths measured in the forward and rear planes of the helical scanner as seen in Fig 6.19.

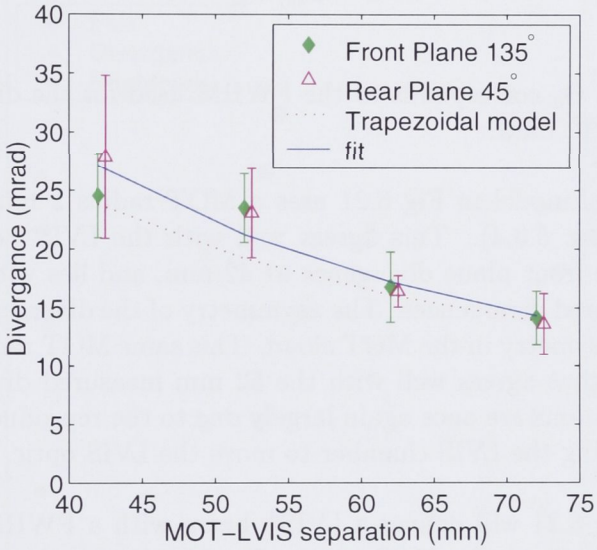

Figure 6.21: Divergence Summary: the data measured by the wire scanner in the forward (□, offset for clarity) and rear (△) planes of the helix correspond with each other and with the mechanical collimation of the MOT beam by the LVIS optic. The data fits well to a $1/L_{cd}$ function (solid line) as well as the prediction of the Ramsey's trapezoidal method based on the LVIS/LVIS$^+$ geometry [70].

The beam profiles in Fig 6.20 can be fitted with a Gaussian profile to provide a FWHM width $w_i = 2r_i$ in each axis. The width of the collimator (the LVIS aperture) is $w_c = 2r_c = 1.5$ mm. Then the divergence is $\Theta = \Delta r_i / L_{cd}$, where L_{cd} is the collimator-detector length (see Fig 6.3), and $\Delta r_i = r_i - r_c$. These divergences plotted in Figure 6.21 demonstrate the decrease in divergence with increasing collimation length, with equal divergences from both axes, even within the error overlap of the closest separation. The solid line in Fig 6.21 is a $1/L_{cd}$ fit to the average divergences, which also agrees well with the data.

In addition an estimate of the geometric collimation is plotted, calculated by the trapezoidal method of Ramsey [70]. In this method the two widths of the source and collimator, $w_s = 2r_s$ and w_c, and the lengths between the source, collimator and detector planes ($L_{sc} = L_{sep}$, L_{sd}, and L_{cd} in Fig 6.3) are employed in the calculation of the umbra ($2p$) and penumbra ($2d$) widths of the beam profile at the detector plane:

$$\Theta_p = \frac{p - r_c}{L_{cd}}, \qquad p = \frac{1}{2}|d_c + a(d_s - d_c)|, \tag{6.1}$$

$$\Theta_d = \frac{d - r_c}{L_{cd}}, \qquad d = \frac{1}{2}(d_c + a(d_s + d_c)) \tag{6.2}$$

$$a = L_{sd}/L_{sc} - 1. \tag{6.3}$$

The average of Θ_p and Θ_d corresponds to the FWHM used for the divergence calculations from the LVIS$^+$ data.

The plotted trapezoidal model in Fig 6.21 uses a MOT radius 2 mm for the size of the source r_s (see Sec 5.3.4). This agrees well with the LVIS$^+$ divergence at 62 and 72 mm and the front plane divergence at 42 mm, and lies within the error bars of the other measured divergences. The asymmetry of the divergence at 42 mm corresponds to a 20% asymetry in the MOT cloud. This same MOT radius (2.4 mm) provides a divergence that agrees well with the 52 mm measured divergences. In general, then, the variations are once again largely due to the reproducibility of the experiment when opening the LVIS chamber to move the LVIS optic.

The divergences in Fig 6.21 will deliver a LVIS$^+$ beam with a FWHM $\leq$ 1 cm to a trapping region 20 cm from the LVIS optic. Combined with the short capture distances resulting from the low LVIS$^+$ velocity in Sec 6.2.4 the LVIS$^+$ flux may be trapped in a second MOT in a volume $\sim$ 1 cm^3. This satisfies the final ACQAO objective 3 for close spacing of the magnetic field coils for a tight magnetic trap to confine and condense He* BEC.

6.3 Comparisons

6.3.1 Collimation Length for the ACQAO Project

A significant consideration in the ACQAO He* BEC experiment is the collimation length to be chosen for using the LVIS/LVIS$^+$ to load a second MOT. The LVIS optic is mounted *in vacuo* and hence cannot be adjusted. The three key properties of the LVIS/LVIS$^+$ beam for the ACQAO objectives in Sec 6.1 are the flux, divergence and velocity. Together flux and divergence provide the beam brightness (Sec 2.2.2). The results the He* LVIS$^+$ flux, divergence and brightness are summarized in Figure 6.22.

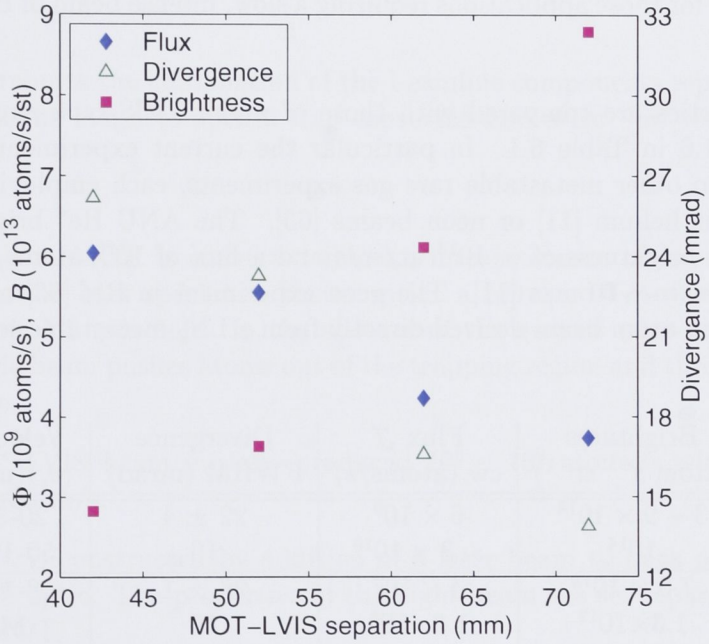

Figure 6.22: Summary of the fundamental properties of the LVIS$^+$ beam, flux (◇), divergence (△) and the brightness (□) derived from these two measurements. The increasing brightness indicates that atoms are still being collimated and recycled into the trap [36].

As observed above in Sections 6.2.5 and 6.2.3, the divergence and flux decrease with the collimation length L_{sep} as the inverse and inverse square respectively. Hence the brightness should be constant for different collimation lengths. Therefore the increasing LVIS$^+$ brightness indicates that atoms are being captured into the trap and recycled [36].

In Sec 6.2.4 we observed that the velocity does not significantly vary for changes in the collimation length. Hence increasing the collimation length decreases the

flux and divergence with no advantage in LVIS$^+$ velocity. The conclusion for the ACQAO project is that the LVIS optic should be installed at the shortest practical collimation length, since the increase in divergence that leads to possible losses from a 1 cm^3 trapping volume will be outweighed by the increase in flux into that volume.

6.3.2 A slow, intense beam of atoms

The brightness of the LVIS$^+$ beam ($\sim 6 \times 10^{13}$ atoms/sr/s) is nearly equivalent of that of the LHe cooled hollow cathode source, 10^{14} atoms/sr/s. However the beam velocity is vastly reduced from 600-700 m/s to $\sim$ 30 m/s. Hence the LVIS$^+$ is eminently suitable for those applications requiring a slow, intense beam of He* atoms (Sec 6.1).

The LVIS$^+$ properties are compared with those of major LVIS-type experiments discussed in Sec 1.6 in Table 6.1. In particular the current experiment may be compared with two other metastable rare gas experiments, each employing a 2D-MOT lens to focus helium [11] or neon beams [63]. The ANU He* bright beam machine reaches a brightness of $\sim 10^{14}$ at/sr/s and a flux of 10^{10} atoms/s slowed from a LN_2 sources to $\sim$70 m/s [11]. The neon experiment in Ref [63] achieves a similar brightness in atom beam derived directly from a LN_2 metastable source and Zeeman slower.

		Brightness (atom s^{-1} sr^{-1})	Flux $\mathcal{J}$ cw (atoms/s)	Divergence FWHM (mrad)	Velocity $\langle v_s \rangle$(m/s)
P	He*	$3 - 9 \times 10^{13}$	6×10^9	22 ± 4	20-35
M	He*	10^{14}	$\sim 3 \times 10^{10}$	10	50-100
A	Cs	7.5×10^{12}	4×10^9	26 ± 1	8-12
B	Rb	1.3×10^{12}	1.3×10^8	10	14
C	Rb	5.0×10^{12}	5.00×10^9	5-36	14
D	Cs	8.5×10^{11}	1.1×10^9	40	8-12
E	Cs	7.5×10^{12}	4.00×10^9	25-27	8-12
F	Cs	1.2×10^{13}	2.20×10^9	11-16	7-16
G	Rb	7.5×10^{13}	6.0×10^{10}	32	50
H	K	-	1.0×10^{11}	-	33
I	Ne*	1.5×10^{14}	6×10^8	-	26

Table 6.1: Summary of Atomic-Beam Performance in the Present Work, and Comparison with Reported Values from Selected Slow ($\langle v_s \rangle < 30$ m/s) Atomic-Beam Sources: A - Arlt *et al.* [56], B - Wohlleben *et al.* [62], C - Lu *et al.* [36], D - Dieckmann *et al.* [45], E - Camposeo *et al.* [58], F - Kohel *et al.* [59], G - Schoser *et al.* [47], H - Catani *et al.* [51], I - Engels *et al.* [63], P - Present experiment and M - ANU bright beam line [11]

Table 6.1 also contains the comparative data, where available, of the LVIS-type experiments discussed in Section 1.6.1 conducted with alkali metals rubidium and cesium. In brightness and flux the He^* LVIS is equal or better of these slow atomic beams. When it comes to velocity the helium experiment yields a higher value. As noted several times previously, He^* atoms have no dark state and are always coupled to the MOT beam/push-beam, and are accelerated continuously. This makes a slow He^* beam difficult to realise. As well helium is the lightest of all these elements (neon is seven times more massive than helium), and this high velocity hides a lower momentum.

6.4 Conclusion

This chapter reports the culmination of the beamline components reported in prior chapters, with the magneto-optical trap converted into a He^* low velocity, intense source (LVIS).

- The 3-beam MOT is converted into an intense source of low velocity with the insertion of a special in vacuo optic: a mirrored 1/4-waveplate with a concentric 1.5 mm hole. In the absence of the on-axis retro-reflected beam, the single beam pushes atoms out of the trapping region and through the LVIS aperture.
- The He^* LVIS beam initially produced $10^8 - 10^9$ atoms/s with an average velocity 25 m/s.
- A $LVIS^+$ is constructed by addition of a laser beam to push atoms through the LVIS optic. The properties of this light beam are set separately to those of the MOT.
- The He^* $LVIS^+$ beam achieves a maximum flux of 6.0×10^9 atoms/s in a beam with an average velocity $\sim$30 m/s and $\sim$ 25 mrad divergence.
- The $LVIS^+$ beam brightness $3 - 9 \times 10^{13}$ atoms/sr/s approaches that of the LHe cooled GHC source.
- Thus the $LVIS^+$ satisfies the ACQAO objectives to deliver a high He^* flux to a small (1 cm^3) trapping volume with a background pressure suitable for evaporative cooling and condensation of a He^* BEC.

These performance measures equal or improve upon the reported performance other high intensity, low velocity atom beams.

CHAPTER 7

Conclusions

This thesis has described a compact MOT loading He* beamline and He* LVIS. In this instance these comprise four steps in the path toward He* BEC for the Australian Research Council Centre of Excellence for Quantum-Atom Optics He* BEC group at the Australian National University:

1. a He* source
2. slowing and guiding the He* beam
3. trapping a large cloud of atoms in a magneto-optical trap, and
4. extracting atoms into a low velocity, intense, bright beam.

7.1 A liquid He cooled, grounded hollow cathode metastable source

The first component of the compact beamline is a novel design for a metastable gas source, presented in Chapter 3. Making a compact beamline requires the minimum average velocity of the atom beam emerging from the source, related directly to source operating temperature. Typical cryogenic liquid nitrogen (80 K) cooled He* sources have substantially reduced beam velocities from those of room temperature sources, $\sim$1 km/s from $\sim$2 km/s (see Fig 3.16). Further cooling with liquid helium to 4 K offers a potential minimum 300 m/s average velocity in an effusive beam.

These cryogenic sources, such as the He* source of the bright beam machine [93], are based on an original design be Shimizu featuring an electron discharge from a needle cathode in a gas vessel surrounded by cooling liquid to an external anode [105]. An effusive flow of atoms from the source requires lower pressures as well as lower temperatures, making the discharge difficult to sustain with the needle cathode.

In a hollow cathode the plasma is surrounded, reducing the loss of electrons and ions, hence making the plasma easier to sustain. In addition the available emitting surface area is greatly increased, supporting a greater electron current density. This higher current density in turn can sustain relatively higher discharge current, exciting more metastable states, at a lower gas pressure.

This grounded hollow cathode (GHC) source is cooled by a commercial liquid helium cryostat. Cooled with liquid nitrogen or liquid helium the cryostat can be operated at any set point between LHe and room temperatures. Thus the source can be operated at 'ultra-cryogenic' temperatures just in excess of the boiling points of helium (4 K), neon (25 K) and argon (90 K).

Cooled with liquid helium the grounded hollow cathode source produces a He* beam of high flux, high brightness and low velocity.

- The LHe cooled Grounded Hollow Cathode (GHC) source produces high flux beam of He* atoms with 450-700 m/s velocity and a brightness 1.2×10^{14} atoms/sr/s.
- Comparably high flux, low velocity beams of metastable neon and argon can be achieved.

7.2 A compact MOT loading beamline

The high brightness LHe cooled GHC source promised to deliver a high performance magneto-optical trap and LVIS when coupled to a high efficiency, compact beamline, described in Chapter 4. This relatively simple atom optics beamline is based around a highly efficient Zeeman slower designed to match the He* beam properties of the source.

The divergent source beam is first collimated by a simple 2-dimensional optical molasses stage as close as possible to the source. This maximised the capture of He* atoms in a $\sim$ 1 cm beam. A key element of a compact He* beamline design is efficient differential pumping between the source chamber at $\sim 10^{-4}$ torr and the trapping chamber at $\sim 10^{-10}$ torr.

Obstructing the line-of-sight path from the source reduces the ground state atom beam gas load on the trapping chamber. A single beam deflects a flux of $7.5 \times$

10^{10} atoms/s metastable atoms from this path into the entrance of the Zeeman slower. Nearly 100% of the velocity distribution of this beam is below the 700 m/s capture velocity of the Zeeman slower when the source is cooled with LHe, and $\sim$ 75% when cooled with LN_2.

The Zeeman slower has been carefully designed and manufactured to slow $\sim$ 80% of the velocity distribution below this capture velocity to $\sim$ 70 m/s. This complete beamline delivers an (unslowed) 1 cm He* beam with flux $1.5 \pm 0.5 \times 10^{10}$ atoms/s and brightness 6.7×10^{10} atoms/sr/s (Chapter 4).

The MOT chamber is located immediately after the Zeeman slower, with the atom beam entering at 45° between the laser beams in the radial plane of the magnetic field. The trapping region is centred just 165 mm after the slower exit to capture the diverging slowed atoms. The MOT uses large 38 mm optics and close, water-cooled magnetic field coils in a specially constructed chamber to achieve high loading rates, over 10^9 atoms/s with liquid nitrogen and $\sim 4\times$ higher with liquid helium.

The results described in Chapter 5 include large atom clouds ($\sim 10^9$ atoms) achievable over a wide range of detunings, intensities and magnetic field gradients. Significant gains in trapped number are achieved with liquid helium cooling of the source ($\sim 2\times$) and variation of power balancing the laser beams ($2 - 3\ \times$). The ultimate number of $\sim 3 \times 10^9$ atoms was achieved at a detuning $\delta = -30MHz$ and axial gradient $\partial_z \vec{B} = 8.7$ G/cm. Typical variations with these parameters was observed.

At just 1.4 m from source to trap centre the LHe cooled beamline is a compact, efficient, easily operable and reliable source of He* atoms with which to load a magneto-optical trap with large numbers of He* atoms. This provides a sound base for conversion into a high intensity, low velocity atom source.

7.3 He* Low Velocity Intense Source

The compact beamline culminates with the first He* low velocity, intense source (LVIS), presented in Chapter 6. The LVIS is constructed by a small modification of the MOT: removing a small (1 mm diameter) centre of one of the laser beams causes a power imbalance that pushes the atoms out of the trapping region into a beam.

For our three retro-reflected beam MOT a special *in vacuo* optic was made: a mirrored 1/4-waveplate with a concentric 1 mm hole. Initially in normal trap conditions $10^8 - 10^9$ atoms/s were pushed through the LVIS aperture with an average velocity 25 m/s.

A fault of the standard LVIS is the remnant collinear optical power after the LVIS aperture that can further interact with atoms in the beam. The hollow ring images of the LVIS beam (Figure 6.4) indicate this is sufficient to transversely heat these atoms. This was rectified by blocking the centre of this MOT beam and replacing its 'push' function with and additional laser beam - the LVIS$^+$ configuration. Optimising the LVIS$^+$ requires mode matching the loading performance of the MOT and the extraction performance of the push-beam.

The optimum $\partial_z \vec{B} = 12$ G/cm, common to both the LVIS and LVIS$^+$, is associated with lower transverse velocities minimising the divergence of atoms extracted into the LVIS/LVIS$^+$ beam. The flux peaks with detuning, the width corresponding with the power broadened linewidth of the accelerating beam. For the LVIS$^+$ a push-beam detuning ~ -10 MHz produces a maximum flux 6×10^9 atoms/s in a beam with an average velocity $\sim$30 m/s and $\sim$ 25 mrad divergence.

The LVIS optic is mounted *in vacuo* on bars (Fig 6.2) permitting adjustment of the separation L_{sep} from the MOT centre. As expected the flux reduces by $1/L_{sep}^2$ and the divergence by $1/L_{sep}$, producing a LVIS$^+$ beam brightness ranging from 3 to 9×10^{13} atoms/sr/s. This brightness approaches that of the LHe cooled GHC source.

The He* LVIS/LVIS$^+$ is the first reported with a metastable rare gas. These performance measures equal or improve upon the reported performance other high intensity, low velocity atom beams and represent the best result with metastable helium (Table 6.1).

7.4 ACQAO Revisited

This thesis has described the first part of the apparatus of the ACQAO BEC group to achieve a large metastable helium Bose Einstein condensate. The great advantage of neutral metastable states is single-particle detection based on electronic methods. Ultimately these provide a detection range considerably greater than optical detection, over twelve orders of magnitude or more. Forming a condensate in a vacuum chamber containing a micro-channel plate requires a large number of He* atoms for evaporative cooling in an ultra-high vacuum chamber.

Although the compact beamline (Chapter 4) loads a large MOT (Chapter 5) this chamber is not sutiable for condensation. The atoms trapped in this first MOT must be transfered to a second UHV trapping chamber for capture in second MOT before transfer to a magnetic trap for evaporative cooling. This atom beam is required to transfer a high flux at low velocities and low divergence to minimise the trapping volume. The high brightness He* LVIS (Chapter 6) delivers atoms into a

1 cm^3 volume some 20 cm from the LVIS optic. This optimises optical access and magnetic trap strengths for magnetic trapping and cooling.

Immediately after completing the LVIS experiments the apparatus was dismantled and relocated to a new laboratory. The source was reinstalled in a new vacuum chamber with special features including *inter alia*:

1. a specially designed cross-shaped skimmer permitting laser access within millimetres of the source nozzle to collimate the atom beam at the smallest possible beam diameter.

2. a 20 cm long collimation stage with curved wavefronts like the ANU bright beam machine (Sec 2.4) to maximise capture and collimation of atoms in this beam.

The chamber where atoms are optically trapped a second time for transfer to the BEC magnetic trap was installed at the output of the $LVIS^+$ and a He^* condensate was first observed on the 22nd of December 2005. The ACQAO He^* BEC machine now produces condensates with 10^6 atoms. For this the LHE cooled compact beamline and LVIS fulfills its purpose as a reliable and efficient apparatus to load the second MOT/magnetic trap for evaporative cooling toward Bose Einstein condensation.

APPENDIX A

Atomic Beam Units

The terms "atomic beam intensity" and "atomic beam brightness" have been used throughout this thesis in a sense, defined in Sec 2.2.2, that has been conventional in the ANU Atomic Manipulation Laboratories and is commonly found in many of the citations in atom optics, e.g. the seminal LIVS paper [36]. However one examiner noted about the term "brightness":

> Although the term is not uniquely defined in the literature, the choice made here is highly non-standard and hence confusing for the reader.

It is noted that the confusion in light optics caused by the use of "brightness" as a synonym for the photometric term "luminance" as well as for the radiometric term "radiance", which is also refered to as "intensity", led to the recommended discontinuence of the term in a quantitative sense by the US National Telecommunications and Information Adminstration in 1996 [124]. The SI units for photometry and radiometry are given below in Tables A.1 and A.2 respectively.

Perhaps atom optics should follow this practice, but then a consensus would need to be reached by the community of practice. The examiner suggested that the quantity refered to here as brightness was equivalent to "luminous intensity". However this seems unsatisfactory as a relative (to the human eye), not an absolute unit (see Tables below).

Quantity	Symbol	SI unit	Abbr.	Notes
Luminous energy	Q_v	lumen second	$lm \cdot s$	units are sometimes called talbots
Luminous flux	F	lumen ($= cd \cdot sr$)	lm	also called luminous power
Luminous intensity	I_v	candela ($= lm/sr$)	cd	an SI base unit
Luminance	L_v	candela per square metre	cd/m^2	units are sometimes called nits
Illuminance	E_v	lux ($= lm/m^2$)	lx	Used for light incident on a surface
Luminous emittance	M_v	lux ($= lm/m^2$)	lx	Used for light emitted from a surface

Table A.1: SI photometry units for the measurement of light, in terms of its perceived brightness to the human eye.

Quantity	Symbol	SI unit	Abbr.	Notes
Radiant energy	Q	joule	J	energy
Radiant flux	ϕ	watt	W	radiant energy per unit time, also called radiant power
Radiant intensity	I	watt per steradian	Wsr^{-1}	power per unit solid angle
Radiance	L	watt per steradian per square metre	$Wsr^{-1}m^{-2}$	power per unit solid angle per unit projected source area. Sometimes confusingly called "intensity".
Irradiance	E	watt per square metre	Wm^{-2}	power incident on a surface. Sometimes confusingly called "intensity".
Radiant exitance	M	watt per square metre	Wm^{-2}	power emitted from a surface.
Radiosity	J	watt per square metre	Wm^{-2}	emitted plus reflected power leaving a surface

Table A.2: SI radiometry units, the measurement of radiant energy (including light) in terms of absolute power.

APPENDIX B

Pixel Calibration

The camera pixel calibration is obtained from an image of a steel etched ruler at the same object distance as the MOT. A line plot of pixel values, parallel with the edge of the ruler, picking upthe graduated markings, is shown in Fig. B.1.

As a cross-check calibration lines are plotted for both the peak points and the trough points. The linear regression fit of these calibration lines produce a calibration (gradient) of 0.0859 ± 0.0004 mm/pixel and 0.0860 ± 0.0002 mm/pixel respectively for the peaks and troughs.

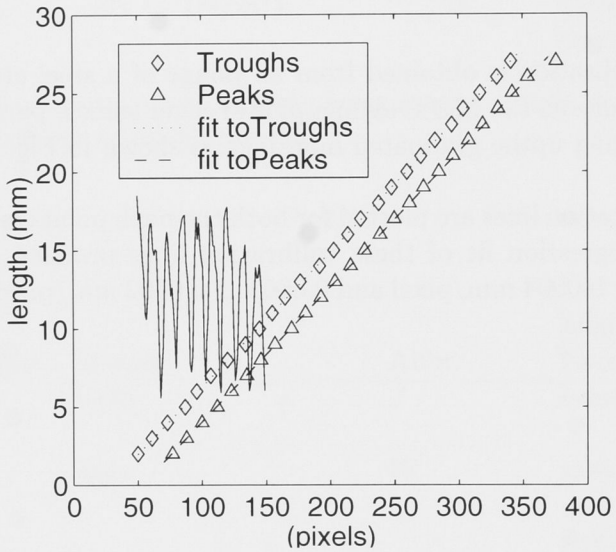

Figure B.1: Pixel calibration: a section of the line plot of pixel values across the ruler is shown, then the plots of peak and trough points, offset for clarity.

APPENDIX C

MOT image size data

PD File	N 10^9	δ MHz	RW mm	CW mm	Image File	Q	σ_x mm	σ_y mm
29Jun17.56.58	1.72	-30	7.19		29Jun17.57.32	med	2.73	3.84
29Jun17.58.19	1.74	-30	7.03	6.90	29Jun17.58.51	med	2.69	3.81
29Jun18.31.39	1.20	-25	4.60	7.40	29Jun18.32.14	med	2.45	3.49
29Jun18.37.42	1.09	-25	5.15	6.40	29Jun18.38.19	med	2.07	3.04
29Jun18.59.49	1.22	-25	6.30	5.90	29Jun19.00.20	med	2.41	3.17
29Jun19.36.12	1.60	-35	7.60	6.70	29Jun19.36.44	low	3.90	2.81
29Jun20.00.22	1.19	-40	8.10	7.10	29Jun20.01.07	low	3.25	5.35
29Jun20.02.24	1.21	-40	7.40	7.90	29Jun20.03.15	low	3.39	5.71
29Jun20.04.53	1.15	-40	8.50	8.30	29Jun20.05.47	low	3.59	6.16
29Jun20.09.36	0.69	-45			29Jun20.11.23	no		
29Jun20.21.43	0.56	-45	10.67					
29Jun20.35.19	0.26	-15	2.68	3.50	29Jun20.36.45	high	1.05	1.41
29Jun20.37.52	0.37	-15	3.10	4.30	29Jun20.38.23	high	1.25	1.72
29Jun20.39.34	0.43	-15			29Jun20.40.04	no		
29Jun20.52.51	0.48	-15	3.20	4.90	29Jun20.53.43	low	1.20	2.10
29Jun21.03.49	0.71	-10	7.80	11.70				
29Jun21.05.16	0.73	-10	7.80	11.50	29Jun21.05.46	low	3.57	3.67
29Jun21.07.44	0.36	-10	10.50		29Jun21.08.19	no		
29Jun21.08.44	0.37	-10	10.60		29Jun21.09.14	no		
29Jun21.11.32	0.29	-10	3.00	3.30	29Jun21.12.03	high	1.20	1.62
29Jun21.14.38	0.52	-10	5.05	5.90	29Jun21.15.09	med	2.13	2.72
29Jun21.24.17	0.50	-10	9.17		29Jun21.25.08	low	4.06	3.14

Table C.1: A sample of MOT data files available for processing. In addition to the abridged automatically logged information on trap number derived from the photodiode (PD) signal, detuning, linear fit FWHMs (RW and CW) and the corresponding image file, associated post-processing data includes image quality 'Q', and the surface fit Gaussian radii σ_x and σ_y.

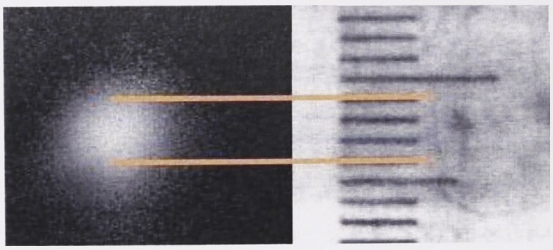

Figure C.1: A (cropped) MOT image alongside a ruler, with a 2σ estimate at 3-4mm.

TOF	(ms)	0.00	0.00	1.00	2.00	3.00
x(surface)	(mm)	0.69	0.70	1.07	1.28	1.45
y(surface)	(mm)	1.15	1.17	1.28	0.90	0.88
x(linear)	(mm)	0.720	0.763	1.102	1.653	2.839
y(linear)	(mm)	0.890		1.144	0.000	
Δ(fit,cal)		1.9%	1.9%	1.9%	8.4%	8.4%
σ_z^2	(mm^2)	0.50	0.54	1.18	2.14	4.59
$\Delta\sigma^2$	(mm^2)	0.05	0.08	0.27	0.94	2.37
σ_ρ^2	(mm^2)	1.04	1.36	1.47	0.20	0.78
$\Delta\sigma^2$	(mm^2)	0.30	0.05	0.40	1.14	0.33
σ_r^2	(mm^2)	0.74	0.77	1.32	0.92	2.97
$\Delta\sigma^2$	(mm^2)	0.39	0.44	0.41	1.58	2.34
σ_a^2	(mm^2)	0.75		1.32	0.92	2.97
$\Delta\sigma^2$	(mm^2)	0.41		0.41	1.58	2.34

Table C.2: MOT image time-of-flight data at detuning -10MHz. Each column contains the results for an individual image. The first five rows provide the four output values of the two fitting routines together with the sum percentage error. The following eight rows provide the derived values and associated errors of *sigma* squared for four averaged combinations: the strong (x or z) axis; the weak (y or ρ) axis; radially 'symmetric' (r); and averaged over all (a) images.

TOF	(ms)	0.00	1.00	2.00	2.00	3.00	3.00
x(surface)	(mm)	1.25	1.36	1.06	1.89		
y(surface)	(mm)	1.37	1.46	1.09			
x(linear)	(mm)	1.271	1.398	1.864	1.890	2.966	3.008
y(linear)	(mm)	1.229	1.356				
Δ(fit,cal)		8.4%	1.9%	8.4%	1.9%	8.4%	8.4%
σ_z^2	(mm^2)	1.59	1.90	2.15	3.57	8.80	9.05
$\Delta\sigma^2$	(mm^2)	0.29	0.41	1.46	0.44	1.78	1.82
σ_ρ^2	(mm^2)	1.69	1.98	1.20			
$\Delta\sigma^2$	(mm^2)	0.43	0.48	0.50			
σ_r^2	(mm^2)	1.64	1.94	1.80	3.57	8.80	9.05
$\Delta\sigma^2$	(mm^2)	0.39	0.45	1.34	0.44	1.78	1.82
σ_a^2	(mm^2)	1.64	1.94	2.44		8.92	
$\Delta\sigma^2$	(mm^2)	0.39	0.45	1.50		1.84	

Table C.3: MOT image time-of-flight data at detuning -15MHz. Each column contains the results for an individual image as described in Table C.2.

TOF	(ms)	0.00	0.00	1.00	2.00	3.00	3.00
x(surface)	(mm)	1.11	1.11	1.76	1.94	1.68	
y(surface)	(mm)	1.03	1.03	1.68	2.01	0.63	
x(linear)	(mm)			1.653	2.034	3.258	3.136
y(linear)	(mm)			1.653			
Δ(fit,cal)		1.9%	1.9%	1.9%	8.4%	8.4%	8.4%
σ_z^2	(mm^2)	1.23	1.24	2.91	3.95	6.10	9.83
$\Delta\sigma^2$	(mm^2)	0.05	0.05	0.27	0.81	2.66	1.71
σ_ρ^2	(mm^2)	1.06	1.05	2.78	4.05	0.40	
$\Delta\sigma^2$	(mm^2)	0.04	0.04	0.19	0.73	0.12	
σ_r^2	(mm^2)	1.15	1.14	2.84	3.98	3.45	9.83
$\Delta\sigma^2$	(mm^2)	0.13	0.13	0.24	0.80	2.79	1.71
σ_a^2	(mm^2)	1.14		2.84	3.98	4.74	
$\Delta\sigma^2$	(mm^2)	0.13		0.24	0.80	3.02	

Table C.4: MOT image time-of-flight data at detuning -20MHz. Each column contains the results for an individual image as described in Table C.2.

TOF	(ms)	0.00	0.00	0.00	0.00	1.00	1.00
x(surface)	(mm)	2.23	2.47	1.83	1.96	1.62	2.00
y(surface)	(mm)	1.91	2.19	1.57	1.66	1.49	1.83
x(linear)	(mm)	2.034		1.695	1.822	1.525	1.864
y(linear)	(mm)	2.034		1.441	1.737	1.441	1.822
Δ(fit,cal)		8.4%	1.9%	1.9%	1.9%	1.9%	1.9%
σ_z^2	(mm^2)	4.53	6.08	3.11	3.57	2.47	3.74
$\Delta\sigma^2$	(mm^2)	0.95	0.23	0.26	0.27	0.21	0.33
σ_ρ^2	(mm^2)	3.88	4.79	2.26	2.89	2.14	3.33
$\Delta\sigma^2$	(mm^2)	0.78	0.18	0.21	0.18	0.15	0.18
σ_r^2	(mm^2)	4.20	5.42	2.67	3.22	2.30	3.53
$\Delta\sigma^2$	(mm^2)	0.93	0.49	0.39	0.34	0.24	0.33
$\Delta\sigma^2$	(mm^2)	3.60				2.89	
$\Delta\sigma^2$	(mm^2)	1.14				0.52	

TOF	(ms)	2.00	3.00	3.00	3.00	4.00	4.00
x(surface)	(mm)	2.19	1.20				
y(surface)	(mm)	2.06	0.87	5.97			
x(linear)	(mm)	2.203	2.627	2.924	5.000	4.831	6.314
y(linear)	(mm)				6.144		
Δ(fit,cal)		8.4%	8.4%	8.4%	8.4%	8.4%	8.4%
σ_z^2	(mm^2)	4.82	3.67	8.55	5.00	23.33	39.86
$\Delta\sigma^2$	(mm^2)	0.88	2.09	1.49	4.71	4.43	6.76
σ_ρ^2	(mm^2)	4.26	0.75	35.59	37.75		
$\Delta\sigma^2$	(mm^2)	0.77	0.18	6.04	6.86		
σ_r^2	(mm^2)	4.63	2.45	19.76	31.05	23.33	39.86
$\Delta\sigma^2$	(mm^2)	0.95	1.99	6.42	6.87	4.43	6.76
σ_a^2	(mm^2)	4.63	12.48			31.05	
$\Delta\sigma^2$	(mm^2)	0.95	6.20			7.21	

Table C.5: MOT image time-of-flight data at detuning -25MHz. Each column contains the results for an individual image as described in Table C.2.

TOF	(ms)	0.00	0.00	1.00	2.00	2.00	2.00	2.00
x(surface)	(mm)	1.85	1.87	2.07	2.32			
y(surface)	(mm)	1.58	1.60	1.89	2.19		1.74	
x(linear)	(mm)	1.737	1.691	1.886	2.297	3.220	3.475	3.602
y(linear)	(mm)	1.737	1.729	1.907		3.729	3.898	4.068
Δ(fit,cal)		0.9%	0.9%	1.9%	8.4%	1.9%	1.9%	1.9%
σ_z^2	(mm^2)	3.22	3.16	3.91	5.32	10.37	12.07	12.97
$\Delta\sigma^2$	(mm^2)	0.18	0.23	0.39	0.97	0.55	0.66	0.75
σ_ρ^2	(mm^2)	2.76	2.77	3.61	4.79	13.90	7.94	16.55
$\Delta\sigma^2$	(mm^2)	0.20	0.18	0.20	0.86	0.68	2.67	0.88
σ_r^2	(mm^2)	2.99	2.96	3.76	5.14	12.07	9.22	14.71
$\Delta\sigma^2$	(mm^2)	0.25	0.25	0.35	1.03	1.12	2.42	1.28
σ_a^2	(mm^2)	2.98		3.76	9.32			
$\Delta\sigma^2$	(mm^2)	0.25		0.35	3.21			

TOF	(ms)	3.00	3.00	4.00	4.00
x(surface)	(mm)		1.92		1.39
y(surface)	(mm)		2.10		0.66
x(linear)	(mm)	2.797	2.542	3.458	
y(linear)	(mm)				
Δ(fit,cal)		8.4%	8.4%	8.4%	8.4%
σ_z^2	(mm^2)	7.82	4.98	11.96	1.94
$\Delta\sigma^2$	(mm^2)	1.57	1.71	2.26	0.58
σ_ρ^2	(mm^2)		4.40		0.43
$\Delta\sigma^2$	(mm^2)		0.99		0.32
σ_r^2	(mm^2)	7.82	4.78	11.96	1.05
$\Delta\sigma^2$	(mm^2)	1.57	1.58	2.26	1.16
σ_a^2	(mm^2)	5.47		3.37	
$\Delta\sigma^2$	(mm^2)	1.87		3.19	

Table C.6: MOT image time-of-flight data at detuning -30MHz. Each column contains the results for an individual image as described in Table C.2.

TOF	(ms)	0.00	1.00	2.00	3.00	4.00	5.00	5.00
x(surface)	(mm)	1.82	2.02	2.24				
y(surface)	(mm)	2.17	2.29	2.51				
x(linear)	(mm)	1.992	2.034	2.373	2.542	3.517	5.805	4.153
y(linear)	(mm)	2.119	2.161	2.500				
Δ(fit,cal)		0.9%	1.9%	1.9%	8.4%	8.4%	8.4%	8.4%
σ_z^2	(mm^2)	3.62	4.10	5.31	6.46	12.37	33.70	17.24
$\Delta\sigma^2$	(mm^2)	0.40	0.29	0.39	1.14	2.13	5.72	3.40
σ_ρ^2	(mm^2)	4.59	4.95	6.28				
$\Delta\sigma^2$	(mm^2)	0.19	0.37	0.30				
σ_r^2	(mm^2)	4.09	4.52	5.78	6.46	12.37	33.70	17.24
$\Delta\sigma^2$	(mm^2)	0.35	0.44	0.49	1.14	2.13	5.72	3.40
σ_a^2	(mm^2)	4.09	4.52	5.78	6.46	12.37	24.79	
$\Delta\sigma^2$	(mm^2)	0.35	0.44	0.49	1.14	2.13	5.88	

Table C.7: MOT image time-of-flight data at detuning -35MHz. Each column contains the results for an individual image as described in Table C.2.

TOF	(ms)	3.00	3.00	4.00	0.00	0.00
x(surface)	(mm)			1.64	1.78	2.06
y(surface)	(mm)		0.53	0.69	1.41	1.80
x(linear)	(mm)	2.500		4.153	1.610	
y(linear)	(mm)				1.483	
Δ(fit,cal)		8.4%	8.4%	8.4%	1.9%	8.4%
σ_z^2	(mm^2)	6.25		8.38	2.87	4.23
$\Delta\sigma^2$	(mm^2)	1.55		4.43	0.28	0.71
σ_ρ^2	(mm^2)		0.28	0.47	2.09	3.25
$\Delta\sigma^2$	(mm^2)		0.55	0.58	0.15	0.55
σ_r^2	(mm^2)	6.25	0.28	4.66	2.46	3.72
$\Delta\sigma^2$	(mm^2)	1.55	0.55	4.21	0.37	0.88
σ_a^2	(mm^2)	2.30		4.66	2.52	
$\Delta\sigma^2$	(mm^2)	2.85		4.21	0.68	

Table C.8: MOT image time-of-flight data at detuning -40MHz. Each column contains the results for an individual image as described in Table C.2.

TOF	(ms)	0.00	0.00	1.00	2.00	3.00	3.00
x(surface)	(mm)	1.95	1.23	2.19	2.18		
y(surface)	(mm)	1.41	0.00	1.75	1.83		
x(linear)	(mm)	1.695	2.076	1.958	2.076	2.445	2.331
y(linear)	(mm)			2.093			
Δ(fit,cal)		1.9%	1.9%	1.9%	1.9%	8.4%	8.4%
σ_z^2	(mm^2)	3.32	2.73	4.31	4.52	5.98	5.43
$\Delta\sigma^2$	(mm^2)	0.38	0.95	0.90	0.77	1.51	1.41
σ_ρ^2	(mm^2)	2.00	0.00	3.68	3.35		
$\Delta\sigma^2$	(mm^2)	0.08	0.00	0.99	0.63		
σ_r^2	(mm^2)	2.84	1.21	3.99	4.11	5.98	5.43
$\Delta\sigma^2$	(mm^2)	0.55	1.75	0.99	0.95	1.51	1.41
σ_a^2	(mm^2)	1.94		3.99	4.11	5.70	
$\Delta\sigma^2$	(mm^2)	1.45		0.99	0.95	1.57	

Table C.9: MOT image time-of-flight data at detuning -45MHz. Each column contains the results for an individual image as described in Table C.2.

APPENDIX D

Regression Analysis

The error in the final value of a compound measurement (such as MOT temperature) can be reduced by the statistical contribution of many individual measurements by regression analysis [97].

Equation (2.39) is linear in $y = \sigma_t^2$ and $x = t^2$ such that we can perform a linear fit to $y = a + bx$. In fact we are intending to minimise the discrepencies between the measured values and the corresponding calculated values: $\Delta y_i = y_i - a - bx$.

For each detuning we have several measurements of y_i for each value of x_i. The total error σ_i of each data point is a combination of fluctuations and instrumental errors which are not equal for every data point, even within the one time set. Therefore each term in the sum of χ^2 is weighted by the deviation at that point before summing. The solutions to the minimisation problem are:

$$a = \frac{1}{\Delta}\left(\sum \frac{x_i^2}{\sigma_i^2} \sum \frac{y_i}{\sigma_i^2} - \sum \frac{x_i}{\sigma_i^2} \sum \frac{x_i y_i}{\sigma_i^2}\right) \tag{D.1}$$

$$b = \frac{1}{\Delta}\left(\sum \frac{1}{\sigma_i^2} \sum \frac{x_i y_i}{\sigma_i^2} - \sum \frac{x_i}{\sigma_i^2} \sum \frac{y_i}{\sigma_i^2}\right) \tag{D.2}$$

$$\Delta = \sum \frac{1}{\sigma_i^2} \sum \frac{x_i^2}{\sigma_i^2} - \left(\sum \frac{x_i}{\sigma_i^2}\right)^2 \tag{D.3}$$

with the error in b calculated as

$$\sigma_b^2 \sim= \frac{1}{\Delta} \sum \frac{1}{\sigma_i^2} \tag{D.4}$$

In this case it is $b \pm \Delta b = b \pm 2/3\sigma_b$ that we are interested in finding.

Bibliography

[1] J.A. Swansson, K.G.H. Baldwin, M.D. Hoogerland, A.G. Truscott, and S.J. Buckman, Appl. Phys. **B 79**, 485, (2004).

[2] J.A. Swansson, R.G. Dall, and A.G. Truscott, Rev. Sci. Inst. **77**, 046103, (2006).

[3] J.A. Swansson, R.G. Dall, and A.G. Truscott, Appl. Phys. B, DOI: 10.1007/s00340-006-2472-y, (2006).

[4] S. Seidelin, O. Sirjean, J. Viana Gomes, D. Boiron, C.I. Westbrook and A. Aspect, J. Opt. B: Quantum Semiclass. Opt. **5**, S112, (2003).

[5] O. Sirjean, S. Seidelin, J. Viana Gomes, D. Boiron, C.I. Westbrook, A. Aspect and G. V. Shlyapnikov, Phys. Rev. Lett. **89**, 2204061, (2002).

[6] F. Pereira Dos Santos, J. Lonard, Junmin Wang, C. J. Barrelet, F. Perales, E. Rasel, C. S. Unnikrishnan, M. Leduc, and C. Cohen-Tannoudji, Phys. Rev. Lett., **86**, 3459, (2001).

[7] A. Robert, O. Sirjean, A. Browaeys, J. Poupard, S. Nowak, D. Boiron, C. I. Westbrook, A. Aspect, Science, **292**, 20, (2001).

[8] R. G. Dall, J. A. Swansson, K. G. H. Baldwin and A. G. Truscott, Project summary for the ACQAO 2005 Annual Report, http://www.acqao.org/research/Towards_BEC_Met_He.pdf, (Accessed 25/12/05.)

[9] T. Wong, M. J. Collet, and D.F. Walls , Phys. Rev. A, **54**, R3718 (1996).

[10] C. J. Dedman, J. Nes, T. M. Hanna, R. G. Dall, K. G. H. Baldwin, and A. G. Truscott, Rev. Sci. Instrum. **75**, 5136 (2004)

[11] K.G.H Baldwin, Contemporary Physics, **46**, 105, (2005).

[12] H. Metcalf, J. Opt. Soc. Am. B, **6**, 2206, (1989).

[13] M. Kumakura and N. Morita, Jpm J. Appl. Phys. **B 31**, L276, (1992).

[14] W. Rooijakkers, W. Hogervorst and W. Vassen, Opt. Comm. **135**, 149 (1997).

[15] Paul J.J. Tol, Norbert Herschbach, Eric A. Hessels, Wim Hogervorst and Wim Vassen, Phys. Rev. A **60**, R761, (1999).

[16] A. Browaeys, J. Poupard, A. Robert, S. Nowak, W. Rooijakkers, E. Arimondo, L. Marcassa, D. Boiron, C.I. Westbrook, and A. Aspect, Eur. Phys. J. D **8**, 199 (2000).

[17] F. Pereira Dos Santos, F. Perales, J. Léonard, A. Sinatra, J. Wang, F.S. Pavone, E. Rasel, C.S. Unnikrishnan, and M. Leduc, Eur. Phys. J. AP **14**, 69 (2001).

[18] A. Browaeys, A. Robert, O. Sirjean, J. Poupard, S. Nowak, D. Boiron, C. I. Westbrook, and A. Aspect, Phys. Rev. A, **64**, 034703, (2001).

[19] S. Nowak, A. Browaeys, J. Poupard, A. Robert, D. Boiron, C. Westbrook, A. Aspect, Appl. Phys. B **70**, 455, (2000).

[20] A. S. Tychkov, T. Jeltes, P. J. J. Tol, N. Herschbach, W. Hogervorst, and W. Vassen, Phys. Rev. A, **73**, 31603 (2006).

[21] N. Herschbach, P. Tol, W. Vassen, W. Hogervorst. G. Woestenenk, J.W. Thomson, P. van der Straten, Phys. Rev. Lett., **84**, 187, (2000).

[22] H. C. Mastwijk, J. W. Thomsen, P. van der Straten, and A. Niehaus, Phys. Rev. Lett., **80**, 5516, (1998).

[23] H.C. Mastwijk, M. van Rijnbach, J.W. Thomsen, P. Van der Straten and A. Niehaus, Eur. Phys. J. D 4, 131 (1998).

[24] G.R. Woestenenk, H.C. Mastwijk, J.W. Thomsen, P. van der Straten, M. Pieksma, M. van Rijnbach, A. Niehaus, Nucl. Inst. Meth. Phys. Res. N, **54**, 194, (1999).

[25] M. Kumakura and N. Morita, Appl. Phys. **B 70**, 555, (2000).

[26] R.J.W Stas, J.M. McNamara, W. Hogerworst and W. Vassen, Phys. Rev. Lett., **91**, 053001, (2004).

[27] L. J. Uhlmann, R. G. Dall, A. G. Truscott, M. D. Hoogerland, K. G. H. Baldwin, and S. J. Buckman, Phys. Rev. Lett., **94**, 173201 (2005).

[28] F. Bardou, O. Emile, J.M. Courty, C.I. Westbrook and A. Aspect, Europhys. Lett, **20** 681, (1992).

[29] N. Herschbach, P. Tol, A. Tychkov, W. Hogervorst and W. Vassen, J. Opt. B: Quantum Semiclass. Opt., **5**, S65, (2003).

[30] A. S. Tychkov, J. C. J. Koelemeij, T. Jeltes, W. Hogervorst, and W. Vassen, Phys. Rev. A, **69**, 055401 (2004).

[31] F. Pereira Dos Santos, F. Perales, J. Léonard, A. Sinatra, Junmin Wang, F. Saverio Pavone, E. Rase, C.S. Unnikrishnan, and M. Leduc, Eur. Phys. J. D **14**, 15 (2001).

[32] F. Pereira Dos Santos, J. Léonard, Junmin Wang, C.J. Barrelet, F. Perales, E. Rasel, C.S. Unnikrishnan, M. Leduc, and C. Cohen-Tannoudji, Eur. Phys. J. D **19**, 103 (2002).

[33] P. A. Molenaar, P. van der Straten, H. G. M. Heideman, H. Metcalf, Phys. Rev. A **55**, 605 (1997).

[34] G. R. Woestenenk, J. W. Thomsen, M. van Rijnbach, P. van der Straten,and A. Niehaus, Rev. Sci. Inst., **72**, 3842, (2001).

[35] R. Jung, S. Gerlach, R. Schumann, G. von Oppen, and U. Eichmann, Eur. Phys. J. D **23**, 415 (2003)

[36] Z.T. Lu, K.L. Corwin, M.J. Renn, M.H. Anderson, E.A. Cornell and C.E.Wieman, Phys. Rev. Lett. **77**, 3331, (1996).

[37] E. Riis, D.S. Weiss, K.A. Moler, and S. Chu, Phys. Rev. Lett., **64**, 1658 (1990)

[38] Chang Yong Park, Chung Mok Lee, Eu Suk Oh, Cho D., J Opt. Soc. Am. B, **16**, 994, (1999).

[39] , Seung Koo Lee, Hyun Sook Lee, Jang Myun Kim, Cho D., J. Phys. B, **38**, 1381, (2005).

[40] E.A. Donley, T.P. Heavner, S.R. Jefferts, IEEE Trans. Inst. Meas., **54**, 1905, (2005).

[41] J.G. Livesey, D.P. Rhodes, D. McGloin, K. Dholakia, J. Mod. Opt., **50**, 1751, (2003).

[42] D. Muller, E.A. Cornell, M. Prevedelli, P.D.D. Schwindt, A. Zozulya, D.Z. Anderson, Opt. Lett., **25**, 1382, (2000).

[43] D.P. Rhodes, G.P.T. Lancaster, J. Livesey, D. McGloin, J. Arlt, K. Dholakia, Opt. Comm., **214**, 247, (2002).

[44] R.S. Conroy, Y. Xiao, M. Vengalattore, W. Rooijakkers, M. Prentiss, Optics Communications **226** 259, (2003).

[45] K. Dieckmann, R. J. C. Spreeuw, M. Weidemuller, and J. T. M. Walraven, Phys. Rev. A **58**, 3891 (1998).

[46] Yuri B. Ovchinnikov, Opt. Comm., **249**, 473, (2005).

[47] J. Schoser, A. Batär, R. Löw, V. Schweikhard, A. Grabowski, Yu. B. Ovchinnikov, and T. Pfau, Phys. Rev. A, **66**, 023410, (2002).

[48] T. B. Swanson, N. J. Silva, S. K. Mayer, J. J. Maki, and D. H. McIntyre, J. Opt. Soc. Am. B, **13**, 1833, (1996).

[49] P. Berthoud, A. Joyet, G. Dudle, N. Sagna and P. Thomann, Europhys. Lett., **41**, 141, (1998).

[50] S. Weyers, E. Aucouturier, C. Valentin, N. Dimarcq, Opt. Comm., **143**, 30, (1997).

[51] J. Catani, P. Maioli, L. De Sarlo, F. Minardi, and M. Inguscio, Phys. Rev. A, **73**, 033415, (2006).

[52] G. Labeyrie, A. Browaeys,W. Rooijakkers, D. Voelkerc, J. Grosperrin, B. Wanner, C.I. Westbrook, and A. Aspect, Eur. Phys. J. D **7**, 341, (1999).

[53] P. Engels, S. Salewski, H. Levsen, K. Sengstock and W. Ertmer, Appl Phys B **69** 407 (1999)

[54] K.I. Lee, J.A. Kim, H.R. Noh, and W. Jhe, Opt. Lett. **21**, 1177, (1996).

[55] J.A. Kim, K.I. Lee, H.R. Noh, and W. Jhe, Opt. Lett. **22**, 117, (1997).

[56] J. J. Arlt, O. Marago, S. Webster, S. Hopkins, and C. J. Foot, Opt. Commun. **157**, 303 (1998).

[57] R. S. Williamson, P. A. Voytas, R. T. Newell, and T. G. Walker, Opt. Express **3**, 111, (1998),

[58] A. Camposeo, A. Piombini, F. Cervelli, F. Tantussi, F. Fuso, and E. Arimondo, Opt. Commun.,**200**, 231 (2001).

[59] J.M. Kohel, J. Ramirez-Serrano, R.J. Thompson, L. Maleki, J.L. Bliss and K.G. Libbrecht, J. Opt. Soc. Am. **B20**, 1161, (2003).

[60] T. B. Swanson, D. Asgeirsson, J. A. Behr, A. Gorelov, and D. Melconian, J. Opt. Soc. Am. B, **15** 2641, (1998).

[61] L. Cacciapuoti, A. Castrillo, M de Angelis and G.M. Tino, Eur. Phys. J. **D 15**, 245, (2001).

[62] W. Wohlleben, F. Chevy, K. Madison, and J. Dalibard, Eur. Phys. J. D **15**, 237, (2001).

[63] P. Engels, W. Ertmer, K. Sengstock, Optics Communications **204**, 185, (2002).

[64] T.J. Gay, "Sources of Metastable Atoms and Molecules"in [67]

[65] W. Lu, K.G.H. Baldwin, M.D. Hoogerland, S.J. Buckman, T.J. Senden, T.E. Sheridan and R.W. Boswell, J. Vac. Sci. Technol. B **16**, 3846 (1998).

[66] W. Lu, PhD thesis, Australian National University (1999).

[67] F. B. Dunning and R. G. Hulet Eds, *Experimental Methods in the Physical Sciences*, **29B**, Academic Press, (1996).

[68] G. Baum, W. Raith, and H. Steidl, Z. Phys. D **10**, 171, (1988).

[69] Chaustowski, R.R., "Atom Lithography using Metastable Gas Species", Honours thesis, The Flinders University of South Australia, 2003; Sih, N., "Atom Lithography", Honours thesis, The Australian National University, 2000.

[70] Norman F. Ramsey, "Thermal Beam Sources" in [67].

[71] M.D. Morse, "Supersonic Beam Sources"in [67]

[72] H.J. Metcalf and P. van der Straten, *Laser Cooling and Trapping*, Springer, New York (1999).

[73] J. C. J. Koelemeij, R. J. W. Stas, W. Hogervorst, and W. Vassen, Phys. Rev. A **67**, 053406 (2003).

[74] C.G. Townsend, N.H. Edwards, C.J. Cooper, K.P. Zetie, C.J. Foot, A.M. Steane, P. Szriftgiser, H. Perrin, and J. Dalibard, Phys. Rev. A **52**, 1423 (1995).

[75] J. Javanainen, J. Opt. Soc. Am., **B10**, 572, (1993).

[76] J. Hoffnagle, Opt.Lett., **13**, 102, (1988).

[77] S. Gozzini, E. Mariotti, C. Gabbanini, A. Lucchesini, C. Marinelli, and L. Moi, Appl. Phys. B **54**, 428, (1992).

[78] M. Zhu, C.W. Oates and J.L. Hall, Phys. Rev. Lett., **67**, 46, (1991).

[79] E. Rasel, F. Pereira Dos Santos, F. Saverio Pavone, F. Perales, C.S. Unnikrishnan and M. Leduc, Eur. Phys. J., **D 7**, 311, (1999).

[80] S. N. Atutov, R. Calabrese, R. Grimm, V. Guidi, I. Lauer, P. Lenisa, V. Luger, E. Mariotti, L. Moi, A. Peters, U. Schramm, and M. Stel, Phys. Rev. Lett., **80**, 2129, (1998).

[81] W. Ketterle, A. Martin, M. A. Joffe and D. E. Pritchard, Phys. Rev. Lett. **69**, 2483 (1992).

[82] H. Batelann, S. Padua, D. H. Yang, C. Xie, R. Gupta and H. Metcalf, Phys. Rev. A **49**, 2780 (1994).

[83] T. G. Aardema, R. M. S. Knops, S. P. L. Nijsten, K. A. H. van Leeuwen, J. P. J. Driessen, and H. C. W. Beijerinck, Phys. Rev. Lett. **76**, 748 (1996).

[84] J. Söding, R. Grimm, Yu. B. Ovchinnikov, Ph. Bouyer, and Ch. Salomon, Phys. Rev. Lett. **78**, 1420 (1997).

[85] M. T. Cashen and H. Metcalf, Phys. Rev. A **63**, 025406 (2001).

[86] M. Partlow, X. Miao, J. Bochmann, M. Cashen, and H. Metcalf, Phys. Rev. Lett. **93**, 213004 (2004).

[87] R. Schumann, C. Schubert, and U. Eichmann R. Jung and G. von Oppen, Phys. Rev. A **59**, 2120 (1999).

[88] M. E. Firmino, C. A. Faria Leite, S. C. Zilio, V. S. Bagnato, Phys. Rev. A **41**, 4070 (1990).

[89] A. Witte, Th. Kisters, F. Riehle, J. Helmcke, J. Opt. Soc. Am. B **9**, 1030 (1992).

[90] S. G. Miranda, S. R. Muniz, G. D. Telles, L. G. Marcassa, K. Helmerson, V. S. Bagnato, Phys. Rev. A **59**, 882 (1999).

[91] M.D. Hoogerland, D. Milic D, W. Lu, H.-A. Bachor, K. G. H. Baldwin and S. J. Buckman, Aust. J. Phys., **49**, 567 (1996).

[92] M. D. Hoogerland, J. P. J. Driessen, E. J. D. Vredenbregt, H. J. L. Megens, M. P. Schuwer, H. C. W. Beijerinck and K. A. H. van Leeuwen, Appl. Phys. B, **62**, 323, (1996).

[93] W. Lu, M.D. Hoogerland, D. Milic K.G.H Baldwin and S.J. Buckman, Rev. Sci. Instrum. **72**, 2558 (2001).

[94] D. Milic, M.D. Hoogerland, K.G.H. Baldwin and S.J. Buckman, Applied Optics **40** (12), 1907 (2001).

[95] R.G. Dall, M.D. Hoogerland, D. Tierney, K.G.H. Baldwin and S.J. Buckman, Applied Physics B **74** (1), 11 - 18 (2002).

[96] Tomasz M Brzozowski, Maria Maczynska, Michal Zawada, Jerzy Zachorowski and Wojciech Gawlik, J. Opt. B: Quantum Semiclass. Opt., **4** 62, (2002).

[97] Philip R. Bevington, "Data reduction and error analysis for the physical sciences", McGraw-Hill, New York, 1969.

[98] Y. Harada, S. Masuda, and H. Ozaki, Chem. Rev., **1997** 1897, (1997)

[99] H. Hotop, "Detection of Metastable Atoms and Molecules"in [67]

[100] P. N. Cooper, *Introduction to nuclear radiation detectors*, Cambridge University Press, 1986.

[101] ETP electron multipliers, *How Electron Multipliers Work*, www.etpsci.com.

[102] M. Zinner, P. Spoden, T. Kraemer, G. Birkl and W. Ertmer, Phys. Rev. A **67**, 010501 (2003).

[103] N. E. Small-Warren and L.-Y. Chow Chiu, Phys. Rev. A, **11**, 1777 (1975).

[104] D.W. Fahey, W.F. Parks and L.D. Schearer, J.Phys. E 13, 381 (1980).

[105] J. Kawanaka, M. Hagiuda, K. Shimizu, F. Shimizu and H. Takuma, Appl. Phys. B **56**, 21 (1993).

[106] K. Ohno, T. Takami, K. Mitsuke and T. Ishida, J.Chem. Phys. 94 (4), 2675 (1991).

[107] J. Thewlis, editor-in-chief, *Encyclopaedic dictionary of physics*, Pergamon Press, Oxford 1961-64.

[108] W. Whaling, W. H. C. Anderson, M. T. Carle, J. W. Brault, H. A. Zarem, J. Res. Natl. Inst. Stand. Technol., **107**, 149 (2002); A. Gottwald, M. Richter and G. Ulm, Rev. Sci. Inst., **76**, 23101 (2005); K.J. Öberg, Eur. Phys. J. D **41**, 25 (2007).

[109] G. Vannaroni, M. Dobrowolny, E. Melchioni, F. De Venuto, and R. Giovi, J. Appl. Phys., **71**, 4709 (1992); A.C. Xenoulis, G. Doukellis, C. Potiriadis, N. Boukos, D.S. Vlachos, NanoStructured Materials, **12**, 311 (1999).

[110] A. Krokhmal, J. Z. Gleizer, Ya. E. Krasik, J. Felsteiner and V. I. Gushenets, J. Appl. Phys, **94**, 55 (2003).

[111] P. van der Straten, private communication with K.G.H. Baldwin (1999).

[112] J. H. Moore, *Building scientific apparatus : a practical guide to design and construction*, Addison-Wesley, London, 1983.

[113] O. Carnal, M. Sigel, T. Sleator, H. Takuma and J. Mlynek, Phys. Rev. Lett. **67**, 3231 (1991).

[114] N. Vansteenkiste, C. Gerz, R. Kaiser, L. Hollberg, C. Salomon and A. Aspect, J. Phys. II France 1, 1407 (1991)

[115] M. Doery, M. Widmer, J. Bellanca, E. Vredenbrecht, T. Bergeman and H. Metcalf, Phys. Rev. Lett. 72 (16), 2546 (1994).

[116] W. Lu, D. Milic, M. D. Hoogerland, M. Jacka, K. G. H. Baldwin, S. J Buckman, Rev. Sci. Inst. 67, 3003 (1996).

[117] T. E. Barrett, S. W. Dapore-Schwartz, M. D. Ray, G. P. Lafyatis, Phys. Rev. Lett. **67**, 3483 (1991).

[118] F.L. Moore, J.C. Robinson, C.F. Bharucha, Bala Sundaram and M.G. Raizen, Phys. Rev. Lett., **75** 4598, (1995).

[119] F. Pereira Dos Santos, F. Perales, J. Leonard, A. Sinatra, Junmin Wang, F. Saverio Pavone, E. Rasel, C.S. Unnikrishnan, and M. Leduc, Eur. Phys. J. D **14**, 15, (2001).

[120] D.J. Wineland, W.M. Itano, J.C. Bergquist, and R.G. Hulet, Phys. Rev. A, **36** 2220, (1987).

[121] Sang Eon Park, Ho Seong Lee, Eun-joo Shin, Taeg Yong Kwon, Sung Hoon Yang, Hyuck Cho, J. Opt. Soc. Am. B, **19**, 2595, (2002).

[122] G.W.F. Drake, Phys. Rev. A, **3**, 908, (1971).

[123] R. G. Herb, U.S. Pat. No. 3,789,298, (1974); M. L. Simpson, U.S. Pat. No. 4,878,014, issued Oct. 31, 1989; National Electrostatics Corporation, "Beam Profile Monitors", Product Bulletin, (1996).

[124] National Telecommunications and Information Adminstration, Federal Standard 1037C, the Federal Glossary of Telecommunication Terms (1996), http://www.its.bldrdoc.gov/fs-1037/dir-005/_0719.htm

semper aliquid novi